Kagome metals

Domenico Di Sante[*]

Department of Physics and Astronomy, University of Bologna, Bologna, Italy

Titus Neupert[†]

Physik-Institut, Universität Zürich, Zürich, Switzerland

Giorgio Sangiovanni[‡] and Ronny Thomale[§]

Institut für Theoretische Physik und Astrophysik and Würzburg-Dresden Cluster of Excellence ct.qmat, Universität Würzburg, Würzburg, Germany

Riccardo Comin[‖] and Joseph G. Checkelsky[¶]

Department of Physics, Massachusetts Institute of Technology, Cambridge, Massachusetts, USA

Ilija Zeljkovic[**]

Department of Physics, Boston College, Chestnut Hill, Massachusetts, USA

Stephen D. Wilson[††]

Materials Department, University of California, Santa Barbara, Santa Barbara, California, USA

(published 12 February 2026)

Three important driving forces for creating qualitatively new phases in quantum materials are the topology of the materials' electronic band structures, frustration in the electrons' motion or magnetic interactions, and strong correlations between their charge, spin, and orbital degrees of freedom. In few material systems do all of these aspects come together to contribute on an equal footing to stabilize new electronic states with unprecedented properties; however, the search for such systems can be guided by models of configurational motifs or key sublattices that can host such physics. One of the most fascinating structural motifs for realizing this rich interplay of frustration, electronic topology, and electron correlation effects is the kagome lattice. This review provides an overview of the theoretical underpinnings driving the physics of kagome lattices and a subsequent discussion on experimental progress in realizing novel states enabled by kagome networks in crystalline materials. Different material classes are discussed, with an emphasis on the phenomenologies of their electronic states and how they map to interactions arising from their kagome lattices.

DOI: 10.1103/1g9n-wm38

CONTENTS

[*]Contact author: domenico.disante@unibo.it
[†]Contact author: titus.neupert@physik.uzh.ch
[‡]Contact author: giorgio.sangiovanni@uni-wuerzburg.de
[§]Contact author: rthomale@physik.uni-wuerzburg.de
[‖]Contact author: rcomin@mit.edu
[¶]Contact author: checkelsky@mit.edu
[**]Contact author: ilija.zeljkovic@bc.edu
[††]Contact author: stephendwilson@ucsb.edu

I. INTRODUCTION

The kagome lattice is recognized as being composed of a corner-sharing network of the iconic elementary motive of frustration, the triangle. This insight was translated into the physics of crystalline materials in two waves: The first focus was on magnetic insulating compounds, such as herbertsmithite, that are derived from strongly correlated oxides and exhibit local magnetic $S = 1/2$ moments of Cu kagome nets (Mendels and Bert, 2010; Norman, 2016). As the Coulomb interactions emanating from the Cu d orbitals are strong, these systems are placed deep in the Mott limit where the kinetic electronic degrees of freedom are frozen out. Herbertsmithite, and polymorphs thereof, thus provided an excellent setting for geometrically frustrated quantum magnetism and topologically ordered spin liquids (Lacroix, Mendels, and Mila, 2011; Iqbal *et al.*, 2013; Bauer *et al.*, 2014; He *et al.*, 2017).

The second focus was on kagome metals. Preceded by binary kagome metals tailored toward supporting Dirac and flat-band electronic states (Ye *et al.*, 2018), the field of many-body electronic order in kagome metals was ignited by the synthesis of layered AV_3Sb_5 ($A = K$, Cs, or Rb) crystals (Ortiz *et al.*, 2019) or the "135" family of kagome compounds. The V^{3+} constituents in this family form a kagome lattice, i.e., a non-Bravais lattice of corner-sharing triangles. Kagome metals, harboring an unprecedentedly rich phenomenology offering itinerant magnetism, charge order, electronic topology, and superconductivity (SC) in a variety of compounds, have initiated a new era of kagome quantum materials (Neupert *et al.*, 2022). Theoretical studies proposed the emergence of $\mathbb{Z}_2$ topological insulators via spin-orbit coupling (SOC) (Guo and Franz, 2009) and quantum anomalous Hall insulators through magnetism and SOC (Xu, Lian, and Zhang, 2015; Guterding, Jeschke, and Valentí, 2016), highlighting the potential for the kagome lattice to host phenomena at the nexus of topology and magnetism. The first experimental confirmation of topological (massive) Dirac fermions in a kagome material was achieved in the ferromagnetic binary kagome compound Fe_3Sn_2 (Ye *et al.*, 2018; Yin *et al.*, 2018), soon followed by the direct observation of the characteristic kagome flat band in the same material (Lin *et al.*, 2018).

Explicitly topological flat bands possessing a $\mathbb{Z}_2$ invariant due to SOC were experimentally verified in the kagome metal CoSn (Kang *et al.*, 2020a). The first explorations of the 135 family of ternary kagome compounds AV_3Sb_5 led to the discovery of a high-temperature charge ordering transition and SC at ambient pressure (Ortiz *et al.*, 2020; H. Chen *et al.*, 2021; Ortiz, Sarte *et al.*, 2021; Kang *et al.*, 2023). The evidence for high-temperature electronic charge order alone, however, which was previously witnessed in other materials such as $NbSe_2$ (Ugeda *et al.*, 2016), would not provide a sufficient basis for the tremendous excitement surrounding kagome metals, and kagome materials in general. Rather, the excitement, as evident from the growing trend of publications and citations in Fig. 1 in the past few years, is fueled by various factors.

To begin, the unconventional nature of charge order with respect to time-reversal symmetry (TRS) breaking or nematicity, as well as the possible appearance of pair density wave (PDW) SC, provides a strong hint that electronic correlations are vital to the formation of quantum many-body phases in kagome metals, which are further enhanced through the presence of Van Hove singularities (VHSs) near the Fermi level (K. Chen *et al.*, 2021; Jiang *et al.*, 2021; Tan *et al.*, 2021; Guo *et al.*, 2022; Mielke *et al.*, 2022; Li *et al.*, 2023b; Guo *et al.*, 2025). The possibility of orbital currents further suggests a largely unexplored facet of correlated electron systems, i.e., a TRS-breaking mechanism descending not from local spins but from orbital moments. Surprisingly, within a relatively short time span, a proliferation of new discoveries and kagome material classes suggests that kagome matter is a

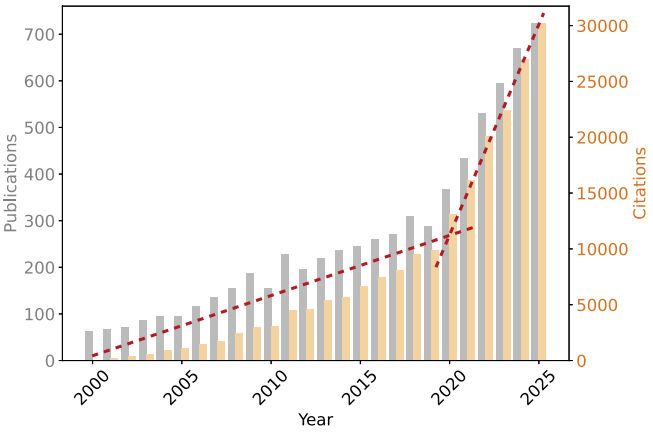

FIG. 1. Number of publications per year, and relative citations, from 2000 to 2025 in which the word *kagome* is mentioned. Data have been retrieved from the Web of Science platform while searching within all fields. The dashed red lines are a guide for the eye to emphasize the surge of interest by the scientific community around 2019, which we ascribe to the experimental discovery of binary and ternary kagome metals. From Ye *et al.*, 2018, and Ortiz *et al.*, 2019.

uniquely diverse host for exotic electronic order. As an added example, FeGe features an itinerant magnetic phase at high temperatures before it develops an onset charge density wave (CDW), as well as the possibility of a spin density wave (SDW), yielding an interesting intertwining of charge and spin fluctuations to be explored further (Teng *et al.*, 2022, 2023; Yin *et al.*, 2022; Lebing Chen *et al.*, 2024; Klemm *et al.*, 2025; Oh *et al.*, 2025).

Parallel to this development on symmetry-broken phases has been the exploration of the prototypical noninteracting kagome band structure features and their fate in real materials. A central line of this research is the flat electronic band, which has been long expected from destructive interference on the hexagonal plaquette of the kagome network (Bergman, Wu, and Balents, 2008). Previously explored in the context of metalizing insulating kagome materials (Mazin *et al.*, 2014; Kelly, Gallagher, and McQueen, 2016), significant progress has been made recently in kagome metals, including spectroscopic identification of these flat bands and observation of interaction effects arising therefrom (Kang *et al.*, 2020a, 2020b; Liu *et al.*, 2020; Gim *et al.*, 2023; Ye *et al.*, 2024; Xie *et al.*, 2025).

At this time, the field keeps expanding into novel kagome material classes with entirely different ordering phenomena such as the 134 family (Eu and Yb) V_3Sb_4 (Ortiz *et al.*, 2023b); the 166 family, like ScV_6Sn_6 (Pokharel *et al.*, 2021; Hu, Wu *et al.*, 2022); and new material classes with varied kagome-site character such as Ti-based and Cr-based kagome metals (B. Liu *et al.*, 2023; Y. Liu *et al.*, 2024). In addition, with the advent of twisted hexagonal moiré systems (Cao *et al.*, 2018; Andrei and MacDonald, 2020; Andrei *et al.*, 2021; Devakul *et al.*, 2021; Kennes *et al.*, 2021; Bernevig and Efetov, 2024) and advances in quantum material heterostructure modeling by design, the possibility of emergent kagome lattices is arising (Claassen *et al.*, 2022). While this branch of kagome matter is still in its early stages, the prospects of such pursuits are promising for reaching the strong-coupling regime of kagome electron systems where topological order and itinerant quasiparticle excitations face off. This would allow access to uncharted territory of strongly correlated electron systems.

A key motivation behind the recent surge of interest in twisted hexagonal moiré systems and heterostructure modeling is the pursuit of truly two-dimensional kagome lattices. Within many bulk kagome materials realized to date, out-of-plane electron hopping can disrupt the flat bands and electron localization essential for many-body correlated and topological phenomena. To address this challenge, several complementary approaches have been actively explored. First, van der Waals kagome metals provide an opportunity to realize atomically thin layers preserving the intrinsic kagome geometry (Park *et al.*, 2020; Yan *et al.*, 2022; Y. Fang *et al.*, 2023; Regmi *et al.*, 2023; Mantravadi *et al.*, 2024; Yun *et al.*, 2025). Second, thin-film growth and surface-engineering techniques enable the fabrication of ultrathin or artificially constructed kagome lattices, thereby allowing precise control over dimensionality and electronic structure (Cheng *et al.*, 2022, 2023; Mihalyuk *et al.*, 2022; Kim and Liu, 2023; J. H. Lee *et al.*, 2024; Ren *et al.*, 2024; Vekovshinin *et al.*, 2024). Together, these strategies aim to create kagome systems where low dimensionality enhances electron correlation effects and topological features, providing a promising avenue for future research in the field.

As much as the experimental side of the field has flourished with new discoveries, kagome metals have also pushed the frontiers of theoretical understanding. In particular, the microscopic description and conceptualization of kagome metals has posed a new level of intricacy in correlated electron systems for three main reasons.

(1) The kagome lattice exhibits three sublattices and, combined with the relevance of multiple orbitals in all kagome metals known to date, enforces a complicated kinetic electronic model even in its most reduced effective form (Kiesel and Thomale, 2012). This presents a fundamental challenge to a large fraction of contemporary many-body methods beyond mean field that are typically constrained to simpler kinetic models.

(2) Coulomb interactions have likewise already been unveiled as a necessary ingredient in V-based kagome metals dominated by vanadium d orbitals (Di Sante, Kim *et al.*, 2023), an ingredient that is likely to be strengthened in future Cr-based (Sangiovanni, 2024) or even Cu-based (Wenger *et al.*, 2024) kagome metals with an increasingly filled d-shell valence. This implies that a many-body electronic ansatz for kagome metals will be largely indispensable.

(3) Phonons have also been shown to be a necessary component of any microscopic kagome modeling, as suggested by large electron-phonon coupling and charge orderings commensurate with dominant phonon modes (T. Hu *et al.*, 2023; Tuniz *et al.*, 2023, 2025). This suggests that any all-electronic modeling of kagome matter will miss out on essential aspects and that phonons have to be considered at all levels of effective kagome metal modeling.

As a consequence, the actual theoretical perspective on kagome metals turned out to be highly fragmented, as most approaches cannot treat the impact of all relevant degrees of freedom on equal footing. As experimental evidence suggests, however, this is needed to account for the astounding richness of electronic orders in kagome matter. The same holds for the typical experimental observables provided by bulk measurements, surface probes, transport signatures, and spectroscopic evidence, where a quantitative correspondence is enabled only by starting with a complex material modeling.

This has put kagome metals at a new level of complexity compared to previous paradigms of correlated electron systems such as high-temperature cuprates. There, as intricate as the nature of the cuprate phase diagram may be and as many questions as it may currently pose, the single band Hubbard model provides an extremely powerful effective description. Such a simple yet universal effective model does not exist for kagome materials. Instead, understanding kagome matter at a deeper level has necessitated methods and models with a more inclusive ansatz with respect to different low-energy degrees of freedom.

Within such a diversified and complex landscape of theoretical and experimental efforts, the goal of this review is to provide a comprehensive overview of kagome metals,

beginning with an analysis of their single-particle electronic and phonon properties in Sec. II, including the electronic structure of spinless electron models in Sec. II.A, spin-orbit interactions in Sec. II.B, and lattice vibrations in Sec. II.C. We then explore in Sec. III many-body phenomena such as CDWs in Sec. III.A, SC in Sec. III.B, PDWs in Sec. III.C, electron-phonon interactions in Sec. III.D, and the role of correlations and fluctuating local moments in Sec. III.E. A detailed discussion on the various materials classes follows in Sec. IV, encompassing binary and ternary kagome compounds in Secs. IV.A and IV.B, respectively, with representative examples across different elemental compositions. Finally, in Sec. V we summarize key insights and outline future research directions in the study of kagome metals.

II. SINGLE-PARTICLE ELECTRONIC AND PHONON PROPERTIES

The kagome lattice geometrically consists of a two-dimensional network of corner-sharing triangles, as shown in Fig. 2(a). The unit cell includes three sublattice sites, conventionally called the A, B, and C sites. These sites result in a high degree of geometrical frustration for the hopping of electrons between the different atoms. In the following, in Secs. II.A and II.B, we discuss the properties of several single-particle models on the kagome lattice without accounting for any many-body contribution that could potentially arise from electron-electron and electron-phonon interactions. These properties are reviewed in Sec. III.

A. Electronic structure of spinless electrons

At the single-particle level, the first important differentiation is the number of orbital degrees of freedom per site. This influences the size of the associated Hilbert space and the number of electronic states. We start in Sec. II.A.1 by revising the well-known and widely used model of a single orbital per site and, more specifically, simple isotropic s-orbital-like electrons, and in Secs. II.A.2 and II.A.3, we extend it by the inclusion of two or more orbitals. This extension and increase in the complexity of the model turns out to be crucial for its expressivity in relation to real-world kagome materials.

1. One orbital per site

The simplest kagome lattice model is constructed by assuming a single orbital per lattice site, most commonly of s-like character (such as s, p_z, or d_{z^2}) because of their trivial transformation under the action of point group symmetry operations. This simplification, long adopted in theoretical studies, captures the essential lattice connectivity responsible for the characteristic kagome band structure. In real materials, however, the spatial orientation and nature of the relevant orbitals with respect to the underlying lattice play a crucial role in realizing the kagome electronic bands; we return to this point in later sections.

The starting point is then the tight-binding (TB) model of spinless s-orbital electrons hopping on the lattice given by the single-particle Hamiltonian

$$H_0 = -t \sum_{\langle (i,s)(j,l) \rangle} c^\dagger_{i,s} c_{j,l}, \tag{1}$$

where t is the hopping amplitude, $c^\dagger_{i,s}$ ($c_{i,s}$) creates (destroys) an electron in the unit cell i and sublattice site s of the kagome lattice, and $\langle (i,s)(j,l) \rangle$ denotes all pairs of nearest-neighbor sites. Transforming Eq. (1) in momentum space, it becomes $H_0 = \sum_{\mathbf{k}} \Psi^\dagger_{\mathbf{k}} \mathcal{H}^0_{\mathbf{k}} \Psi_{\mathbf{k}}$, with $\Psi^\dagger_{\mathbf{k}} = (c^\dagger_{\mathbf{k},1}, c^\dagger_{\mathbf{k},2}, c^\dagger_{\mathbf{k},3})$ and

$$\mathcal{H}^0_{\mathbf{k}} = \begin{bmatrix} 0 & \cos \mathbf{k}\cdot\mathbf{a}_1 & \cos \mathbf{k}\cdot\mathbf{a}_2 \\ \cos \mathbf{k}\cdot\mathbf{a}_1 & 0 & \cos \mathbf{k}\cdot\mathbf{a}_3 \\ \cos \mathbf{k}\cdot\mathbf{a}_2 & \cos \mathbf{k}\cdot\mathbf{a}_3 & 0 \end{bmatrix}. \tag{2}$$

The index $s = 1$, 2, or 3 in $c^\dagger_{\mathbf{k},s}$ refers to any of the three basis sites A, B, and C in the triangular unit cell, whereas $\mathbf{a}_1 = a\hat{x}$, $\mathbf{a}_2 = a(\hat{x} + \sqrt{3}\hat{y})/2$, and $\mathbf{a}_3 = \mathbf{a}_2 - \mathbf{a}_1$ identify the three nearest-neighbor vectors, with a the lattice parameter.

The eigenvalue spectrum of $\mathcal{H}^0_{\mathbf{k}}$, shown in Fig. 2(b) with the corresponding DOS, consists of two dispersive bands,

$$E^{(1,2)}_{\mathbf{k}} = -t[1 \pm \sqrt{4A_{\mathbf{k}} - 3}], \tag{3}$$

with $A_{\mathbf{k}} = \cos^2 \mathbf{k}\cdot\mathbf{a}_1 + \cos^2 \mathbf{k}\cdot\mathbf{a}_2 + \cos^2 \mathbf{k}\cdot\mathbf{a}_3$, and one flat band at energy $E^{(3)}_{\mathbf{k}} = 2t$. The dispersive bands $E^{(1,2)}$ touch at the corner of the Brillouin zone (BZ) $\mathbf{K} = (2\pi/3a, 0)$ and $\mathbf{K}' = (-2\pi/3a, 0)$, in proximity of which they exhibit a linear energy-momentum dispersion relationship analogous to the case of the honeycomb lattice. In fact, by linearizing $\mathcal{H}^0_{\mathbf{k}}$ near $\mathbf{K}$ and $\mathbf{K}'$ and subsequently projecting onto the subspace spanned by the bands $E^{(1,2)}$, one obtains the Dirac Hamiltonian $h_{\mathbf{k}} = v_F(\tau_3 k_x + \tau_1 k_y)$, where $v_F = \sqrt{3}t$ is the Fermi velocity and τ_i are Pauli matrices (Guo and Franz, 2009).

In addition to the dispersive bands, a flat band $E^{(3)}$ independent of the electron wave vector $\mathbf{k}$ exists. This flat band is degenerate with one of the two dispersive bands at the center of the BZ Γ, where the band touching is quadratic in momentum. The presence of a flat band can be understood from a mechanism relying on the destructive quantum phase interference of fermion hopping paths in certain two-dimensional networks. Besides the kagome lattice, these also include the dice (Sutherland, 1986), Lieb (Lieb, 1989), and decorated square lattices (Tasaki, 1992). With a specific focus on the nearest-neighbor electronic hopping model of Eq. (1), one can in fact build the real-space eigenfunction Ψ with alternating phases at neighboring corners of the hexagon shown in Fig. 2(c). Such an electronic state is geometrically confined within a single hexagon because any hopping to neighboring cells is canceled out by destructive phase interference. This real-space electronic localization translates into flat momentum-space eigenfunctions with no energy dispersion.

We emphasize that this mechanism relies strictly on the nearest-neighbor hopping approximation; further-neighbor terms generally introduce a finite dispersion into the nominally flat band. Moreover, the formation of perfectly flat bands in real kagome materials is nontrivial because the relevant p and d orbitals have distinct symmetry properties compared to

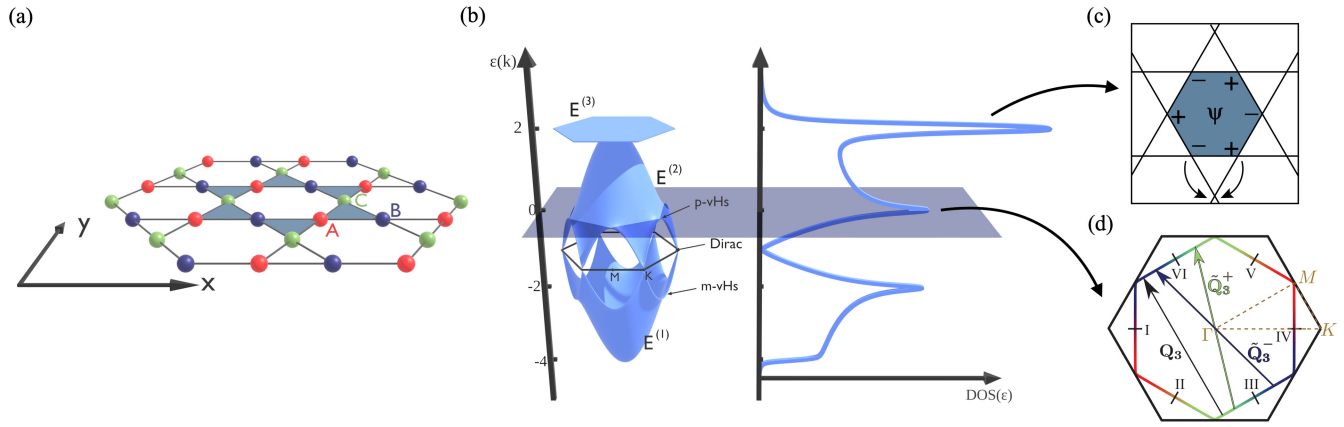

FIG. 2. (a) Structure of the ideal kagome lattice. A, B, and C are the three sites in the unit cell. The blue triangles highlight the corner-sharing configuration. (b) Band structure and corresponding density of states (DOS) in units of the hopping integral t resulting from the three-sublattice structure of the kagome lattice shown in (a). The electron fillings $n = 3/12$ and $n = 5/12$ (horizontal gray plane) are located at VHSs, as visible in the density of state plot from the two divergences symmetric to the location of the Dirac point. (c) Confinement of the electron wave function Ψ. The plus and minus signs indicate the phases of the flat-band eigenstate at neighboring sublattices. Any hoppings outside the hexagon (arrows) are canceled by destructive quantum interference, resulting in the perfect localization of the electron in the blue hexagon. (d) Fermi-surface distribution of the sublattice weight for the pure-type VHSs at filling $n = 5/12$. The Fermi surface touches the M point of the hexagonal BZ where the DOS diverges, as shown in (b). Its topology allows for three nesting vectors connecting parallel opposite sides of the Fermi surface, one of which is $\mathbf{Q}_3 = (-\pi/2, \sqrt{3}\pi/2)$. The colors red, blue, and green label the major sublattice occupation of the Fermi-surface states, in agreement with the sublattice coloring scheme of (a). $\tilde{\mathbf{Q}}_3^{\pm}$ originate from opposite shifts of $\mathbf{Q}_3$ and link states of similar sublattice weights. The labels I–VI are guides for the eye to help reading off the modulation of sublattice occupation weights encoded in $|u_{s,n=2}(\mathbf{k})|^2$ for band $E^{(2)}$ and momenta $\mathbf{k}$ along the Fermi surface. (c) Adapted from Kang *et al.*, 2020a. (d) Adapted from Kiesel and Thomale, 2012.

idealized s-like orbitals. Achieving an ideal kagome band structure thus requires the orbital character to be properly aligned with the lattice geometry, a condition recently clarified by Kim and Liu (2023), who showed that only certain orbital configurations (for example, d_{z^2}) or rotated orbital bases under large crystal-field splitting can host true flat bands.

A second instructive way to understand the appearance of a flat band on the kagome lattice takes root in the theory of graphs (Mielke, 1991a, 1991b; Roychowdhury *et al.*, 2024). This method also explains why the dispersion of bands $E^{(1,2)}$ resembles that of nearest-neighbor hopping models on the honeycomb lattice. If $\mathbf{A}$ is a generic matrix of arbitrary dimensions, then the two matrices $\mathbf{A}\mathbf{A}^\dagger$ and $\mathbf{A}^\dagger\mathbf{A}$ are isospectral, except for zero modes that result from a potential dimension mismatch between the kernel of $\mathbf{A}$ and $\mathbf{A}^\dagger$ if $\mathbf{A}$ is not a square matrix. Identifying $\mathbf{A}\mathbf{A}^\dagger$ as the adjacency matrix of the honeycomb lattice graph, $\mathbf{A}^\dagger\mathbf{A}$ turns out to be the adjacency matrix of its incident or line graph, i.e., the graph originating from the promotion of edges to vertices.

For the honeycomb lattice, the incidence graph is the kagome lattice (Roychowdhury *et al.*, 2024). The adjacency matrix can be thought of as a hopping-1 nearest-neighbor Hamiltonian similar to Eq. (1). The adjacency matrix of a line graph can also be shown to have a zero mode as its lowest eigenvalue (Cvetkovic, Rowlinson, and Simic, 2004; Chiu *et al.*, 2022). The flat band, or zero mode, in the kagome spectrum can then be traced back to the difference in the dimensions of the two graph adjacency matrices, which is simply the difference in the number of sites (three) in the kagome lattice unit cell versus the two sites of the honeycomb lattice unit cell. This analysis explains why, besides the flat band, the two lattices are identical from a spectral point of view, with both featuring Dirac-like linear dispersions at the K and K' valleys and VHSs at the M points.

However, unlike the honeycomb lattice, the lack of particle-hole symmetry in the kagome spectrum emerges prominently when one looks at the redistribution of the real-space A, B, and C sublattice characters in the momentum-dependent wave function. In fact, the transition from real space to momentum space upon Fourier transform reads

$$\begin{aligned} c^\dagger_{i,s} &= \sum_{\mathbf{k}} c^\dagger_{\mathbf{k},s} \exp\left[-i\mathbf{k}(\mathbf{R}_i + \mathbf{r}_s)\right] \\ &= \sum_{\mathbf{k},n} u^*_{s,n}(\mathbf{k}) c^\dagger_{\mathbf{k},n} \exp\left[-i\mathbf{k}(\mathbf{R}_i + \mathbf{r}_s)\right], \end{aligned} \tag{4}$$

where $\mathbf{R}_i$ denotes the unit-cell location and $\mathbf{r}_s$ represents the sublattice location within the unit cell. The core information is encoded in the transformation coefficients $u_{s,n}(\mathbf{k})$, namely, the eigenvectors of $\mathcal{H}^0_{\mathbf{k}}$ in Eq. (2), which are known as sublattice weights (Kiesel and Thomale, 2012). For a given band n that identifies any of the $E^{(1,2,3)}$ and momentum point $\mathbf{k}$ in the BZ, the coefficients obey $\sum_s |u_{s,n}(\mathbf{k})|^2 = 1$.

Noteworthy is the distribution of the sublattice weights at the VHS. At variance with the bipartite honeycomb lattice, the kagome bands host two different types of VHSs that are commonly labeled as sublattice mixed (m type) and sublattice pure (p type), characterized by odd and even parities at the M point, respectively (Kiesel and Thomale, 2012; Kiesel, Platt, and Thomale, 2013; Wang *et al.*, 2013; Kang *et al.*, 2022; Profe *et al.*, 2024). Figure 2(d) shows the evolution of

$|u_{s,n=2}(\mathbf{k})|^2$ on the Fermi surface at the p-type VHS, where the eigenstates near the three M points are localized on mutually different sublattices. By contrast, the lower VHS has mixed sublattice character, with the eigenstates equally distributed over mutually different sets of two sublattices for each M point.

Regardless of the sublattice decoration, the Fermi-surface topologies at both VHSs suggest $\mathbf{Q}_1 = (-\pi/2, -\sqrt{3}\pi/2)$, $\mathbf{Q}_2 = (\pi, 0)$, and $\mathbf{Q}_3 = (-\pi/2, \sqrt{3}\pi/2)$ as nesting vectors. However, for the p-type VHS, the different sublattice character of states at the three distinct M points reduces the effectiveness of the nesting vectors in the particle-hole fluctuation channels compared to a Fermi surface with identical topology and constant orbital makeup. In fact, because of sublattice interference (Kiesel and Thomale, 2012; Kiesel, Platt, and Thomale, 2013), the particle-hole fluctuation channels split into six different nesting vectors that connect Fermi-surface regions of equal sublattice weights. For instance, for the case of $\mathbf{Q}_3$, this amounts to a shift to $\tilde{\mathbf{Q}}_3^{\pm} = \mathbf{Q}_3 \pm (\pi/4, \pi/4\sqrt{3})$, as shown in Fig. 2(d).

The distributions of sublattice characters of VHSs in kagome systems are important for possible Fermi-surface instabilities, which are modulated by the matrix-element effects of the sublattice textures. Indeed, the noninteracting two-particle susceptibility in momentum-frequency space is defined as

$$\chi^0_{s_1 s_2 s_3 s_4}(\mathbf{q},\omega) = -\Omega \int \frac{d\mathbf{k}}{4\pi^2} \times \sum_{n,m} u_{s_4,n}(\mathbf{k}) u^*_{s_2,n}(\mathbf{k}) u_{s_1,m}(\mathbf{k}+\mathbf{q}) u^*_{s_3,m}(\mathbf{k}+\mathbf{q}) \times \frac{n_F[E^{(n)}_{\mathbf{k}}] - n_F[E^{(m)}_{\mathbf{k}+\mathbf{q}}]}{\omega + i\delta + E^{(n)}_{\mathbf{k}} - E^{(m)}_{\mathbf{k}+\mathbf{q}}}, \quad (5)$$

where Ω is the unit-cell volume, n/m are the band indices, $n_F(E)$ is the Fermi-Dirac distribution, δ is an infinitesimally small broadening, and the integral is carried out over the entire BZ.

It is clear how the presence of the weighting coefficients $u_{s,n}(\mathbf{k})$ has a sizable influence on the particle-hole fluctuations. The physical susceptibility is given by the susceptibility matrix elements $\chi^0_{s_1 s_1 s_3 s_3}(\mathbf{q},\omega)$, whereas the Lindhard function neglects the contribution from the coefficients $u_{s,n}$ in Eq. (5). Figure 3(a) displays the sublattice-resolved eigenvalues of the static physical bare susceptibility $\chi^0_{s_1 s_1 s_3 s_3}(\mathbf{q}, \omega = 0)$ (the solid colored points) and the Lindhard function (the dashed gray line) along a high-symmetry path at the p-type VHS. The former does not reveal any peak around the $M = \mathbf{Q}_3$ point, and the eigenvector of the largest eigenvalue is attributed mainly to the B and C sublattices, as the nesting vector $\mathbf{Q}_3$ connects parts of the Fermi surface that are dominated by those sublattices; see Fig. 2(d).

As a result, the susceptibility along the line Γ–M is almost constant because the opposite edges of the hexagonal Fermi surface connected by $\mathbf{Q}_3$ are likewise dominated entirely by the B and C sublattices. However, the Lindhard function that discards the orbital makeup displays a pronounced peak at the

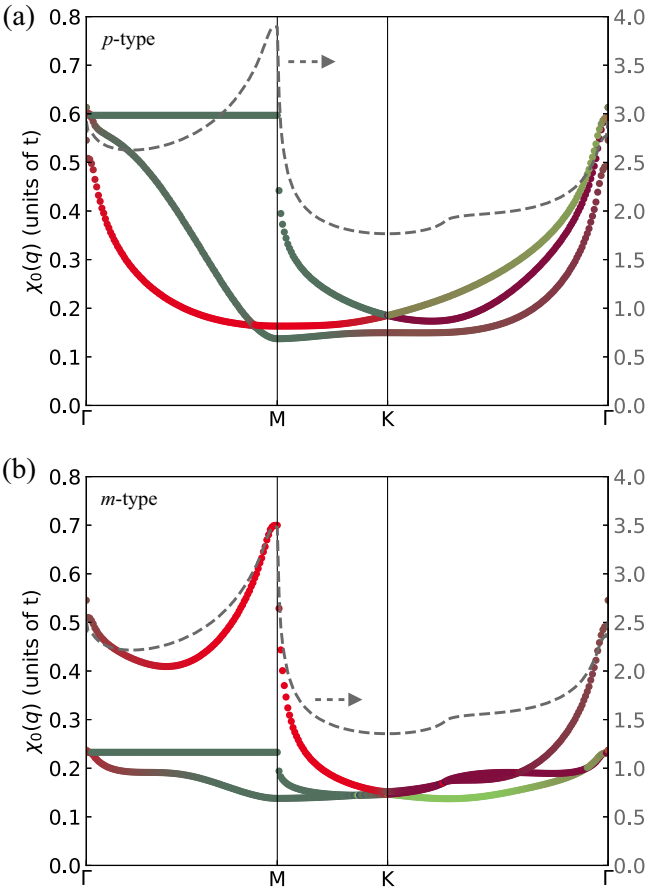

FIG. 3. (a) Eigenvalues of the static noninteracting susceptibility $\chi^0_{s_1 s_1 s_3 s_3}(\mathbf{q}, \omega = 0)$ along a high-symmetry path of the kagome BZ for the chemical potential set at the p-type VHS. The colors refer to the sublattice contributions in the susceptibility eigenvectors and follow the color scheme given in Fig. 2(a) for the A, B, and C sublattices. The dashed gray line, whose y axis is on the right, reports the Lindhard function. (b) Same as (a) but for the chemical potential set at the m-type VHS.

M point as a consequence of the Fermi-surface nesting. Alternatively, at the m-type VHS [Fig. 3(b)], the physical susceptibility shows a noticeable peak at the M point attributed to the A sublattice, which is the common sublattice shared by the Fermi-surface segments connected by the $\mathbf{Q}_3$ nesting vector. The Lindhard function exhibits a similarly pronounced feature. A comparison of Figs. 3(a) and 3(b) demonstrates the clear effect of the sublattice interference that originates from the modulation of sublattice weights on the Fermi surfaces at the VHS (Kiesel and Thomale, 2012; Kiesel, Platt, and Thomale, 2013).

2. Two and three orbitals per site

The description in terms of itinerant electrons as given by the one s-like orbital per site model can be adopted as a basis to study the phenomenology of some realistic kagome systems that are located at intermediate coupling and not in the Mott-type local spin regime. Herbertsmithites (Norman, 2016) like $ZnCu_3(OH)_6Cl_2$ are notable candidates in the latter regime (Mazin *et al.*, 2014; Di Sante *et al.*, 2020). Promising

alternative platforms have also been proposed, such as optical kagome lattices of ultracold fermionic atomic gases, including isotopes like ^{6}Li and ^{40}K (Jo *et al.*, 2012).

In the weaker coupling, itinerant regime, the discovery of AV_3Sb_5 kagome metal compounds (Ortiz *et al.*, 2019) with their large number of contributing orbitals from both V and Sb near the Fermi level, have required the development of more sophisticated multiorbital effective models as a prerequisite to any analysis of many-body instabilities. We use this material as one concrete example to illustrate the complexity that arises in this regime. In this context X. Wu *et al.* (2021) started with the assumption that the *ab initio* band structure of AV_3Sb_5 closely matches angle-resolved photoemission spectroscopy (ARPES) measurements taken below the CDW transition temperature, despite the density functional theory (DFT) calculations being done without considering the Star-of-David-type structural distortion (Ortiz *et al.*, 2020; Tan *et al.*, 2021).

The layered structure of AV_3Sb_5, combined with the large anisotropy in the resistivity ρ_c/ρ_{ab} [≈600 for CsV_3Sb_5 (Ortiz *et al.*, 2020)] motivated X. Wu *et al.* (2021) to constrain themselves to the two-dimensional V-Sb kagome plane. When one sets $k_z = 0$, DFT predicts three distinct Fermi surfaces in AV_3Sb_5: (i) a pocket formed by vanadium d_{xy}, $d_{x^2-y^2}$, and d_{z^2} orbitals near a p-type VHSs, (ii) two additional pockets created by vanadium d_{xz} and d_{yz} orbitals close to another p-type VHSs below the Fermi level and an m-type VHS above it, and (iii) a circular pocket around Γ comprising antimony p_z orbitals. Owing to opposite mirror M_z eigenvalues, electronic states in pockets (i) and (ii) do not hybridize, while the allowed hybridization terms between pockets (ii) and (iii) are small.

For their two orbitals per site effective model, X. Wu *et al.* (2021) considered only the Fermi pockets (ii) because they carry the dominant DOS at the Fermi levels and preserve the complexity of multiple VHSs of both p-type and m-type character. More importantly, the effective model captures all irreducible band representations at the high-symmetry points in the BZ. The orbitals d_{xz} and d_{yz} that constitute the Fermi pockets (ii) transform, respectively, under the B_{2g} and B_{3g} irreducible representations of the site symmetry group D_{2h} for the $3f$ atomic Wyckoff positions (shown in Fig. 4). As such, they form two sets of three bands with opposite mirror eigenvalues and a mirror-symmetry-protected Dirac cone along the Γ–M line, hence giving rise to an upper and lower Van Hove filling (indicated by the red box in Fig. 4) with opposite sublattice parity. The proposed effective TB Hamiltonian reads (X. Wu *et al.*, 2021)

$$H_0 = \sum_{\mathbf{k}s\alpha} \epsilon_\alpha c^\dagger_{\mathbf{k},s,\alpha} c_{\mathbf{k},s,\alpha} - \sum_{\mathbf{k}sl\alpha} t_\alpha \Phi_{sl}(\mathbf{k}) c^\dagger_{\mathbf{k},s,\alpha} c_{\mathbf{k},l,\alpha} - t' \sum_{\mathbf{k}sl} \Phi_{sl}(\mathbf{k}) \nu_{sl} (c^\dagger_{\mathbf{k},l,xz} c_{\mathbf{k},s,yz} - c^\dagger_{\mathbf{k},l,yz} c_{\mathbf{k},s,xz}), \quad (6)$$

with $s, l = A$, B, and C and $\alpha = xz$ and yz. In Eq. (6) ϵ_α denotes the crystal-field splitting and the operator $c^\dagger_{\mathbf{k},s,\alpha}$ ($c_{\mathbf{k},s,\alpha}$) creates (annihilates) an electron on orbital α on sublattice site s with momentum $\mathbf{k}$. Further, $\Phi_{sl}(\mathbf{k}) = 1 + e^{-2i\mathbf{k}\cdot\mathbf{d}_{sl}}$ are the lattice structure factors, with $\mathbf{d}_{sl}$ the sublattice-connecting vectors. They obey $\Phi_{sl}(\mathbf{k}) = (1-\delta_{sl})\Phi^*_{ls}(\mathbf{k})$. The transformation of the B_{2g} and B_{3g} orbitals under the site symmetry group demands that the sign structure of the third term in Eq. (6) is ensured by $\nu_{AC} = \nu_{CB} = -\nu_{AB} = 1$ and $\nu_{sl} = -\nu_{ls}$. Figure 4 shows that the model is capable of faithfully capturing the electronic behavior of AV_3Sb_5 kagome metals in the energy region around the chemical potential, reproducing the nature and dispersion of the two VHSs at the M point as well as the mirror symmetry-protected Dirac crossing along the Γ–M line.

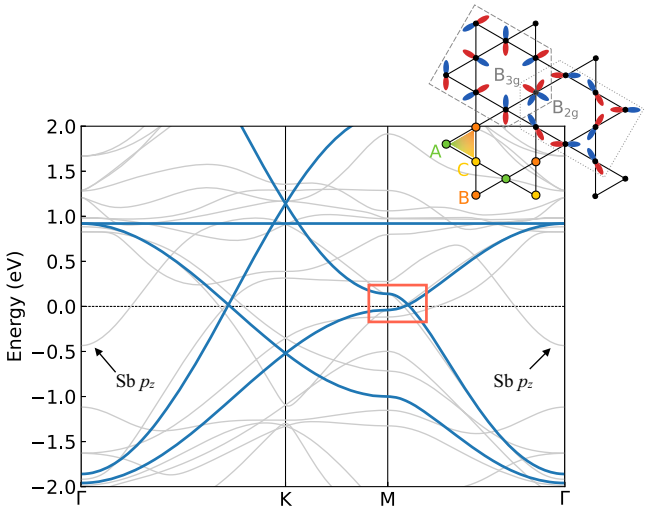

FIG. 4. Eigenvalues of the two orbitals per site model of Eq. (6) (blue lines) overlaying the band structure as obtained from the first-principles calculations in the absence of SOC (gray lines) for KV_3Sb_5. The red box highlights the energy-momentum region where the multiple VHSs of both p-type and m-type character emerge below and above the Fermi level, respectively. Inset: real-space structure of the kagome V plane where the sign structure (blue or red lobes) and spatial orientation of the B_{2g} and B_{3g} orbitals is shown on the different lattice sites. Around the Γ point, the arrows identify the electron pocket originating from the p_z orbital of the Sb atom located at the center of the hexagon of the kagome lattice. Inset adapted from X. Wu *et al.*, 2021.

This model has been used as the noninteracting platform for refined random phase approximation (RPA) analysis of superconducting instabilities (see Sec. III.C for details), to interpret ARPES experiments on the twofold nature of VHSs (Kang *et al.*, 2022) and to predict the existence of possible chiral excitonic order (Scammell *et al.*, 2023). An extension of the model to include the electron pocket at the Γ point that derives from the central Sb p_z orbital and is clearly detected in photoemission measurements (Ortiz *et al.*, 2020; Kang *et al.*, 2022) has also been proposed (X. Wu *et al.*, 2021). However, numerical calculations suggest that its contribution to the superconducting properties of AV_3Sb_5 kagome metals is marginal, while measurements under nonhydrostatic pressure point toward a strong correlation between a monoclinic structural transition, the termination of the second high-pressure superconducting dome and the removal of the Sb p_z electron pocket from the Fermi surface (Tsirlin *et al.*, 2023).

An extension of the aforementioned model includes an additional V d_{xy} orbital represented by a Wannier state in the A_g irreducible representation of D_{2h} formed by a linear

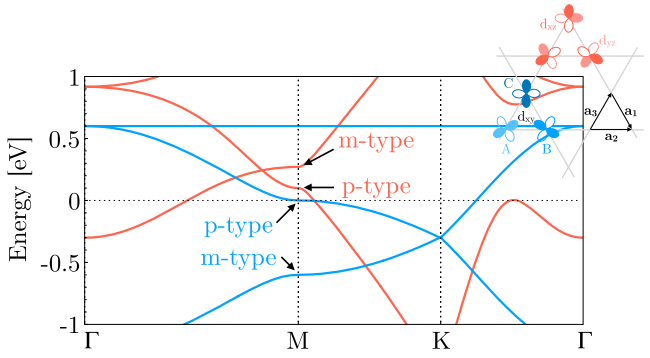

FIG. 5. Band structure induced by d_{xy} (blue lines) and d_{xz}/d_{yz} (red lines) orbitals on the kagome lattice (see the inset) and the corresponding pure and mixed nature of the VHSs. Adapted from Denner, Thomale, and Neupert, 2021.

combination of d_{xy}, $d_{x^2-y^2}$, and d_{z^2} orbitals (Denner, Thomale, and Neupert, 2021). Figure 5 shows the band dispersion of such a model, and crossings between the d_{xy} (blue) bands and the d_{xz}/d_{yz} (red) bands are protected by mirror symmetry. The coexistence of two *p*-type and one *m*-type VHS near the Fermi level has been confirmed by recent ARPES measurements of the CsV_3Sb_5 kagome metal (Kang *et al.*, 2022). The three bands forming these states at the *M* point have been named $K1$, $K2$, and $K2'$, and their location in the proximity of the Fermi level could set the stage for electronic symmetry breaking (Denner, Thomale, and Neupert, 2021; Kang *et al.*, 2022).

One further model for the AV_3Sb_5 kagome metals worth mentioning was proposed by Deng, Zhang *et al.* (2023) and based on the identification of elementary band representations (EBRs) (Bradlyn *et al.*, 2017; Cano *et al.*, 2018; Elcoro *et al.*, 2021). This model is built considering an orbital with A_g symmetry on each kagome site, i.e., V $d_{x^2-y^2}$, and an orbital with A_2'' symmetry, i.e., p_z, on all Sb atoms on the hexagonal "graphenelike" sublattice. This model, called two-EBR graphene-kagome model, captures the dispersion of the two low-energy VHSs and correctly describes the overall nontrivial band topology of AV_3Sb_5 materials.

3. Extended models

The electronic structures of realistic kagome materials are complicated and involve many orbitals and bands at the Fermi level. Strongly simplified models, such as those described in Secs. II.A.1 and II.A.2, while capable of describing general band structure features in a qualitative way, fail to give quantitative descriptions. To overcome this drawback and to bring the faithfulness of TB approaches closer to that of first-principles calculations, more realistic models have been developed where not only the multiorbital nature of kagome-like atoms but also the atomic environment are accounted for. In fact, the importance of interorbital hybridization and of grouping the $d_{x^2-y^2}/d_{xy}$, d_{xz}/d_{yz}, and d_{z^2} orbitals was recognized in earlier studies of kagome metals (Kang *et al.*, 2020a; Okamoto *et al.*, 2022; Kim and Liu, 2023) that highlighted how orbital symmetry and hybridization strongly influence the emergence of flat bands and VHSs.

As another material specific example, a comprehensive understanding of the complicated electronic properties of the *XY* family of kagome metals (discussed in Sec. IV.A), where *X* is a 3*d* transition metal such as Fe and Co and *Y* is a main group element such as Sn or Ge, was proposed by Jiang *et al.* (2025) on a strategy based upon band decomposition and orbital grouping. Each of the three groups is formed by separating the *d* orbitals of *X* in combination with specific orbitals of *Y* based on chemical and symmetry analyses. Within each group an analytical understanding of the band structures can be obtained. The resulting three decoupled effective TB models quantitatively reproduce the quasiflat bands, VHSs, and Dirac points of *XY* kagome metals (Kang *et al.*, 2020a, 2020b).

More specifically, Jiang *et al.* (2025) split the five kagome *X d* orbitals into the three groups $(d_{xy}, d_{x^2-y^2})$, (d_{xz}, d_{yz}), and d_{z^2} because the M_z mirror symmetry prevents any planar hybridization between the orbitals of the first two groups, whereas the hopping terms between the $(d_{xy}, d_{x^2-y^2})$ and d_{z^2} orbitals, although allowed by symmetry, can be neglected. These three groups are then combined with specific orbitals of *Y* atoms, as depicted in the insets of Fig. 6. Indeed, first-principles calculations confirm (1) large overlap and σ-like bonding between the *X* $(d_{xy}, d_{x^2-y^2})$ and trigonal *Y* (p_x, p_y) orbitals [Fig. 6(a)], (2) large overlap and π-like bonding between the *X* (d_{xz}, d_{yz}) and trigonal as well as hexagonal *Y* p_z orbitals [Fig. 6(b)], and (3) sizable overlap between the *X* d_{z^2} orbitals and the sp^2 bonding state of honeycomb *Y* atoms [Fig. 6(c)].

In matrix form the total TB Hamiltonian becomes (Jiang *et al.*, 2025)

$$\mathcal{H}^0_{\mathbf{k}} = H_{d_{z^2}}(\mathbf{k}) \oplus \begin{bmatrix} H_{p^t_{xy}}(\mathbf{k}) & S_{p^t_{xy},\ d_{xy}}(\mathbf{k}) & S_{p^t_{xy},d_{x^2-y^2}}(\mathbf{k}) \\ & H_{d_{xy}}(\mathbf{k}) & S_{d_{xy},\ d_{x^2-y^2}}(\mathbf{k}) \\ \text{H.c.} & & H_{d_{x^2-y^2}}(\mathbf{k}) + H^{(2)}_{d_{x^2-y^2},\ p^h_z}(\mathbf{k}) \end{bmatrix} \oplus \begin{bmatrix} H_{p^h_z}(\mathbf{k}) + H^{(2)}_{p^h_z,d_{x^2-y^2}}(\mathbf{k}) & \mathbf{0} & S_{p^h_z,d_{yz}}(\mathbf{k}) \\ & H_{d_{xz}}(\mathbf{k}) + H^{(2)}_{d_{xz},p^t_z}(\mathbf{k}) & S_{d_{xz},d_{yz}}(\mathbf{k}) \\ \text{H.c.} & & H_{d_{yz}}(\mathbf{k}) \end{bmatrix}, \tag{7}$$

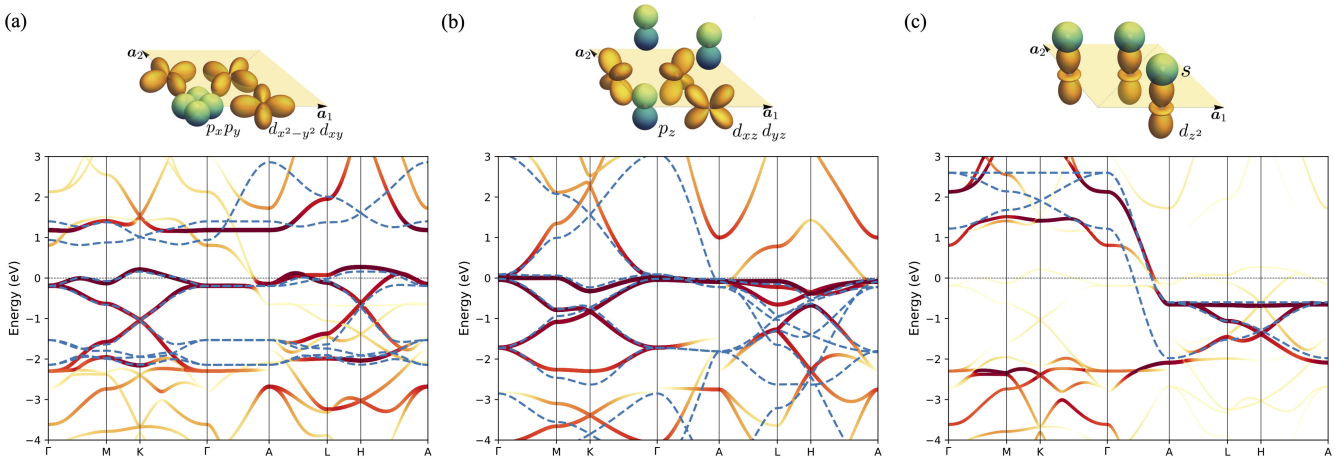

FIG. 6. Band structures of first-principles calculations (solid lines) and of the TB model in Eq. (7) (dashed blue lines) for the specific case of FeGe. The *ab initio* band structure has been computed in the paramagnetic phase of FeGe. (a)–(c) The three groups of Fe $(d_{xy}, d_{x^2-y^2})$, (d_{xz}, d_{yz}), and d_{z^2} orbitals, respectively. The darker the color of the bands, the stronger the character of the respective set of orbitals shown in the insets. Adapted from Jiang *et al.*, 2025.

where the blocks $H_i(\mathbf{k})$ along the diagonals derive from short-range hopping contributions of the corresponding orbital i ($p^t_{\dots}$ and $p^h_{\dots}$ refer to orbitals on the trigonal and honeycomb Y atoms, respectively), while the off-diagonal blocks $S_{i,j}(\mathbf{k})$ account for hybridization terms between different orbitals. The blocks $H^{(2)}_{i,j}(\mathbf{k})$ arise as corrections from second-order perturbation theory and are required to keep the Hilbert space of the model still manageable and to write Eq. (7) as the direct sum $\oplus$ of three independent terms. Their eigenvalues, shown in Fig. 6 as dashed blue lines overlaid to the *ab initio* band structures for the specific case of paramagnetic FeGe, quantitatively reproduce the quasiflat bands, VHSs, and Dirac points close to the Fermi level. Disagreements between the TB model and bands from first-principles calculations appear at high energies, putting forward Eq. (7) as a useful quantitative model to study low-energy physics in kagome metals.

The model in Eq. (7) for the XY kagome metals can be considered a Lego-like building block for the large family of RX_6Y_6 or "166" kagome materials in the paramagnetic phase, such as $R(\mathrm{Mn,V})_6\mathrm{Sn}_6$ (Peng *et al.*, 2021; Pokharel *et al.*, 2021; Arachchige *et al.*, 2022). The Hamiltonian of these 166 members can be obtained by doubling and perturbing the model in Eq. (7) because the 166 class materials RX_6Y_6 can be seen as a doubled X_3Y_3 material with an R atom inserted as a spacer in the middle honeycomb layer.

In addition to binary kagome metals, simplified models of ternary compounds such as AV_3Sb_5 also struggle to quantitatively capture several key aspects revealed by first-principles calculations and ARPES (Kang *et al.*, 2022). These include the sublattice character of the two VHSs close to the Fermi energy, the correct Fermi-surface orientation, and the multiorbital nature of the low-energy bands. To address these shortcomings, an extended Slater-Koster multiorbital formalism was developed by Zeng *et al.* (2025). This approach systematically incorporates the crystal-field environment of Sb atoms, employs a symmetry-adapted C_3-respecting orbital basis, and allows hybridization between orbitals of the same symmetry.

The Slater-Koster framework is based on six independent hopping parameters, effectively renormalizing the influence of the surrounding crystal environment while preserving orbital symmetries. A central advance of the Slater-Koster method over the simplified models of Secs. II.A.1 and II.A.2 is the explicit treatment of interorbital hopping, particularly between mirror-even and mirror-odd d orbitals. This mechanism explains the emergence of "mirror interorbital flat bands" (Zeng and Wang, 2024) and accounts for the anomalous double p-type VHSs observed in AV_3Sb_5. When intraorbital hoppings are included, these interorbital flat bands evolve into dispersive kagomelike bands that remain consistent with the double p-VHS scenario. The resulting Slater-Koster multiorbital models achieve excellent agreement with DFT and ARPES by reproducing the correct Fermi-surface shapes and orientations, the sublattice and orbital character of the VHSs, the multiorbital composition of the low-energy dispersions across the BZ, and higher-order VHS dispersions that are consistent with experimental fits (Zeng *et al.*, 2025).

B. Effect of spin-orbit interaction

To study the physics of kagome lattices in the presence of SOC, one needs to expand the spinless basis of the model in Eq. (1) to $\Psi^\dagger_{\mathbf{k}\sigma} = (c^\dagger_{\mathbf{k},1}, c^\dagger_{\mathbf{k},2}, c^\dagger_{\mathbf{k},3}) \otimes (\uparrow,\downarrow)$ to include the spin degree of freedom. In the absence of SOC, at $1/3$ filling the lowest band $E^{(1)}_{\mathbf{k}}$ in Fig. 2(b) is filled and the low-energy electronic excitations of H_0 resemble those of graphene. A perturbation term bilinear in the fermionic operators that breaks the SU(2) spin symmetry while preserving both the translational symmetry and the TRS of H_0 is the spin-orbit interaction that induces hopping between next-nearest-neighbor (NNN) sites (Guo and Franz, 2009). It takes the form

$$H_{\mathrm{SO}} = i\frac{2\lambda_{\mathrm{NNN}}}{\sqrt{3}} \times \sum_{\langle\langle (i,s)(j,l)\rangle\rangle\sigma\sigma'} (\mathbf{d}^1_{ij} \times \mathbf{d}^2_{ij}) \cdot c^\dagger_{i,s,\sigma}\boldsymbol{\sigma}_{\sigma\sigma'}c_{j,l,\sigma'}, \quad (8)$$

where λ_{NNN} is the NNN SOC strength, $c^{\dagger}_{i,s,\sigma}$ ($c_{i,s,\sigma}$) creates (annihilates) an electron in the unit cell i, the sublattice site s, and the spin σ and $\langle\langle (i,s)(j,l)\rangle\rangle$ denotes all next-nearest neighbors. $\mathbf{d}^{1,2}_{ij}$ are nearest-neighbor vectors traversed between NNN pairs (i,s) and (j,l), and $\boldsymbol{\sigma}$ is the vector of Pauli spin matrices. Because the vectors $\mathbf{d}^{1,2}_{ij}$ all lie within the x-y plane, only the σ^z Pauli matrix appears in Eq. (8), and the spin-orbit Hamiltonian H_{SO} decouples for the two spin projections along the z axis. As such, the motif of NNN hoppings that are induced by the SOC [Fig. 7(a)] resembles that of the Haldane or Kane and Mele models of graphene (Haldane, 1988; Kane and Mele, 2005a, 2005b).

Transforming Eq. (8) in momentum space, the spin-orbit Hamiltonian reads

$$\mathcal{H}^{\mathrm{SO}}_{\mathbf{k}} = \pm i 2\lambda_{\mathrm{NNN}} \times \begin{bmatrix} 0 & \cos\mathbf{k}\cdot(\mathbf{a}_2+\mathbf{a}_3) & -\cos\mathbf{k}\cdot(\mathbf{a}_3-\mathbf{a}_1) \\ & 0 & \cos\mathbf{k}\cdot(\mathbf{a}_1+\mathbf{a}_2) \\ & & 0 \end{bmatrix}, \quad (9)$$

where the plus (minus) sign refers to spin-up (spin-down) electrons. As shown in Fig. 7(b), the SOC opens up a gap at the Dirac point. The magnitude of such a gap scales linearly with the strength of the SOC, amounting to $\Delta_{\mathrm{SO}} = 4\sqrt{3}|\lambda_{\mathrm{NNN}}|$. H_{SO} also opens up a gap at the touching point between the flat band $E^{(3)}$ and the dispersing band $E^{(2)}$ coming up from the Dirac point; see Fig. 7(b).

The Hamiltonian that governs the low-energy excitation in the vicinity of the K point acquires a mass term $m_{\pm} = \pm 2\sqrt{3}\lambda_{\mathrm{NNN}}$ taking the form $h_{\mathbf{k}\pm} = v_{\mathrm{F}}(\tau_3 k_x + \tau_1 k_y) + \tau_2 m_{\pm}$. Furthermore, performing a numerical diagonalization of the lattice Hamiltonian $\mathcal{H}^0_{\mathbf{k}} + \mathcal{H}^{\mathrm{SO}}_{\mathbf{k}}$ in a strip geometry, one obtains a spectrum that is characterized by the presence of spin-filtered gapless states associated with each edge, as reported in Fig. 7(c). These states traverse bulk gaps that both have been opened up by the SOC and are hallmarks of a topologically nontrivial ground state at both 1/3 and 2/3 filling. In this respect, with SOC the electronic structure cannot be smoothly deformed into that of a trivial insulator, and explicit calculations show that it possesses

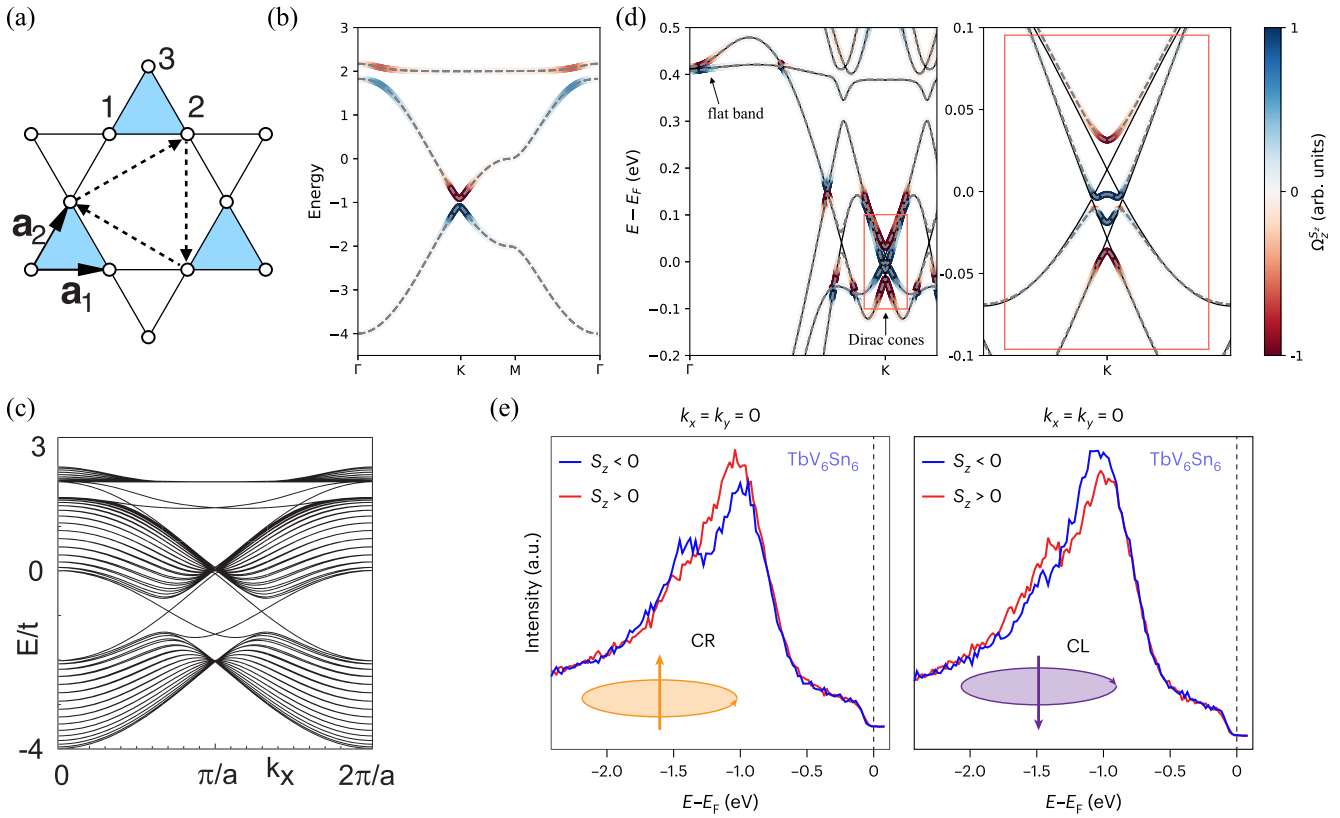

FIG. 7. (a) In the presence of SOC, spin-up electrons hopping between next-nearest-neighbor sites with amplitude $i\lambda_{\mathrm{NNN}}$ when moving in accordance to the dashed arrows and $-i\lambda_{\mathrm{NNN}}$ when moving against. For spin-down electrons, the arrows are reversed. (b) SOC opening a gap at the Dirac cone and at the touching point between the dispersing and flat bands. Concomitantly, a finite spin-Berry curvature $\Omega^{S_z}_z$ arises at those gaps. (c) Band structure of the kagome model in open boundary conditions featuring the appearance of topological edge states at both gaps. (d) First-principles band structure of TbV_6Sn_6 kagome metal without (solid black line) and with (dashed gray line) SOC. Red and blue highlight $\Omega^{S_z}_z$ as in (b). Right panel: close-up view of the Dirac cone region. (e) Circular right (CR) and circular left (CL) spin-resolved ARPES energy distribution curves (EDCs) measured for the spin-up ($S_z > 0$; red curves) and spin-down ($S_z < 0$; blue curves) channels in TbV_6Sn_6. The EDCs were acquired at the center of the BZ, with the incident light confined entirely to the sample's mirror plane. Under these conditions geometric contributions to the circular dichroism can be reliably ruled out. (a),(c) Adapted from Guo and Franz, 2009. (e) Adapted from Di Sante *et al.*, 2023.

a nontrivial $\mathbb{Z}_2$ invariant (Kane and Mele, 2005a; Fu, Kane, and Mele, 2007; Guo and Franz, 2009).

The block diagonal form of the spin-orbit Hamiltonian in Eq. (8), as far as the spin projection along the z component is concerned, allows one to compute the $\mathbb{Z}_2$ invariant as the parity of the spin Chern number C_s of the bands of interest

$$C_s = \frac{C_\uparrow - C_\downarrow}{2} = \frac{1}{2\pi}\int_{BZ} d\mathbf{k}\Omega_z^{S_z}(\mathbf{k}), \tag{10}$$

where $C_\sigma, \sigma = \uparrow, \downarrow$ is the Chern number for the specific spin block of Eq. (8) and $\Omega_z^{S_z}(\mathbf{k})$ is the spin-Berry curvature (SBC) (Xiao, Chang, and Niu, 2010). Figure 7(b) demonstrates how the momentum-space regions in proximity of the gaps opened up by SOC are characterized by a sizable SBC. Numerical integration of $\Omega_z^{S_z}(\mathbf{k})$ as in Eq. (10) gives $C_s = 1, 0$, and -1 for bands $E^{(1)}$, $E^{(2)}$, and $E^{(3)}$, respectively. This analysis proves the topological nature of the ground state at $1/3$ and $2/3$ filling.

Beyond the simplified model, the preceding argument is also valid for realistic kagome metals. For example, Fig. 7(d) reports the first-principles band structure of TbV_6Sn_6, a member of the 166 family (Peng *et al.*, 2021; Rosenberg *et al.*, 2022). SOC opens up several gaps throughout the entire spectrum and, as relevant to our discussion, specifically in the regions of the flat band at the $\mathbf{\Gamma}$ point and Dirac cones at the K point. The bands in the vicinity of those gaps feature a pronounced spin-Berry curvature $\Omega_z^{S_z}(\mathbf{k})$, even if the underlying electronic description is more complicated than that provided by the simple TB model of Eqs. (1) and (8). Recently, the fingerprints of a finite spin-Berry curvature in TbV_6Sn_6 kagome metals were experimentally addressed by looking at spin-resolved circular dichroism in the wide energy region of the occupied flat band, about 1 eV below the chemical potential (Di Sante *et al.*, 2023). The spin asymmetry in both right- and left-polarized dichroic signals, shown in Fig. 7(e), can be taken as an indication of a finite spin-Berry curvature (Schüler *et al.*, 2020). As for the Dirac cone region, a spin-dependent orbital Zeeman shift of bands observed in quasiparticle interference (QPI) scanning tunneling microscopy (STM) was also attributed to a nonvanishing $\Omega_z^{S_z}$ (Li *et al.*, 2024).

Unlike the lattice model on the hexagonal lattice, electrons on the kagome lattice can also experience a first nearest-neighbor (NN) spin-orbit interaction (Tang, Mei, and Wen, 2011; Ma *et al.*, 2020). The reason is that the electric field from neighboring ions felt during the nearest-neighbor hopping on the kagome lattice is no longer perfectly compensated. Nevertheless, its presence does not qualitatively change the previously addressed physical picture. Both NN and NNN SOC terms open up a gap at the Dirac point as well as in the flat-band region, giving rise to a finite spin-Berry curvature.

The main quantitative difference between the two types of spin-orbit interactions appears when one looks at the symmetries of Bloch states at the high-symmetry points for the flat band, as dictated by its topological quantum chemistry (Bradlyn *et al.*, 2017; Cano *et al.*, 2018). They are $\{\bar{\Gamma}_7, \bar{M}_6, \bar{K}_9\}$ and $\{\bar{\Gamma}_8, \bar{M}_6, \bar{K}_9\}$, depending on whether NN or NNN SOC is considered (Ma *et al.*, 2020). However, in both cases the symmetry-data vectors cannot be decomposed into a linear combination of EBRs that, as it is topologically equivalent to atomic orbitals, is topologically trivial. In this respect both forms of spin-orbit interaction lead to topological flat bands characterized by a nontrivial $\mathbb{Z}_2$ invariant. The coexistence of these topological flat bands and Dirac bands elevates the kagome lattice to one of the most interesting forums in the study of certain fundamental physical phenomena, such as high-T_c SC (H. Chen *et al.*, 2021; Zhao, Li *et al.*, 2021) and the fractional quantum Hall effect (Neupert *et al.*, 2011; Sun *et al.*, 2011; Tang, Mei, and Wen, 2011).

C. Phonons in the kagome lattice

The fundamental equations that govern the physics of periodic lattices, whether they describe electronic, phononic, or photonic degrees of freedom, show striking similarities, hinting at the possibility of a correspondence between phenomena occurring on a given lattice across different classes of systems ranging from ionic crystals to metamaterials (Kane and Lubensky, 2014; Lu, Joannopoulos, and Soljačić, 2014; Yang *et al.*, 2015; Huber, 2016; Xue, Yang, and Zhang, 2022). To cite a few specific examples, the analogy between the TB Hamiltonians of electrons in a crystal, such as those introduced in Sec. II.A, and the stiffness (or dynamical) matrix of lattice vibrations has led to the observation of mechanical topological helical states at the edge of a large lattice of coupled pendula (Süsstrunk and Huber, 2015). The analogy between the electron Hamiltonian and the Laplacian of an electric circuit has fostered the prediction and discovery of topoelectrical circuits (Imhof *et al.*, 2018; Lee *et al.*, 2018). In this framework, as with their electronic counterparts, mechanical vibrations of atoms or phonons in the kagome lattice feature rich physics. For instance, spring-mass models consisting of a periodic arrangement of springs and point masses serve as a simple platform to realize phenomena of topological nature governed by Newtonian equations of motion (Kane and Lubensky, 2014).

Within this description the motion of point masses is described by the dynamics of a variable $\vec{u}_{i,s}$, which identifies the displacement of the mass in unit cell i and sublattice $s = 1$, 2, and 3. Indeed, the notation used here is equivalent to that of TB Hamiltonians in Eqs. (1) and (8). For simplicity, assuming that all atoms in the lattice have the same unitary mass, the Lagrangian that governs the motion of point masses is that of coupled harmonic oscillators. It reads

$$\mathcal{L} = \tfrac{1}{2}\sum_{i,s,\mu}(\dot{u}^\mu_{i,s})^2 - \tfrac{1}{2}\sum_{\langle(i,s)(j,l)\rangle}\sum_{\mu,\nu}(u^\mu_{i,s} - u^\mu_{j,l})\mathcal{K}^{\mu\nu}_{is,jl}(u^\nu_{i,s} - u^\nu_{j,l}), \tag{11}$$

where, as usual, $\langle(i,s)(j,l)\rangle$ refers to the pairs of first-nearest neighbors and $\mu, \nu = x, y$ are Cartesian coordinates in a two-dimensional space. $\mathcal{K}^{\mu\nu}_{is,jl}$ is the spring-constant matrix and encodes the geometry of the lattice. The Euler-Lagrange equations for $u^\mu_{i,s}$, i.e., $d/dt(\partial\mathcal{L}/\partial\dot{u}^\mu_{i,s}) - \partial\mathcal{L}/\partial u^\mu_{i,s} = 0$, give the equation of motion

$$\ddot{\vec{u}} + \mathcal{D}\vec{u} = 0, \tag{12}$$

where $\vec{u}$ is the column vector formed by $\vec{u}_{i,s}$ and $\mathcal{D}$ is the real-space dynamical matrix

$$\mathcal{D}^{\mu\nu}_{is,jl} = -\mathcal{K}^{\mu\nu}_{is,jl} + \sum_{\langle (i,s)(k,o)\rangle} \mathcal{K}^{\mu\nu}_{is,ko}\delta_{ij}\delta_{sl}, \tag{13}$$

which is proportional to the spring-constant matrix and where the second term, clearly diagonal in the sublattice index, is needed to enforce the acoustic sum rule (Grosso and Parravicini, 2013). $\mathcal{D}$ is a real and symmetric matrix. If we assume that each mass point oscillates at frequency ω, i.e., $u^{\mu}_{i,s} = e^{i\omega t}\epsilon^{\mu}_{i,s}$, Eq. (12) reads

$$-\omega^2\vec{\boldsymbol{\epsilon}} + \mathcal{D}\vec{\boldsymbol{\epsilon}} = 0, \tag{14}$$

giving a real-space eigenvalue problem for the matrix $\mathcal{D}$, whose eigenbasis is $\vec{\boldsymbol{\epsilon}}$ and whose eigenvalues are ω^2. Further imposing translational invariance, $\epsilon^{\mu}_{i,s} = 1/N_{\mathbf{q}}\sum_{\mathbf{q}} e^{i\mathbf{q}\cdot\mathbf{R}_i}\epsilon^{\mu}_{\mathbf{q},s}$, where $\mathbf{q}$ belongs to the first BZ, Eq. (14) becomes

$$-\omega^2_{\mathbf{q}}\epsilon^{\mu}_{\mathbf{q},s} + \sum_{l}\Gamma^{\mu\nu}_{sl}(\mathbf{q})\epsilon^{\nu}_{\mathbf{q},l} = 0, \tag{15}$$

whose solution gives the phonon dispersion relation $\omega_{\mathbf{q}}$ and the phonon vibrational modes $\vec{\epsilon}_{\mathbf{q},s}$. The matrix Γ is named the momentum-space dynamical matrix and appears as the lattice Fourier transform of $\mathcal{D}$,

$$\Gamma^{\mu\nu}_{sl}(\mathbf{q}) = \sum_{j}\mathcal{D}^{\mu\nu}_{0s,jl}e^{i\mathbf{q}\cdot\mathbf{R}_j}, \tag{16}$$

whose matrix dimension depends only on the number of atoms in the unit cell and its independent Cartesian coordinates.

For the explicit case of interest here, i.e., the spring-mass model on the nearest-neighbor kagome lattice depicted in Fig. 8(a), the momentum-space dynamical matrix is a 6×6 matrix, owing to the three sublattices and the two spatial coordinates x and y. The complete form of Γ is

$$\Gamma^{\mu\nu}_{sl}(\mathbf{q}) = \begin{bmatrix} D_1 & -\gamma_{12}(\mathbf{q}) & -\gamma_{13}(\mathbf{q}) \\ & D_2 & -\gamma_{23}(\mathbf{q}) \\ & & D_3 \end{bmatrix}, \tag{17}$$

with

$$\gamma_{12}(\mathbf{q}) = Q\begin{bmatrix} 1 & 0 \\ 0 & 0 \end{bmatrix}(1 + e^{-i\mathbf{q}\cdot\mathbf{a}_1})$$

$$\gamma_{13}(\mathbf{q}) = Q\begin{bmatrix} \frac{1}{4} & \frac{\sqrt{3}}{4} \\ \frac{\sqrt{3}}{4} & \frac{1}{4} \end{bmatrix}(1 + e^{-i\mathbf{q}\cdot(\mathbf{a}_1+\mathbf{a}_2)})$$

$$\gamma_{23}(\mathbf{q}) = Q\begin{bmatrix} \frac{1}{4} & -\frac{\sqrt{3}}{4} \\ -\frac{\sqrt{3}}{4} & \frac{1}{4} \end{bmatrix}(1 + e^{-i\mathbf{q}\cdot\mathbf{a}_2}).$$

Denoting the aforementioned 2×2 matrices in $\gamma_{ij}(\mathbf{q})$ as $\boldsymbol{A}$, $\boldsymbol{B}$, and $\boldsymbol{C}$, respectively, the diagonal blocks of Γ read $D_1 = 2Q(\boldsymbol{A}+\boldsymbol{B})$, $D_2 = 2Q(\boldsymbol{B}+\boldsymbol{C})$, and $D_3 = 2Q(\boldsymbol{A}+\boldsymbol{C})$ in order to enforce the acoustic sum rules. The entries in $\boldsymbol{A}$, $\boldsymbol{B}$, and $\mathbf{C}$ originate from the projections of the Cartesian atomic displacements along the nearest-neighbor bonds of the kagome lattice. The parameter Q determines the strength of the spring constant, as in Fig. 8(a), and sets the overall energy scale (of lattice vibrations) in complete analogy to the hopping parameter t in the electronic Hamiltonian of Eq. (1). The resulting phonon band structure is shown in Fig. 8(b). It features a Dirac-like dispersion at the K point and VHS at the M point.

Despite its simplicity, this simple model of lattice vibrations on the kagome geometry can account for interesting nontrivial

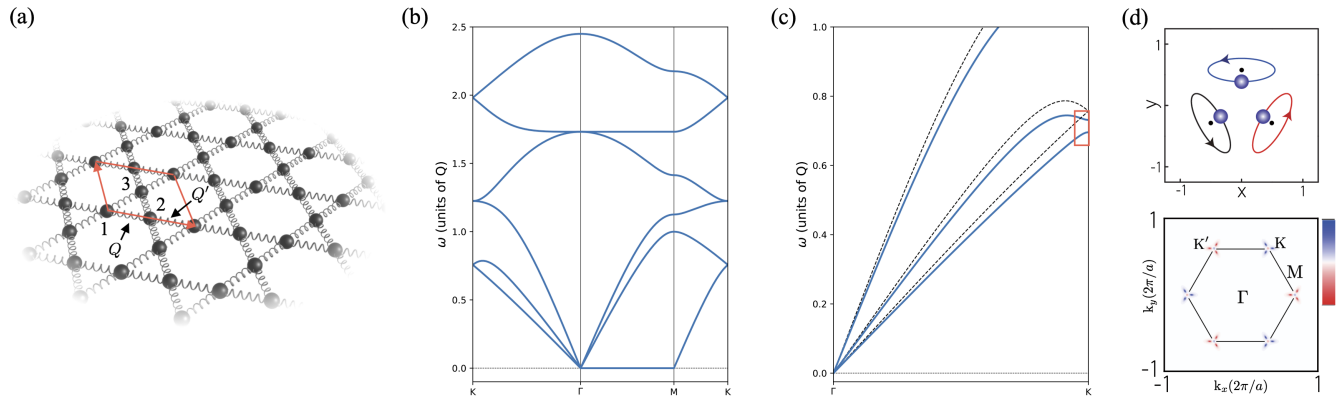

FIG. 8. (a) Nearest-neighbor spring-mass model in the kagome lattice. The red lines identify the kagome unit cell with the three-sublattice sites. Q and Q' set the strengths of the spring constant. (b) Phonon band dispersion in the $\mathcal{PT}$-symmetric $Q = Q'$ limit, featuring Dirac cones between the first and second bands, as well as between the fifth and sixth bands. The simplified nearest-neighbor model also features a flat band along the Γ–M direction. (c) Enlargement showing the phonon dispersion when inversion symmetry $\mathcal{P}$ is broken by differentiating the intra-unit-cell Q and inter-unit-cell Q' spring constants. In this specific case, $Q'/Q = 0.8$. The dashed black line refers to the $\mathcal{P}$-symmetric case $Q'/Q = 1$, as in (b). (d) Top panel: phonon eigenmode $\vec{\boldsymbol{\epsilon}}_{\mathbf{K},s}$ at the K point for each of the three sublattice sites $s = 1$, 2, and 3 for the first phonon branch, highlighting the chiral nature of the atomic displacements. Bottom panel: calculated phonon Berry curvature in momentum space for the same phonon branch. (c),(d) Adapted from Chen *et al.*, 2019.

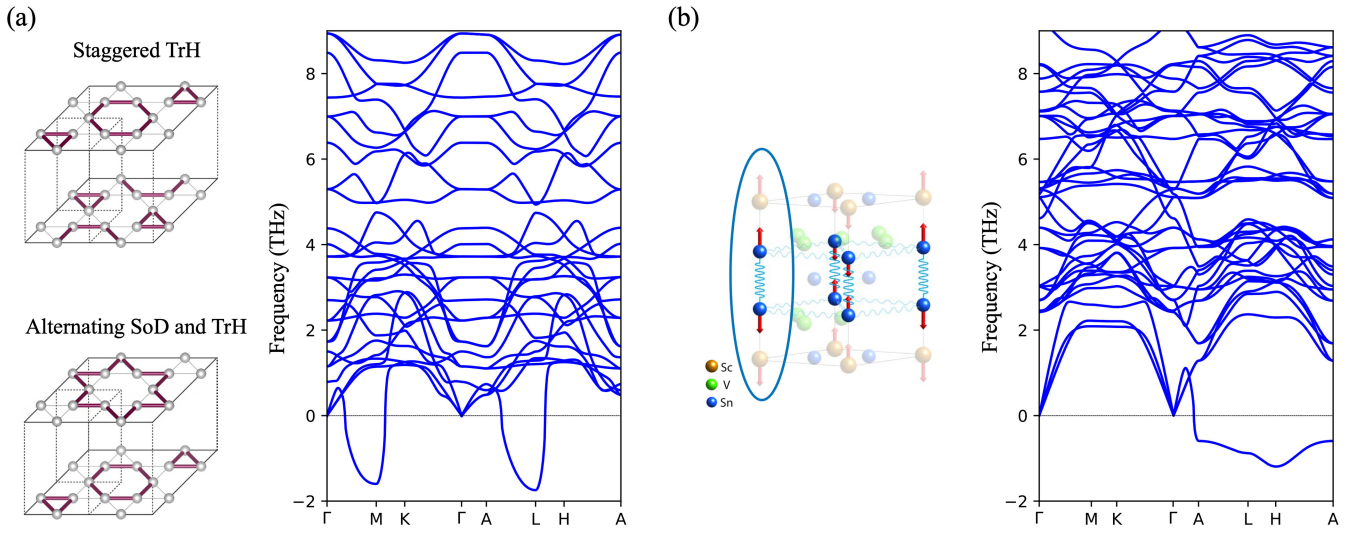

FIG. 9. (a) *Ab initio* phonon band dispersion of CsV_3Sb_5, characterized by imaginary phonon frequencies at the M and L points. The crystal structures show the expected in-plane modulation of vanadium atoms for $(K, Rb)V_3Sb_3$ (staggered TrH) and CsV_3Sb_5 (alternating SoD and TrH). (b) *Ab initio* phonon band structure of ScV_6Sn_6, characterized by a flat imaginary phonon band whose eigenmode primarily affects the out-of-plane vibration of Sn and Sc atoms. Adapted from Kang *et al.*, 2023, and Hu *et al.*, 2025.

topological effects when specific symmetry-breaking terms are included. For instance, when one differentiates between intra-unit-cell (Q) and inter-unit-cell (Q') spring constants, the model breaks inversion symmetry $\mathcal{P}$ while maintaining the overall C_3 rotational symmetry. This has noticeable effects on the topological properties of the model. In fact, the Berry curvature is even under the action of $\mathcal{P}$, while it is odd under TRS $\mathcal{T}$.

When both $\mathcal{P}$ and $\mathcal{T}$ are present, the Berry curvature vanishes. Breaking $\mathcal{P}$ via $Q \neq Q'$, a consequence of a weak trimerization seen in some kagome metals (Nakatsuji, Kiyohara, and Higo, 2015; Huimin Zhang *et al.*, 2023), results in a gap opening of the Dirac cones at the K valleys shown by the red box in Fig. 8(c). The vibration eigenmodes describe chiral phonons [top panel in Fig. 8(d)] (Chen *et al.*, 2019), a concept theoretically predicted in the graphene-type honeycomb lattice (Zhang and Niu, 2015) and experimentally verified in a monolayer of the transition-metal dichalcogenide WSe_2 (Zhu *et al.*, 2018), where the phonon eigenmodes at the Brillouin zone corner have a well-defined sense of chirality and quantized phonon pseudoangular momentum.

In contrast to the honeycomb lattice, however, chiral phonons on the kagome lattice include motion of all three sublattices with the same chirality, and the vibration orbit can take an elliptical shape. Moreover, these chiral phonons possess a valley-contrasting Berry curvature that is sharply peaked at the K and K' points, as depicted in the bottom panel of Fig. 8(d). This is the basis of the topological phonon Hall effect (Strohm, Rikken, and Wyder, 2005; Sheng, Sheng, and Ting, 2006; Kagan and Maksimov, 2008; Wang and Zhang, 2009; Zhang *et al.*, 2010), i.e., the phonon analogue to the anomalous Hall effect (AHE) in electron systems. Besides chiral phonons, variants of the simple nearest-neighbor spring-mass model can also support mechanical analogues to the quantum spin Hall effect (Chen *et al.*, 2018) and higher-order topological phases (Wakao *et al.*, 2020).

When it comes to the study of phonon dispersions in actual kagome materials, quantum mechanical first-principles methods are preferred to simplified spring-mass models. To substantiate this, we now discuss two notable cases of AV_3Sb_5 and ScV_6Sn_6 kagome metals for which an extensive *ab initio* investigation was performed to unveil the origin of their CDW instabilities.

In the first example, an in-plane lattice distortion of the kagome lattice is often energetically favorable and characterized via a multi-q distortion at inequivalent M points. Interactions between the lattice planes are possible in three-dimensional compounds, leading to a rich spectrum of possible distortion modes. As reviewed in more detail in Sec. IV.B.2, AV_3Sb_5 kagome compounds exhibit such a CDW instability (Ortiz *et al.*, 2020; H. Li *et al.*, 2021; Ortiz, Teicher *et al.*, 2021), embodied by these energetically favored breathing modes in the kagome plane (Tan *et al.*, 2021; Consiglio *et al.*, 2022). The in-plane distortion is identified by a breathing mode into a star-of-David (SoD) or trihexagonal (TrH) modulation. *Ab initio* phonon modeling fully captures both the SoD and TrH patterns, as shown in Fig. 9(a), with the preferred distortion modes including in-plane M-point modes, along with L-point modes that add an out-of-plane modulation to the CDW structure (Christensen *et al.*, 2021; Tan *et al.*, 2021).

The energy differences between various distortion types are small, with the predicted distortion mode being the staggered TrH arrangement, which involves the combination of the three $\mathbf{q}$ vector $(\mathbf{M}, \mathbf{L}, \mathbf{L})$ modes for $(K, Rb)V_3Sb_5$, and an alternating SoD and TrH arrangement that comprises $(\mathbf{L}, \mathbf{L}, \mathbf{L}) + (\mathbf{M}, \mathbf{M}, \mathbf{M})$ modes for CsV_3Sb_5 (Kang *et al.*, 2023); see the inset of Fig. 9(a). First-principles calculations of the phonon dispersion of AV_3Sb_5 kagome metals under external pressure (Zhang, Liu, and Lu, 2021; Consiglio *et al.*, 2022) were also able to faithfully reproduce the observed reduction of the CDW distortion (K. Chen *et al.*, 2021; Du *et al.*, 2021;

N. N. Wang *et al.*, 2021; Yu, Ma *et al.*, 2021), diagnosed in the calculation by a decrease—and an eventual disappearance—of the imaginary phonon softening at the M and L points.

As a second example, another common distortion type is an out-of-plane chain instability that can couple to the kagome plane in a secondary manner. Discussed in greater depth in Sec. IV.B.3, ScV_6Sn_6 is an experimental realization of this distortion type (Arachchige *et al.*, 2022). Here, in contrast to the previous example of AV_3Sb_5, the distortion of ScV_6Sn_6 distortion is characterized primarily by a displacement of out-of-plane Sc and Sn atoms accompanied by a weak modulation of the kagome-network V atoms. This is driven by the electron-phonon interaction and the softening of a flat phonon mode related to an out-of-plane vibration of Sn atoms (Cao *et al.*, 2023; Korshunov *et al.*, 2023; Tuniz *et al.*, 2023; Hu *et al.*, 2024; S. Lee *et al.*, 2024). As shown in Fig. 9(b), the first-principles calculation of the phonon spectrum of ScV_6Sn_6 agrees well with the experimental observations, predicting the presence of an unusually flat imaginary phonon band whose eigenmode weight comprises the out-of-plane vibration of Sn and Sc atoms (Tuniz *et al.*, 2023, 2025; Hu *et al.*, 2025).

III. MANY-BODY PHENOMENA

The kagome lattice, with its inherent geometric frustration and intriguing electronic structure, provides an exceptional setting for many-body interactions that give rise to a diverse landscape of emergent quantum phenomena. Beyond the previously explored single-particle band structure features, kagome metals exhibit rich physics driven by electron-electron and electron-lattice interactions. These many-body effects can not only modify the electronic states but also stabilize novel ordered phases that are highly sensitive to doping, temperature, and external perturbations.

Here we discuss the theoretical aspects behind key many-body phenomena observed in kagome metals. We begin with a discussion in Sec. III.A on CDWs, which often emerge in response to Fermi-surface nesting and lattice instabilities, manifesting as periodic modulations in the electronic density. Then, in Sec. III.B we delve into SC, a central theme in the study of kagome systems, particularly in compounds like AV_3Sb_5, where unconventional pairing mechanisms and nontrivial topology are believed to play a role.

In Sec. III.C we then examine the more exotic concept of a PDW, wherein the superconducting order parameter itself exhibits spatial modulation, an intriguing possibility in systems with competing orders and strong correlations. The role of electron-phonon interactions is also scrutinized in Sec. III.D, especially given their relevance to both CDW formation and SC. Finally, in Sec. III.E we consider electronic correlations and fluctuating local moments, which underpin much of the emergent behavior in kagome systems, contributing to magnetic fluctuations and possible non-Fermi liquid behavior.

A. Charge orders

We start with an imperative comment on the terminology of different orders. The systems of interest are often multiband (with electron and hole bands), multiorbital, and moderately spin-orbit coupled. Therefore, CDWs and SDWs, flux orders, and even exciton condensates are not sharply differentiated concepts. We therefore use the umbrella term *charge orders* here. All of them are electron-hole condensates, i.e., the order parameter takes the general form

$$\Delta_{\alpha,\beta;\mathbf{q}}(\mathbf{k}) \sim \langle c^{\dagger}_{\mathbf{k}+\mathbf{q},\alpha} c_{\mathbf{k},\beta} \rangle, \tag{18}$$

where α and β are compound indices including spin, orbital, and sublattice degrees of freedom. The center of mass momentum $\mathbf{q}$ is set as a subscript to indicate that the order parameter is typically nonzero only for a small set of discrete $\mathbf{q}$, while it has a continuous dependence on the relative momentum $\mathbf{k}$ (Nayak, 2000).

In general, charge orders can also appear at $\mathbf{q} = 0$, as long as they break other symmetries besides translation (for example, in nematic phases if the flux order in the Haldane model is spontaneously generated).[1] The $\mathbf{k}$ dependence, if breaking lattice symmetries by itself, would justify calling the charge order unconventional and may be categorized by a finite *angular momentum* that it carries (which is meaningful only modulo the rotation symmetry of the crystal). A nontrivial $\mathbf{k}$ dependence is typically associated with an order parameter that renormalizes—in a TB picture—the hopping integrals rather than only on-site terms and is therefore also referred to as a bond order.

Another important symmetry distinction is whether the order breaks TRS. Time-reversal symmetry breaking through complex hopping amplitudes will induce spontaneous ring currents and is therefore also called the *flux phase*. Such orbital magnetism would generally, because of SOC, also induce spin magnetism, and therefore a spin density wave. Whether a phase should be termed flux order or spin density wave depends on the primary driver for the time-reversal breaking order, but this is not always a well-defined question.

Among the charge ordering phenomena, those occurring in the AV_3Sb_5 family are the most studied and perhaps the most puzzling (Christensen *et al.*, 2021, 2022; Tan *et al.*, 2021; Ritz, Fernandes, and Birol, 2023; Enzner *et al.*, 2025; Holbæk and Fischer, 2025). We therefore focus our description primarily on effective theories applying to the situation found there, namely, two-dimensional orders on the kagome lattice with a 2×2 enlarged unit cell (Grandi *et al.*, 2023; Wagner *et al.*, 2023). Building on these theories, we can comment on how these orders couple into three-dimensional structures. Such a symmetry-based description can be connected to microscopic models (Christensen *et al.*, 2022).

We restrict our discussion to the spinless case, focusing on the point group C_{6v} instead of the double groups. We focus on ordering momenta $\mathbf{q} \in \{\mathbf{M}_1, \mathbf{M}_2, \mathbf{M}_3\}$ corresponding to the three M points. This enlarges the point group by four

[1]This distinction of $\mathbf{q} = 0$ and finite $\mathbf{q}$ phases is more widespread in SC, where a finite $\mathbf{q}$ order is a Fulde-Ferrell-Larkin-Ovchinnikov phase (Fulde and Ferrell, 1964; Larkin and Ovchinnikov, 1964) or a PDW (Agterberg *et al.*, 2020), while a $\mathbf{k}$ dependence that breaks lattice symmetries is often referred to as an unconventional superconductor with nonzero angular momentum (p wave, d wave, etc.).

TABLE I. Character table of the group C_{6v}''' (Venderbos, 2016). The one- and two-dimensional irreducible representations preserve the translation symmetry of the original kagome lattice, while the three-dimensional irreducible representations lead to a 2×2 increase in the unit cell.

	I	t_i	C_2	t_iC_2	C_3	C_6	σ_v	$t_i\sigma_v$	σ_d	$t_i\sigma_d$
$\lvert\mathcal{C}\rvert$	1	3	1	3	8	8	6	6	6	6
A_1	1	1	1	1	1	1	1	1	1	1
A_2	1	1	1	1	1	1	−1	−1	−1	−1
B_1	1	1	−1	−1	1	−1	1	1	−1	−1
B_2	1	1	−1	−1	1	−1	−1	−1	1	1
E_1	2	2	−2	−2	−1	1	0	0	0	0
E_2	2	2	2	2	−1	−1	0	0	0	0
F_1	3	−1	3	−1	0	0	1	−1	1	−1
F_2	3	−1	3	−1	0	0	−1	1	−1	1
F_3	3	−1	−3	1	0	0	1	−1	−1	1
F_4	3	−1	−3	1	0	0	−1	1	1	−1

translations acting within the enlarged unit cell. We denote the new group by C_{6v}'''; its character table is listed in Table I. Any spinless charge order with translation symmetry breaking according to a 2×2 period in the two-dimensional plane will fall into one of the irreducible representations F_i, $i = 1, 2, 3,$ and 4, which are all of dimension 3. We further denote by F_i', $i = 1, 2, 3,$ and 4 TRS-breaking cousins of these orders. Determining which of F_i or F_i' is realized in a given system is thus the primary goal in understanding it.

Group-theory analysis (Venderbos, 2016; Wagner *et al.*, 2023) shows that on-site density orders on the kagome lattice sites can realize the irreducible representations F_1, F_3, and F_4, while bond orders on the nearest-neighbor kagome bonds can realize any F_i with $i = 1, 2, 3,$ or 4. Finally, flux orders on the plaquettes outlined by the nearest-neighbor kagome bonds can realize F_2' and F_4'. See Fig. 10 for pictorial representations of these orders.

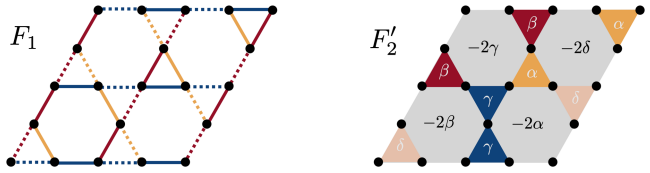

FIG. 10. Examples of orders with a 2×2 enlarged unit cell. Left sketch: bond order pattern in the irreducible representation F_1. Straight and dotted lines represent strong and weak bonds, respectively. The three colors represent different amplitudes of the bond modulations that together represent the three-dimensional order parameter of F_1. If all amplitudes are chosen to be equal, one obtains the TrH and SoD orders for positive and negative values of the order parameter, respectively. Right sketch: flux order pattern in irreducible representation F_2', where α, β, γ, and δ represent fluxes subject to the constraint $\alpha + \beta + \gamma + \delta = 0$. With this they represent the three-dimensional order parameter space of F_2'. Note that even though the magnetic flux through the 2×2 unit cell vanishes, this does not imply that the orbital magnetic moment of the state vanishes. [A well-known example where this is not the case is the Haldane model (Haldane, 1988).]

The effective free energy governing these orders has two notable features. First, it may contain third-order terms in the order parameters. This is enabled by the fact that the three momenta corresponding to the three components of the irreducible representations $F_i^{(\prime)}$, with $i = 1, 2, 3,$ and 4, add up to $0 = \mathbf{M}_1 + \mathbf{M}_2 + \mathbf{M}_3$, allowing for terms that transform trivially under translation. Considering the other symmetry constraints, such third-order terms exist only for F_1 individually, reading

$$\Delta_1\Delta_2\Delta_3, \tag{19}$$

where $(\Delta_1, \Delta_2, \Delta_3)$ is the three-dimensional vector order parameter associated with the three-dimensional irreducible representation F_1. The three components carry momenta $\mathbf{M}_1$, $\mathbf{M}_2$, and $\mathbf{M}_3$, respectively. The term in Eq. (19) in the free energy renders the transition of first order, regardless of whether the microscopic origin of the order is phononic or electronic. In addition, the following coupling terms between F_1 order and F_2' or F_4' are allowed:

$$\Delta_1\Delta_2'\Delta_3' + \Delta_1'\Delta_2\Delta_3' + \Delta_1'\Delta_2'\Delta_3, \tag{20}$$

where $(\Delta_1', \Delta_2', \Delta_3')$ is the three-dimensional order parameter of either F_2' or F_4'. Consider a scenario where the F_1 bond order is the primary instability and F_2' or F_4' have a comparably lower transition temperature. The effect of Eq. (20) in the free energy is to renormalize the transition temperature to higher values—the bond order thus promotes a secondary flux order. This is not the case for bond orders F_2, F_3, and F_4.

Some general conclusions can be drawn for the coupling of these orders to magnetic fields and in-plane strain. The lowest-order coupling term between an out-of-plane magnetic field B and the mentioned bond and flux orders is one that mixes a bond and a flux order, namely,

$$B(\Delta_1\Delta_1' + \Delta_2\Delta_2' + \Delta_3\Delta_3'). \tag{21}$$

It is symmetry allowed only for the combination of orders (F_1, F_2') and (F_3, F_4'). If we again consider the situation of a well-established F_1 order, the effect of Eq. (21) for $B \neq 0$ is to admix the F_2' flux order, even though this might not have an instability by itself (since it effectively acts as a first-order term for F_2'). This creates the intriguing phenomenology that a homogeneous magnetic field can be used to induce a staggered flux order, and reversal of the field orientation reverses the sign of the staggered flux. This is enabled by the presence of the F_1 order, which, owing to its symmetry breaking, renders the combination of F_1 and F_2' not perfectly *antiferromagnetic*, or free of net magnetization, but induces a finite magnetic moment in F_2' to which B can couple. A second feature of a phase with coexisting F_1 and F_2' orders is that it becomes anisotropic (in the kagome plane). This is true for both a mixed phase due to the coupling in Eq. (20) and one brought about by a magnetic field via Eq. (21). The latter scenario leads to a counterintuitive response: one starts with an isotropic F_1 order and applies a magnetic field that also has

the full rotation symmetry of the kagome lattice (and more). Yet, the resulting state is anisotropic.

In-plane strain explicitly breaks the rotation symmetry (down to twofold). However, the impact that this explicit symmetry breaking has on the electronic response of the system depends on the susceptibility of the system toward such an isotropy-breaking deformation. Since anisotropy arises from a combination of F_1 and F_2' orders, as previously explained, an enhanced strain response of the system appears if it is near a phase where the F_1 and F_2' orders coexist.

In this way responses of the system to external perturbations can be used to systematically argue about the irreducible representation(s) that its symmetry-breaking pattern realizes. They are independent of whether phonons or electronic interactions are the main driver of the instability. In this discussion we ignored the three-dimensional nature of the charge order for simplicity. Considering orders with nonvanishing momentum (translation symmetry breaking) perpendicular to the kagome planes will induce further constraints on possible terms in the free energy. For instance, if one only considers order parameters with π momentum in this direction (and the same in-plane momenta, i.e., L-point orders), one obtains no third-order terms in the free energy, as they would violate momentum conservation. The unusual coupling of bond and flux orders to the magnetic field remains, however.

For instance, in the AV_3Sb_5 family of compounds, experimental observations place clear constraints on the order that is realized. By perturbing CsV_3Sb_5 in a controlled way by strain and magnetic field, C. Guo *et al.* (2024) argued that the material is close to a phase where F_1 and F_2' orders coexist but, in its pristine form, realizes pure F_1 order. Xing *et al.* (2024) argued that RbV_3Sb_5 has a coexisting F_1 and F_2' order, and the specific configuration of the respective three-dimensional order parameters has been determined.

B. Superconductivity

In the same way that the community has tried to reconcile high-T_c cuprates from the perspective of doping a magnetically ordered Mott insulator (Lee, Nagaosa, and Wen, 2006), kagome metals suggest a scenario where a high-temperature itinerant charge order may seed superconducting order (Neupert *et al.*, 2022). A rather low T_c has recently been recorded for kagome metals at ambient pressure (Ortiz *et al.*, 2020; Ortiz, Sarte *et al.*, 2021; H. Yang *et al.*, 2024), ranging between 0.8–4 K, depending on the specific compound and the sample quality; see Fig. 11(a). This explains why a

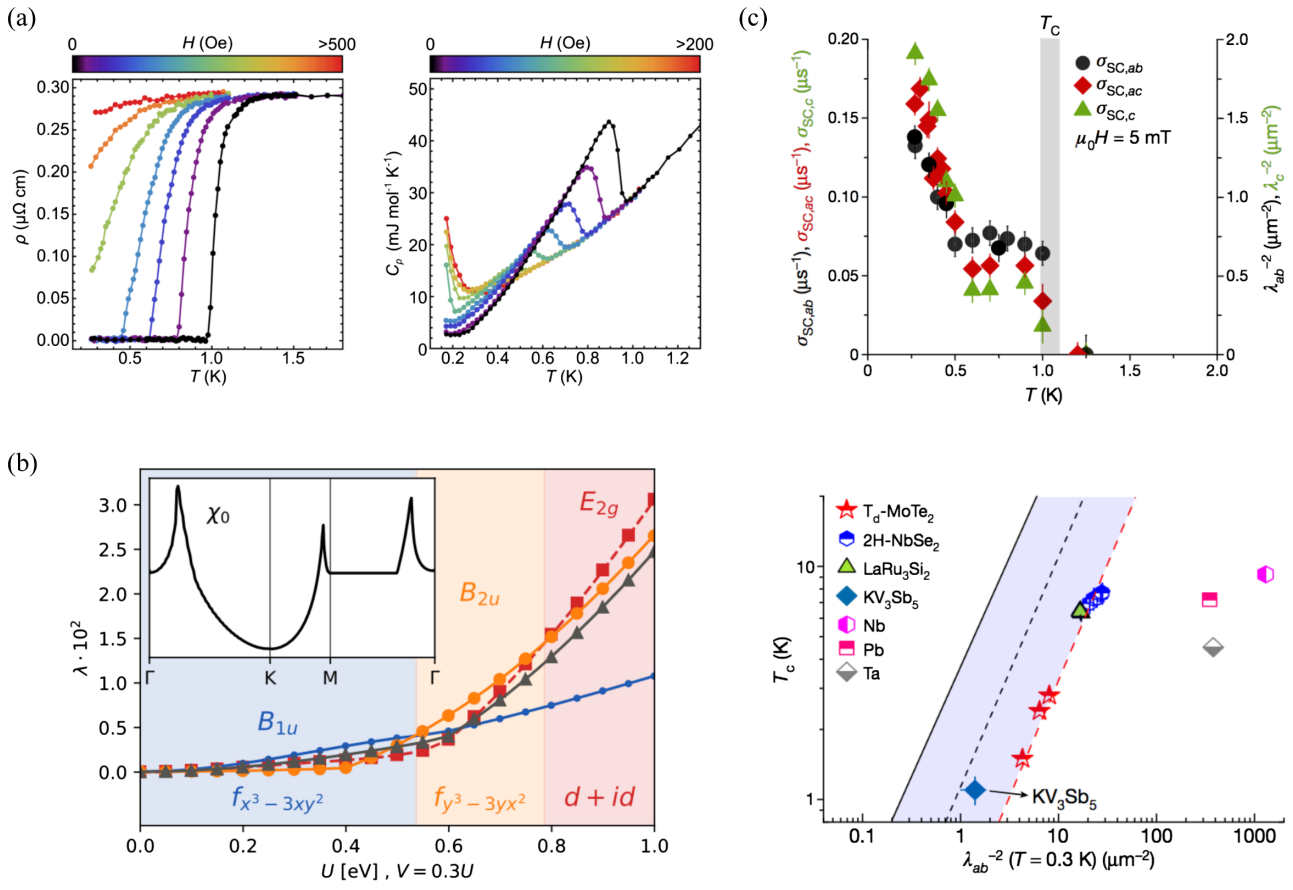

FIG. 11. SC in kagome metals. (a) Original resistivity and specific heat data obtained for KV_3Sb_5 featuring $T_c = 0.94$ K. (b) Theoretical predictions for an f wave and a chiral d wave for an all-electronic mechanism of SC in kagome metals. (c) Top panel: μSR scattering rates and penetration depth measurements for CsV_3Sb_5. Bottom panel: Uemura plot in comparison to other hexagonal superconductors, cuprate bounds (hole doping, straight black line; electron doping, dashed black line), and traditional Bardeen-Cooper-Schrieffer (BCS) superconductors. Adapted from Ortiz, Sarte *et al.*, 2021, X. Wu *et al.*, 2021, and Mielke *et al.*, 2022.

majority of experimental activity has focused thus far on exploring the nature of the high-temperature charge order rather than such low-T_c phases that evade certain spectroscopic methods. Furthermore, the intricacy of charge ordering cascades as a function of temperature renders it difficult to isolate an effective electronic model that SC originates from.

In the absence of strong magnetic fluctuations such as those observed in the majority of kagome metal compounds with local magnetic moments, phonon-mediated SC is a common suspect and cannot be excluded even though the electron-phonon coupling is estimated to be too small for the observed T_c in the 135 kagome metals (Tan *et al.*, 2021). From an electronically mediated microscopic mechanism of SC, kagome metals present themselves as weakly to intermediately correlated electron systems and suggest a high relevance of the VHS near the Fermi level (X. Wu *et al.*, 2021; Rømer *et al.*, 2022), combined with sublattice interference (Kiesel and Thomale, 2012), to explain the nature of superconducting pairing; see Fig. 11(b). Either way, the complicated nature of charge order and its concomitant Fermi-surface reconstruction has rendered it a difficult task to accomplish studies of superconducting order starting from a microscopically accurate charge-ordered itinerant parent state. From an Uemura plot of T_c versus penetration depth, muon spin relaxation (μSR) locates this kagome metal in the domain of unconventional SC; see Fig. 11(c).

From a synoptic viewpoint, the nature of SC in kagome metals appears to be strongly compound and family dependent and appears to navigate between an all-phononic and an all-electronic pairing mechanism. It is likely that SC can be quantitatively accounted for only through taking into account phonons and electronic correlations on a similar footing (Q.-G. Yang *et al.*, 2024).

C. Pair density wave

A PDW is a SC condensate that also breaks translation symmetry besides particle conservation. The principle found its original conception in the cuprates (Agterberg *et al.*, 2020). One can differentiate between a strict and a more inclusive definition of a PDW. In the strict reading, one would require the translation symmetry to be restored at temperatures right above the SC transition, while in the more inclusive picture, SC appearing within a translation-breaking-ordered phase (such as charge order) is also termed PDW if a noticeable modulation of the SC order parameter is imprinted from the higher-temperature order. While PDWs had evaded unambiguous observation for a significant amount of time, recent discoveries in cuprates (Du *et al.*, 2020), UTe_2 (Q. Gu *et al.*, 2023), transition-metal dichalcogenides such as $NbSe_2$ (Liu *et al.*, 2021), and, in particular, the kagome metal CsV_3Sb_5 (H. Chen *et al.*, 2021; Deng *et al.*, 2024b) have significantly broadened the empirical basis for alleged PDWs.

A prototypical signature of a PDW results from the STM analysis of the pairing function above and below T_c, where the intertwined onset of SC and translation symmetry breaking would show up through additional Fourier moments at T_c. For CsV_3Sb_5, Fig. 12(a) depicts a comparison between the Fourier-transformed STM topography (top panel) versus the Fourier-transformed dI/dV map at 300 mK (bottom panel), i.e., deep in the superconducting regime of H. Chen *et al.* (2021). The additional purple peaks represent the additional translational symmetry breaking at $\mathbf{Q}_{3q-4a/3}$ assigned to the superconducting condensate. From theory, sublattice interference (Kiesel and Thomale, 2012) has been claimed to be pivotal in explaining the system's propensity for the formation of PDW SC (Wu, Thomale, and Raghu, 2023), while other mechanisms ascribe pivotal relevance to the tentative formation of loop current order (Zhou and Wang, 2022).

Presently, a key challenge in the unambiguous experimental identification of a PDW—in the strict previously mentioned sense—is the exclusion of a possible preceding reconstruction with the same ascribed Fourier moment above T_c. Ideally, Fourier data would be necessary as a function of temperature, scanned from above all the way to below T_c, and suggest the need for future additional exploration. In kagome metals the charge-ordered parent state within which the PDW appears is particularly intricate and exhibits a cascade of translation symmetry breaking through charge order. Notably, the reconstructed charge-ordered Fermi pockets trigger a Fourier moment similar to what has been ascribed to the PDW; see Fig. 12(b) from Li *et al.*, 2023(b).

Instilled by the nontrivial unit cell of the kagome lattice, alternative proposals such as sublattice-modulated superconducting pairing have been proliferating (Schwemmer *et al.*, 2024). There the superconducting order experiences modulations within the unit cell; they accordingly do not break translation symmetry but still yield a site-modulated profile similar to a PDW breaking other crystalline symmetries.

D. Electron-phonon interaction

In this section we provide a discussion of the impact of phonons on many-body states in kagome metals, with AV_3Sb_5 compounds used as an experimental touchstone. Although various superconducting pairing symmetries have been proposed, recent ARPES experiments have revealed distinct evidence of nodeless superconducting gaps in AV_3Sb_5 compounds (Zhong *et al.*, 2023b), placing significant constraints on the nature of the pairing mechanism. In addition, multiboson kinks in photoemission spectra were observed in both CsV_3Sb_5 and KV_3Sb_5 systems (H. Luo *et al.*, 2022; Luo *et al.*, 2023; Wu *et al.*, 2023; Zhong *et al.*, 2023a), showing contrasting behaviors across different electron bands, with some predominantly exhibiting a single kink and others displaying double kinks. These low-energy excitations are often attributed to strong electron-phonon (e-ph) coupling (Engelsberg and Schrieffer, 1963; Hengsberger *et al.*, 1999), although the connection between photoemission kinks and emergent electronic orders is not always straightforward. A well-known example is provided by copper oxide superconductors, where the e-ph interaction accounts for the ~70 meV photoemission kinks but is generally regarded as too weak to explain the high T_c and inconsistent with the nodal d-wave pairing symmetry (Z. Li *et al.*, 2021).

Initial first-principles calculations using DFT indicated a weak to moderate overall e-ph coupling $\lambda \approx 0.25$ in CsV_3Sb_5 at both ambient and elevated pressures (Tan *et al.*, 2021; Zhang, Liu, and Lu, 2021; Wang, Jia *et al.*, 2023), which fails

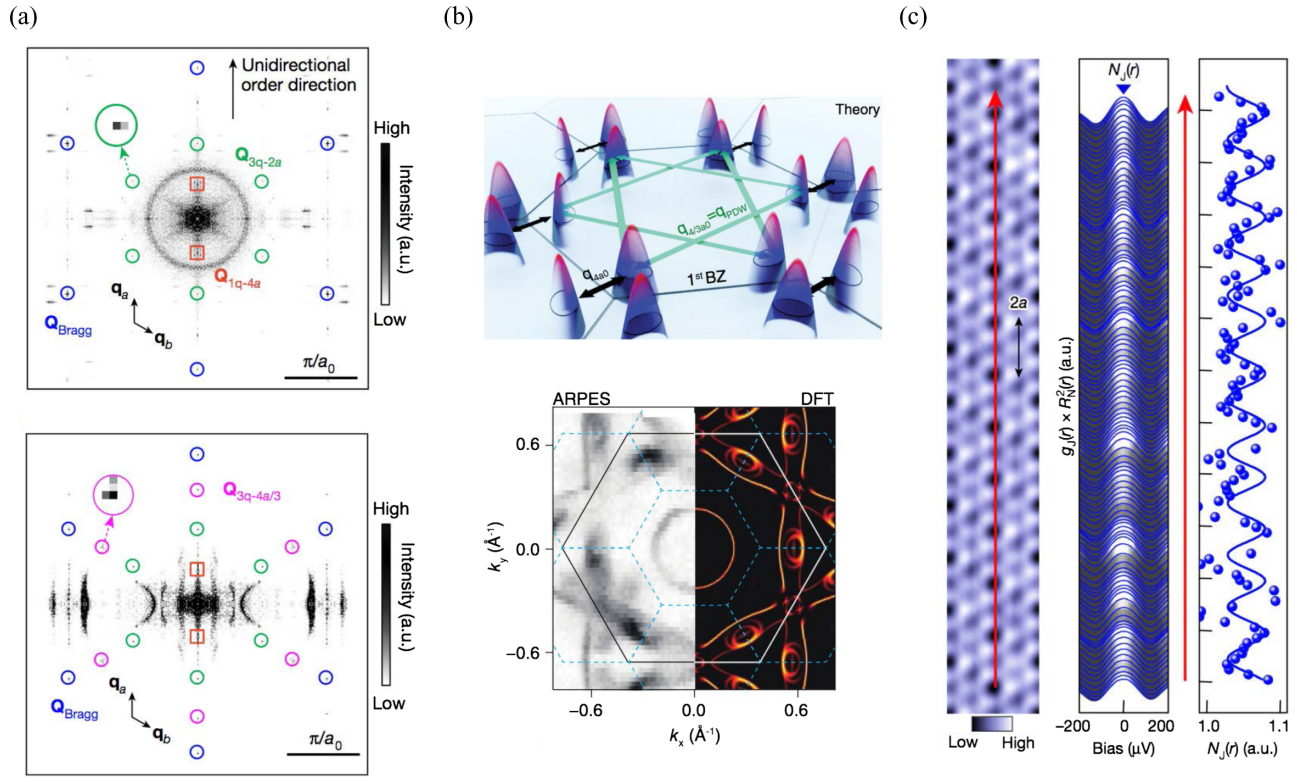

FIG. 12. Pair density wave order in kagome metals. (a) Original observation of onset ordering vectors $Q_{3q-4a/3}$ in the superconducting phase of CsV_3Sb_5. Adapted from H. Chen *et al.*, 2021. (b) Fermi pocket reconstruction from charge order. The nesting features suggest similarities to the observed onset order below T_c. Adapted from Li *et al.*, 2023b. (c) Josephson tunneling spectroscopy along a clean Sb-terminated KV_3Sb_5 crystal, where the spatial modulation of the SC pairing function becomes visible. Adapted from Deng *et al.*, 2024b.

to support the superconducting transition temperature $T_c \approx 2.6$ K and hinting at an unconventional electron-electron pairing mechanism for SC. Nevertheless, recent low-energy laser-based ARPES measurements reported evidence of anomalies (kinks) in the intensity and dispersion of the spectra for the Sb $5p$ and V $3d$ electronic bands near a binding energy of ≈32 meV.

Figure 13(a) (center panel) shows the ARPES intensity plots for the so-called α (Sb $5p$-derived) and β (V $3d$-derived) bands, where e-ph coupling-induced kinks are clearly visible. While the kink around ≈32 meV is evident on both α and β bands, an additional kink appears at a lower binding energy of ≈12 meV only on the β band. State-of-the-art GW-based many-body perturbation calculations demonstrated that e-ph coupling is the universal origin of those multiboson photoemission kinks (You *et al.*, 2025). The simulated spectral functions shown in Fig. 13(a) (left and right panels) reproduce the salient features of the experimental data with clear signatures of phonon-induced electron self-energy effects in the form of dispersion kinks (highlighted by the red arrows) and spectral width broadening. In fact, the α band displays a single kink around −32 meV, whereas the β band shows double kinks at −12 and −30 meV, respectively, which agrees well with the experimental measurements. The calculated atom-vibration-resolved real and imaginary parts of the e-ph self-energy attribute the kinks at ≈ − 30 meV and −12 meV primarily to V and Sb atom vibrations.

Ultrahigh-resolution, low-temperature ARPES experiments have also directly observed a nodeless, nearly isotropic, and orbital-independent superconducting gap in momentum space for two representative CsV_3Sb_5-derived kagome superconductors: $Cs(V_{0.93}Nb_{0.07})_3Sb_5$ and $Cs(V_{0.86}Ta_{0.14})_3Sb_5$ (Zhong *et al.*, 2023b). Figure 13(b) gives a schematic momentum dependence of the superconducting gap amplitude. Notably, this gap structure remains unaffected by the presence or absence of charge order in the normal state (Zhong *et al.*, 2023b). In agreement with the observed band dispersion kinks, the robust isotropic superconducting gaps with small $2\Delta/k_BT_c$ in the presence or absence of the CDW seem to be consistent with a conventional s-wave-driven and e-ph-coupling-driven pairing. This interpretation is further reinforced by the GW-based calculations reported in Fig. 13(c) (You *et al.*, 2025), which, within the framework of anisotropic Eliashberg theory, predict an almost isotropic angular distribution of gap functions that is consistent with experimental observations. Overall, ARPES experiments and state-of-the-art calculations support a conventional e-ph scenario of SC.

That said, in spite of supporting a fully gapped superconducting state, recent STM and μSR results provide evidence for TRS-breaking SC in $Cs(V,Ta)_3Sb_5$ and magnetism-induced modulation of Cooper pairs (Deng *et al.*, 2024a). It is, however, important to point out that the e-ph-driven SC is not incompatible with the recently observed PDWs in both CsV_3Sb_5 (H. Chen *et al.*, 2021) and TRS-breaking orders (Mielke *et al.*, 2022). Indeed, PDWs have been also observed

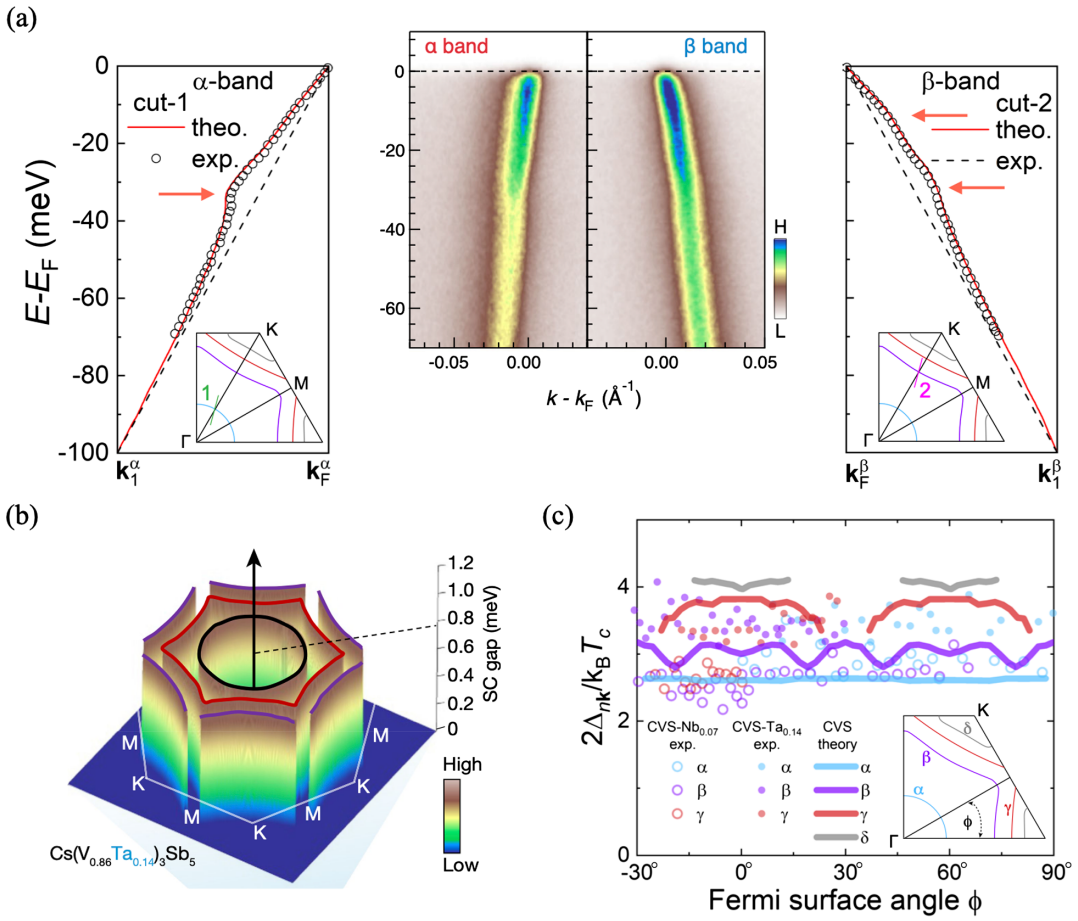

FIG. 13. (a) Left and right panels: momentum distribution cut-derived dispersion relation between experiments (open circles) and *GW* theory (red lines) for the α and β bands, respectively. The red arrows highlight the positions of the kinks in the photoemission data. Center panel: ARPES intensity plot. (b) Schematic momentum dependence of the superconducting gap amplitude of the $Cs(V_{0.86}Ta_{0.14})_3Sb_5$ sample. (c) Calculated and experimental angle distribution of the rescaled superconducting gaps $2\Delta/k_BT_c$ on multiple Fermi-surface sheets of CsV_3Sb_5-derived compounds within the $k_z = 0$ plane. Adapted from Zhong *et al.*, 2023a, 2023b, and You *et al.*, 2025.

in the conventional superconductor $NbSe_2$, where the pair density modulation is due to the real-space charge density modulation (Liu *et al.*, 2021).

Besides SC, strong *e*-ph coupling is potentially responsible for the appearance of a CDW order, specifically, when it is momentum dependent (Varma and Simons, 1983). Several experimental and theoretical studies support this scenario as a mechanism for the formation of the various charge orders in the AV_3Sb_5 family. In fact, although bulk sensitive hard-x-ray and neutron scattering showed the absence of soft phonons (H. Li *et al.*, 2021; Xie *et al.*, 2022), i.e., phonon modes whose frequency softens upon cooling toward a phase transition, Raman scattering measurements on CsV_3Sb_5 reported high-frequency amplitude modes that hybridize significantly with other lattice modes, thus indicating strong *e*-ph coupling within the CDW state (G. Liu *et al.*, 2022). To reconcile the experimental evidence with the potential lack of phonon softening, it was suggested that the CDW transition in the AV_3Sb_5 family is a weakly first-order transition without a continuous change of the lattice dynamics (Miao *et al.*, 2021).

At the theoretical level, DFT calculations revealed unstable phonon modes at the *M* and *L* points of the hexagonal BZ, with the softening of these modes proposed as the driving mechanism for the CDW formation (Christensen *et al.*, 2021; Tan *et al.*, 2021; Consiglio *et al.*, 2022), as shown in Fig. 9(a). Moreover, variational Monte Carlo simulations for the Hubbard model on the kagome lattice pointed to the pivotal role that electron-phonon coupling plays to stabilize the experimentally observed CDW phases in AV_3Sb_5 (Ferrari, Becca, and Valentí, 2022).

E. Correlations and fluctuating local moments

This section discusses the degree of electronic correlation in kagome metals, especially that of the 135 family. An unbiased approach to quantify the strength of the electron-electron interaction is to calculate the Coulomb tensor from first principles. Operatively, this can be done by defining a localized model spanning a given energy window of the band structure around the Fermi level and performing a constrained random phase approximation (cRPA) calculation. This excludes the screening effects within the so-called target manifold when the polarization of the system is calculated and yields the interaction parameters specific to that low-energy model. [For an overview of cRPA, see Aryasetiawan (2011).]

cRPA results for kagome metals have been reported for KV_3Sb_5 (Di Sante, Kim *et al.*, 2023) and CsV_3Sb_5 (Jeong

et al., 2022). In both cases the average values for the Kanamori-type intraorbital repulsion U and Hund's exchange J_{Hund} are approximately 6.1 and 0.5 eV, respectively, when screening is removed over the entire V $3d$ and Sb $5p$ manifolds. These values are significantly reduced to about 1.6 and 0.4 eV, respectively, when the target space is restricted to the V $3d$ orbitals only. Compared to oxides such as $SrVO_3$ and $LaVO_3$, the d bandwidth in the 135 kagome is larger and the energy distance to the p bands is a factor of 3 to 4 smaller, resulting in a much more pronounced covalency. Taking other kagome materials such as Ni_3In, FeSn, and $Co_3Sn_2S_2$ as a reference, the interaction values for KV_3Sb_5 are roughly a factor of 2 smaller. This all indicates a weak degree of correlation in the V compounds of the 135 family.

Di Sante, Kim *et al.* (2023) compared the decay of the Coulomb repulsion with the interatomic distance for the two different target spaces to other classes of materials. The results shown in Fig. 14 indicate a good degree of universality, despite the different absolute values of the interaction strengths.

In addition to cRPA calculations, one can estimate the degree of correlation from a comparison of experimentally measured quantities and theoretical calculations. Possibilities are offered by optical measurements, tunneling, or photoemission spectroscopies, which can be compared to corresponding first-principles calculations. In the cases where the experimental spectrum displays a gap that is not predicted by DFT or GW (and if long-range order can be ruled out at the temperatures of the measurements), the material qualifies as a candidate for a strongly correlated Mott insulator (Imada, Fujimori, and Tokura, 1998). According to this criterion, for instance, high-temperature superconducting cuprates are classified as Mott systems, as the pseudogap extends to zero doping and persists above the Néel temperature. Such a strong-coupling scenario can be immediately ruled out for both V-based 135 and V-based 166 kagome materials that display metallic bands in photoemission and well-defined Fermi surfaces. Using the ratio of the kinetic energy obtained from optics experiments and the kinetic energy from band theory as a proxy to the degree of correlation also puts the V-based 135 compounds in the same category as other weakly correlated itinerant systems (Zhou *et al.*, 2023).

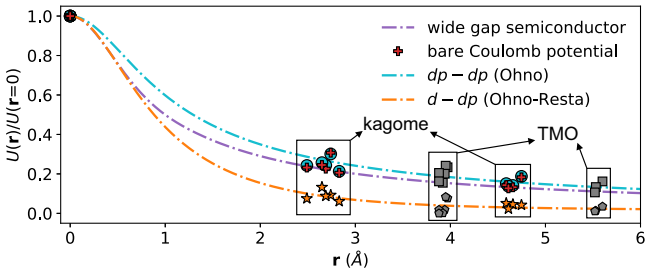

FIG. 14. Decay with the interatomic distance of the intraorbital Coulomb repulsion U normalized to the on-site strength and compared for two different choices for the target subspaces in cRPA calculations. The representative of the transition-metal-oxide (TMO) family are $LaVO_3$, $LaTiO_3$, and $LaCrO_3$, while KV_3Sb_5, Ni_3In, FeSn, and $Co_3Sn_2S_2$ are considered for the kagome class. From Di Sante, Kim *et al.*, 2023.

Therefore, more than one criterion points to a small degree of correlation in the V-based 135 compounds. Yet, because of their multiorbital nature, one could still ask whether the V-based kagome metals could be classified as "Hund's metals" (Georges and Kotliar, 2024), extending the definition given to iron-based superconductors and some transition-metal oxides. Hund's metals are also characterized by metallic single-particle spectra. Yet, their spin-spin correlation function reveals sizable instantaneous local magnetic moments that are long lived (Haule and Kotliar, 2009; Aichhorn *et al.*, 2010; Yin, Haule, and Kotliar, 2011; Dai, Hu, and Dagotto, 2012; Si, Yu, and Abrahams, 2016) and fluctuate in a way characteristic of systems close to a Mott transition (Hansmann *et al.*, 2010; Watzenböck *et al.*, 2020). Moreover, they display strong differentiation of the band renormalizations due to the orbital decoupling induced by the presence of J_{Hund} (de' Medici, Mravlje, and Georges, 2011; Georges, de' Medici, and Mravlje, 2013).

In analogy with many prototypical Hund's metals, the majority of the kagome materials discussed here constitute transition-metal elements of the fourth period (principal quantum number $n = 3$), and, as discussed in Sec. III, the kagome bands close to the Fermi level involve partially filled atomic shells with angular momentum $l = 2$. In general, this situation promotes the formation of large local magnetic moments. From an atomic point of view, electrons are indeed significantly confined because of the nodeless radial wave function with $l = n - 1$ (Georges, 2004).

However, when screening effects in the solid are included via cRPA, the intraorbital repulsion gets fairly suppressed, at least for V-based 135 materials. Yet, apart from the absolute value of the U parameter, we can sketch the main physical ingredients of a 135 kagome metal using the language of a microscopic Hubbard-like model, as in Fig. 15. This neglects

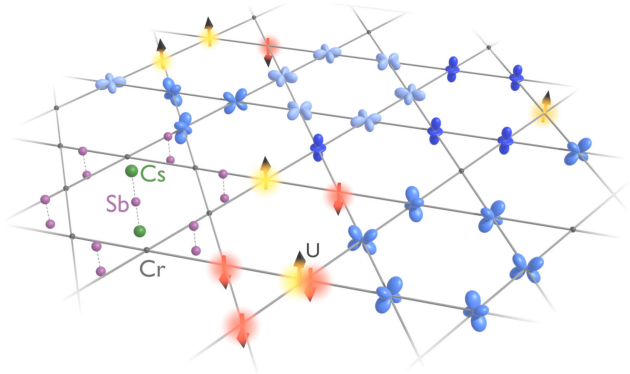

FIG. 15. Sketch of a kagome plane of Cr atoms (small gray sphere). The larger green and purple balls represent Cs and Sb, respectively, to portray the $CsCr_3Sb_5$ compound. On randomly selected kagome sites, some of the Cr $3d$ orbitals are drawn. Spin-up and spin-down electrons hop through the lattice, and when two of them occupy the same site, they pay an energy cost. Its value depends on whether they sit on the same or different orbitals. Exemplified is the case in which they occupy the same orbital, which means that they have opposite spins and repulsion U. This demotes electron's delocalization through the lattice and favors the formation of fluctuating local moments. Adapted from Sangiovanni, 2024.

for simplicity nonlocal interactions (see Fig. 14) and also assumes no long-range magnetic order.

The illustration in Fig. 15 highlights the specificity of the kagome lattice, which plays a role in determining the degree of correlation in these materials. As extensively discussed in Secs. II.A.1 and III, the geometric frustration of single-particle wave functions influences the electrons' localization on the kagome lattice. The resulting flat band with the associated singular DOS increases the impact of correlations. In fact, because the band velocity is proportional to the first derivative of the energy $E_{\mathbf{k}}$ with respect to momentum $\mathbf{k}$, bands that are flat host Bloch electrons that are enormously slowed down, even without consideration of the kinetic energy reduction effect driven by U (Vonsovskii, Katsnelson, and Trefilov, 1993; Mravlje *et al.*, 2011; Hausoel *et al.*, 2017).

One can therefore view the kagome lattice as a platform in which the level of itinerancy can be suppressed by one- and two-particle processes synergistically. The former can be roughly thought to be set by the ratio between U and the bandwidth W of the electronic manifold, or by better indicators sensitive to the presence of flat bands in the DOS—such as the second moment of the DOS (Bulla and Potthoff, 2000). Instead, at the two-particle level, the strength of the interaction matters in general, but the associated vertex corrections are crucially dependent on the filling of the correlated bands. This indeed determines the size of the phase space for the relevant many-body processes directly influencing the behavior of charge and spin fluctuations: the closer the localized orbitals are to half filling, the stronger the effective correlation. Borrowing jargon from meteorology, the filling has a role similar to humidity for the perceived temperature; i.e., it can enhance or reduce the effects of correlation (Crispino *et al.*, 2025).

There is a simple consequence to this: if it is possible to increase the number of d electrons with respect to known metals like V-based 135 and 166 compounds, there is a chance to reach a higher level of correlation. One way is to substitute Cr for V in the 135 compounds. This increases the nominal d occupation by 3 per formula unit, though the cRPA estimates would be influenced as well. At the present stage, the first indications indeed point to more relevant many-body correlations. For the recently synthesized $CsCr_3Sb_5$, Y. Liu *et al.* (2024) reported signatures of local magnetic moments and sizable spin fluctuations. Using a parton approach based on subsidiary spins, Xie *et al.* (2025) stressed the tendency toward orbital selectivity in which the d_{xz} orbital is the most correlated one and reaches quasiparticle renormalizations of between 2 and 10, depending on the interaction used.

This is in striking contrast to the V compounds for which both experiments (Kenney *et al.*, 2021) and theory (Zhao, Wu *et al.*, 2021) have reported no local moments. The latter DFT calculations with dynamical mean-field theory (DFT + DMFT) calculations for V-based 135, which are in agreement with those of Liu, Wang, and Zhou (2022), also indicate a weak electronic mass renormalization (smaller than 2) for KV_3Sb_5. This is true even if one focuses only on the d_{xz} orbital, which is the one that responds most sensitively to the electron-electron interaction in the V compounds. DFT + DMFT also indicates vanishing local moments and small mass renormalizations in the related ScV_6Sn_6 kagome metal (Yu *et al.*, 2024).

IV. MATERIALS CLASSES

In this section we provide an overview of the properties of key members of some of the more common classes of kagome metals. The phenomenology associated with each kagome compound is governed by the corresponding lattice frameworks, the nature of the atoms composing the kagome sublattice, the electron filling of the kagome bands, and the presence of other instabilities (native to other sublattices) that couple to the kagome framework. This results in a rich spectrum of phase behaviors across numerous classes of kagome metals.

We discuss key kagome metal classes by breaking them down via their chemical complexities, which govern the phenomena and tunability possible in each. As two elements are required to drive the formation of a kagome plane via distortions in close-packed hexagonal layers of single-element compositions (Kolli, Natarajan, and Van der Ven, 2021), the simplest class of kagome metals is binary compounds. Although this phase space is seemingly simple, binary kagome networks harbor an impressive range of complexity. This is governed by a combination of a stacking degree of freedom between kagome and nonkagome layers, which, in principle, can tune the dimensionality and the filling of the kagome network. The character of the kagome ion can further tune magnetism within the kagome network and gapping within the electronic band structure.

Additional elements introduced within the crystal network, for example, in ternary compounds, allow for new structural motifs that support interactions between the kagome network and other cation sublattices. Examples include added magnetic layers distinct from the kagome network that can couple to carriers and break symmetries within the kagome planes. Other examples include structural subunits that host bond order or steric instabilities that couple to and distort the kagome networks. Some of the more common ternary kagome compounds hosting some of these features are discussed in the second part of this section.

A. Binary structures

The binary kagome metal series T_mX_n ($T = 3d$ transition metal; $X =$ Sn, In, or Ge) has been instrumental in the early exploration of the physics of kagome metals. This family of compounds offers a versatile platform to study the interplay between the unique electronic structure of the kagome lattice and magnetism. A key feature of these materials is the presence of a structural layer hosting a kagome sublattice that is occupied by $3d$ transition-metal elements. The stacking arrangements of these kagome layers, interspersed with spacer layers (S) of X atoms, can be varied depending on the specific composition (the $m:n$ ratio in T_mX_n). This structural flexibility allows the tuning of interlayer interactions and the effective dimensionality of the electronic structure; see Fig. 16.

For instance, in the 3:1 structure (T_3X), the kagome layers exhibit an AB-type stacking where each layer is shifted

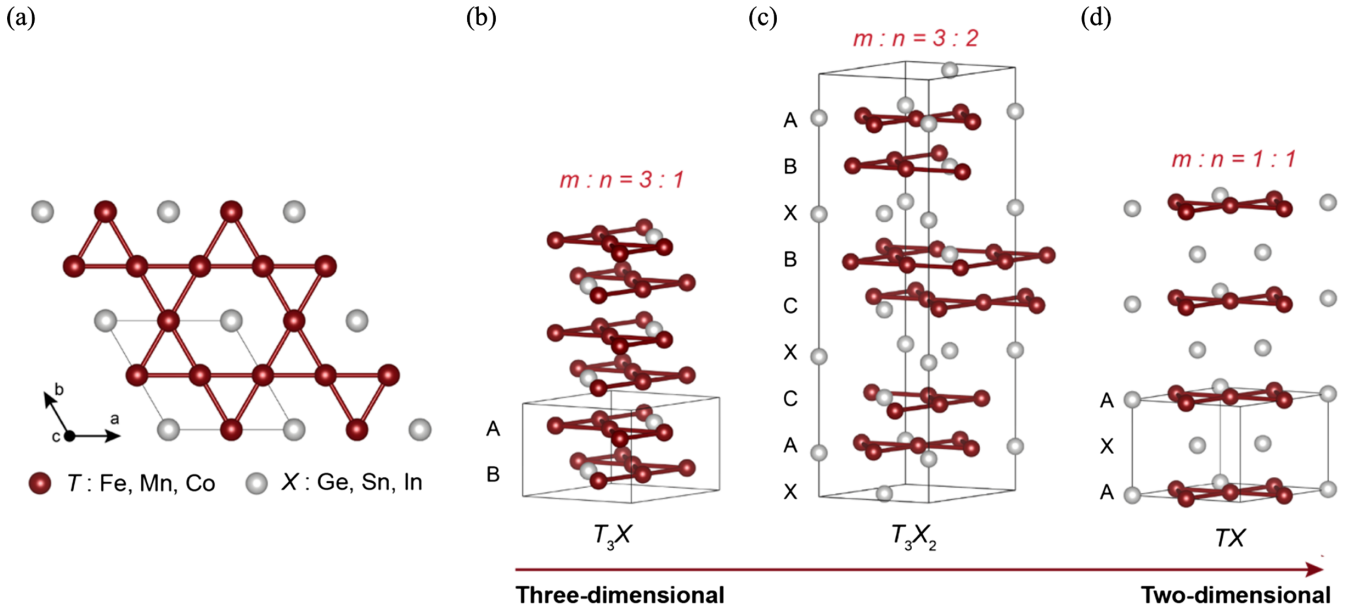

FIG. 16. (a) Top view of the kagome layer in the T_mX_n series. Stacking sequences of the T_mX_n series with (b) m:n = 3:1, (c) 3:2, and (d) 1:1 (d). The kagome layers (A, B, and C) exhibit different in-plane lattice offsets. The spacing layers S consist of X atoms. The dimensionality increases with the $X:T$ ratio. In the 1:1 structure (d), kagome layers are separated by the S layers, while in the 3:1 structure (b), neighboring kagome layers are stacked on top of each other. The 3:2 structure (c) exhibits a mixture of the two stacking types. Adapted from Kang *et al.*, 2020b.

laterally with respect to the neighboring one by half of a unit cell; see Fig. 16(b). Such a configuration, where downward-pointing triangles face upward-pointing triangles, naturally leads to strong interlayer interactions and a three-dimensional (3D) electronic structure. Consequently, some of the characteristic electronic features of an ideal 2D kagome lattice, such as Dirac fermions, are typically not observed in these materials. However, flat bands can partially survive in these structures even when interlayer hopping is allowed. In addition, some compounds from the 3:1 family defy conventional understanding by demonstrating a large intrinsic AHE without net magnetization arising from a noncollinear antiferromagnetic spin structure (Nakatsuji, Kiyohara, and Higo, 2015).

In the 3:2 structure (T_3X_2), interlayer interactions are partially reduced, allowing some characteristics of the 2D kagome electronic structure to emerge; see Fig. 16(c). In this stacking motif, kagome-bilayer units are stacked between the spacer layers, with a stacking sequence A-B-*S*-B-C-*S*-C-A-*S*. Fe_3Sn_2 is a prime example, as it was the first material where kagome-derived Dirac fermions were experimentally realized (Ye *et al.*, 2018; Yin *et al.*, 2018). The material also exhibits other interesting properties, such as room-temperature skyrmion bubbles and a topological Hall effect (Hou *et al.*, 2017).

Last, the 1:1 structure (TX) represents a configuration where kagome layers are most strongly decoupled, offering the closest environment to realize the prototypical electronic structure of a 2D kagome lattice; see Fig. 16(d). CoSn, a nonmagnetic kagome metal, displays ideal kagome flat bands with suppressed dispersion in all momentum directions (Kang *et al.*, 2020a). The intrinsic SOC lifts the degeneracy between the flat and Dirac bands, leading to topologically nontrivial flat bands. In contrast, the antiferromagnetic kagome metal FeSn displays a richer electronic structure with coexisting surface and bulk Dirac fermions alongside a magnetic flat band. The interplay between Dirac fermions and the unique magnetic structure in FeSn leads to symmetry-protected Dirac nodes that are robust against SOC (Kang *et al.*, 2020b). FeGe, which is closely related to FeSn, exhibits a different magnetic structure and features a 2×2 charge order coexisting with antiferromagnetism (AFM) (Teng *et al.*, 2022).

In summary, the binary kagome series T_mX_n has been an ideal playground to initiate and deepen the exploration of kagome metals. The diverse stacking configurations and the intrinsic properties of 3*d* transition metals allow for the realization of a broad array of electronic and magnetic phenomena, providing a fertile ground for further exploration of topological and correlated phases in kagome lattices.

1. Fe-based compounds: FeSn, Fe_3Sn_2, and FeGe

a. Fe_3Sn_2 *compounds*

The first kagome metal to have its electronic band structure extensively studied was Fe_3Sn_2. This material has attracted significant interest owing to its intriguing electronic, magnetic, and transport properties, all stemming from its geometrically frustrated kagome lattice. Crystals are typically prepared via chemical vapor transport methods (Malaman *et al.*, 1976).

Establishing the groundwork for understanding the magnetic properties of Fe_3Sn_2 (Malaman, Fruchart, and Le Caer, 1978), neutron diffraction, and magnetization measurements identified the compounds as ferromagnetic, with a notable spin rotation between 250 and 60 K. The magnetic properties of Fe_3Sn_2 were later investigated using Mössbauer spectroscopy, revealing spin direction changes across a wide temperature range (Le Caer, Malaman, and Roques, 1978;

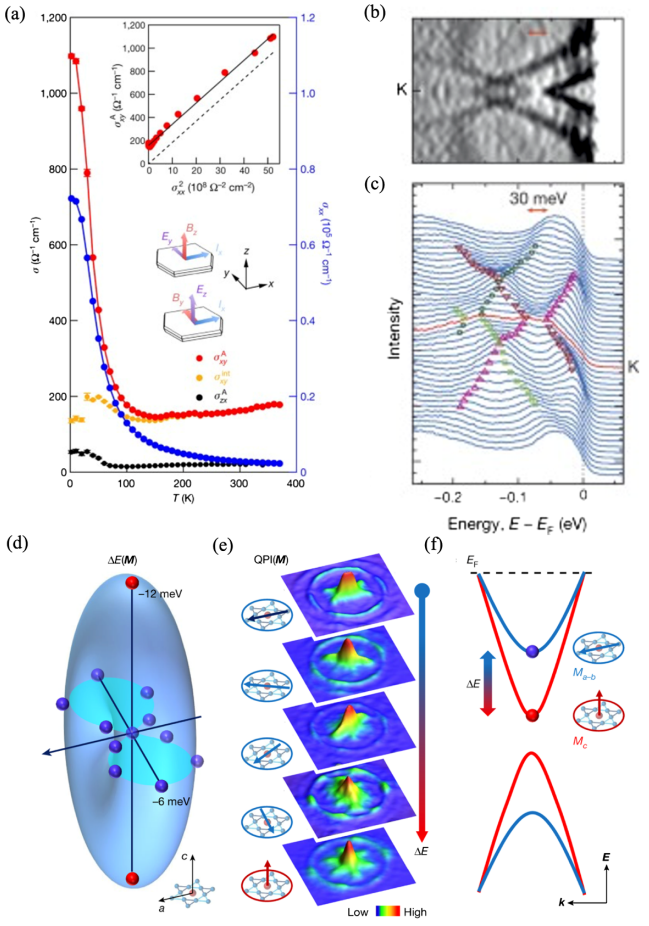

FIG. 17. (a) Anomalous Hall transport in kagome ferromagnet Fe_3Sn_2. (b),(c) Pair of massive Dirac fermions at the K point. (d) Magnetization-dependent energy shift of the Dirac fermions. (e) Quasiparticle interference pattern as a function of magnetization direction. (f) Magnetization-controlled mass gap at the Dirac point. Adapted from Ye *et al.*, 2018, and Yin *et al.*, 2018.

Le Caer *et al.*, 1979). Subsequent explorations of the noncollinear static spin structures and reentrant spin glass behavior were crucial for understanding the role of spin chirality in the AHE (Fenner, Dee, and Wills, 2009). This giant AHE was later attributed to the material's unique frustrated kagome-bilayer structure, while an unconventional scaling law in Hall resistivity was also discovered, pointing to intrinsic mechanisms over extrinsic phenomena (Kida *et al.*, 2011).

Exploration of the electronic structure generated the discovery of massive Dirac fermions near the Fermi level using ARPES [Figs. 17(a)–17(c)] and STM [Figs. 17(d)–17(f)] (Ye *et al.*, 2018; Yin *et al.*, 2018). These studies highlighted the rich electronic structure of Fe_3Sn_2 and its potential for topological phenomena. A subsequent STM study provided spectroscopic evidence of the presence of flat bands and explored their connection to electron correlation and magnetic ordering (Lin *et al.*, 2018). Early theoretical works using DFT calculations predicted Weyl nodes and topological transitions, significantly advancing the theoretical framework surrounding Fe_3Sn_2 (Yao *et al.*, 2018; Biswas *et al.*, 2020). More recent work reported a new type of electron band formation at low temperatures derived from Sn p orbitals and possibly due to electron fractionalization (Ekahana *et al.*, 2024). These studies firmly established the material as a fertile ground for exploring topological quantum states.

Additional research has focused on more exotic magnetic properties of Fe_3Sn_2. Magnetic skyrmions were observed, highlighting potential spintronics applications due to their room-temperature stability and contributions to the topological Hall effect (Hou *et al.*, 2017; P. Wu *et al.*, 2021). Progress in thin-film synthesis has opened further new avenues for exploration.The synthesis of Fe_3Sn_2 thin films was reported using sputter deposition (Khan *et al.*, 2022) and molecular beam epitaxy (Cheng *et al.*, 2022; Ren *et al.*, 2022). This development has enabled further investigation of magnetotransport properties and device integration, paving the way for practical applications in nanostructured devices. The interplay between the topological effects and the AHEs was investigated in epitaxial films and revealed a rich interplay between electronic topology and magnetic ordering (Du *et al.*, 2022; Zhang, Hou, and Mi, 2022). Research, exemplified by Li, Ding *et al.* (2023) and Zhu *et al.* (2024), continues to explore and harness the unique properties of Fe_3Sn_2, thereby driving advancements in spintronics and quantum materials.

b. FeSn compounds

The kagome metal FeSn, with its unique lattice structure, exhibits an interesting interplay of electronic and magnetic phenomena. Bulk single crystals can be grown via crucible-based Sn-flux methods (Häggström *et al.*, 1975). Early investigations focused primarily on FeSn's magnetic behavior where neutron diffraction studies revealed antiferromagnetic ordering below 365 K (Yamaguchi and Watanabe, 1967). Concurrently, Mössbauer spectroscopy provided insights into hyperfine interactions and magnetic configurations (Yamamoto, 1966; Ligenza, 1971, 1972; Kulshreshtha and Raj, 1981). These foundational works established FeSn as a compelling kagome antiferromagnet.

Characterization of FeSn's electronic and band structure properties was performed by measuring its magnetic, electronic and thermal transport, and thermodynamic properties (Sales *et al.*, 2019; Kang *et al.*, 2020b). DFT calculations were used to unveil a three-dimensional electronic structure with Dirac nodal lines, highlighting the potential for topological phases intertwined with magnetic order (Sales *et al.*, 2019). ARPES experiments provide evidence for the presence of Dirac fermions in FeSn [Figs. 18(a)–17(b)], solidifying its status as a platform for studying topological phenomena (Kang *et al.*, 2020b). Additional studies further elucidated the properties of these Dirac states, demonstrating their bulk nature and connection to two-dimensional surface Weyl fermions (Lin *et al.*, 2020).

There is renewed interest in the magnetic properties and spin dynamics of FeSn. *Ab initio* studies employed linear spin wave theory and density functional perturbation theory to analyze spin fluctuations, revealing Landau damping effects on magnons (Y.-F. Zhang *et al.*, 2022). Further neutron scattering work demonstrated the potential for manipulating magnetic states in FeSn to unlock exotic excitations like Dirac magnons (Do *et al.*, 2022).

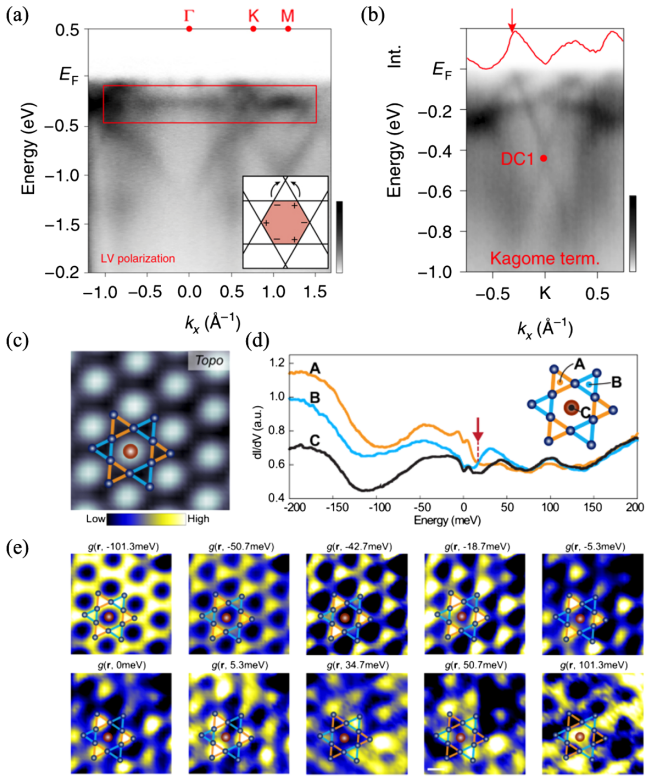

FIG. 18. (a) Flat band and (b) Dirac fermions in FeSn. (c) Topographic STM image of the kagome termination of FeSn. (d) Tunneling conductance spectra from three representative sites A, B, and C. (e) Energy-dependent differential conductance maps. Adapted from Kang *et al.*, 2020b, and Huimin Zhang *et al.*, 2023.

Investigations into the transport properties of FeSn have yielded intriguing results. Contrary to expectations for quasi-2D systems, the material exhibits significant anisotropic conductivity. This anisotropy, observed in early studies on bulk (Sales *et al.*, 2019) and epitaxial thin-film samples (Inoue *et al.*, 2019), challenges conventional interpretations of Hall effects linked to Berry curvature. An additional study quantified higher-order nonlinear AHEs, connecting their response to the quantum geometry of this system (Sankar *et al.*, 2024). Further optical spectroscopy work emphasized the role of Sn layers in contributing to the optical anisotropy of FeSn, challenging simple 2D models (Ebad-Allah *et al.*, 2024). This study, along with investigations of magnetoelastic couplings and lattice constants (Tao *et al.*, 2023), underscores the intricate interplay of correlation effects in FeSn.

STM experiments have explored FeSn in both single crystal (Li, Zhao, Yin *et al.*, 2022; Multer *et al.*, 2023) and thin-film forms (Li, Zhao, Yin *et al.*, 2022; Huimin Zhang *et al.*, 2023; Pham *et al.*, 2024); see Figs. 18(c)–18(e). Spin-polarized STM imaging visualized layered antiferromagnetic ordering at the surface of FeSn (Li, Zhao, Yin *et al.*, 2022). An external magnetic field was found to further modify electronic properties of individual defects (Li, Zhao, Yin *et al.*, 2022) and tune local directionality of the electronic structure (Multer *et al.*, 2023; Huimin Zhang *et al.*, 2023). Spectroscopic signatures of electronic bands were detected as peaks in STM differential conductance dI/dV spectra (Multer *et al.*, 2023; Huimin Zhang *et al.*, 2023).

c. FeGe compounds

FeGe is a kagome lattice metal exhibiting *A*-type AFM (Watanabe and Kunitomi, 1966), and single crystals can be grown via halogen vapor transport methods (Richardson, 1967; Forsyth, Wilkinson, and Gardner, 1978). It has become a key system for investigating the interplay of CDWs, electronic correlations, and magnetism within kagome topological systems. Its unique features, such as Dirac cones, VHSs, and flat electronic bands, create a complex landscape of quantum phases influenced by lattice geometry, spin-phonon coupling, and nontrivial band topology. FeGe therefore stands out as an important platform for studying strongly correlated topological systems.

Specifically, FeGe is host to a diverse array of phenomena including high-temperature magnetic order, unconventional CDW states, and strong electronic correlations, an interplay that is not readily found in most other kagome materials (Setty *et al.*, 2022; Teng *et al.*, 2022,2023; Yin *et al.*, 2022; Yi *et al.*, 2025). The interest in FeGe stems from its distinct *A*-type antiferromagnetic order ($T_N \approx 410$ K), coupled with an unconventional CDW phase ($T_{\mathrm{CDW}} \approx 100$–$110$ K), spin-canting transitions, and topological electronic behavior dominated by VHSs (Teng *et al.*, 2022; Wang, 2023; Zhao *et al.*, 2025); see Figs. 19(a)–19(f).

FeGe possesses electronic bands that are characteristic of the kagome lattice, namely, Dirac cones, flat bands, and VHSs (Setty *et al.*, 2022; Teng *et al.*, 2023); see Figs. 19(g)–19(i). These features are prominent near the Fermi level, where electronic correlation effects amplify their topological and transport signatures. ARPES has revealed key intricacies of the band structure of FeGe, notably spin-split VHSs below T_N, arising from magnetic exchange interactions (Teng *et al.*, 2022, 2023). DFT + DMFT emphasizes the importance of SOC and Hund's coupling in modulating these topological features (Setty *et al.*, 2022; Wang, 2023). The coexistence of flat bands and Dirac cones in FeGe enables Berry curvature effects, driving topological phenomena like the AHE (Yin *et al.*, 2022; Miao *et al.*, 2023). Spectral weight redistribution due to spin and charge ordering underscores the vital role of these kagome-derived features in shaping the electronic properties of FeGe.

The Fermi level's proximity to the VHS makes FeGe highly sensitive to external conditions like pressure, strain, and doping (Wen *et al.*, 2024). Studies under high pressure show that T_{CDW} increases rather than decreases, in contrast to conventional CDW materials, suggesting a unique correlation-driven origin for CDWs in FeGe (Korshunov *et al.*, 2024; Wen *et al.*, 2024). Annealing and doping studies (such as $FeGe_{1-x}Sb_x$) have demonstrated that modifications to lattice symmetry and bonding distances significantly influence band topology and CDW stability (J. Huang *et al.*, 2023; Klemm *et al.*, 2025).

CDWs in FeGe have unconventional origins driven by electronic correlations and accompanied by structural modulation involving Ge dimerization (Wang, 2023; Shi *et al.*, 2024; Zhao *et al.*, 2025). Unlike conventional CDWs

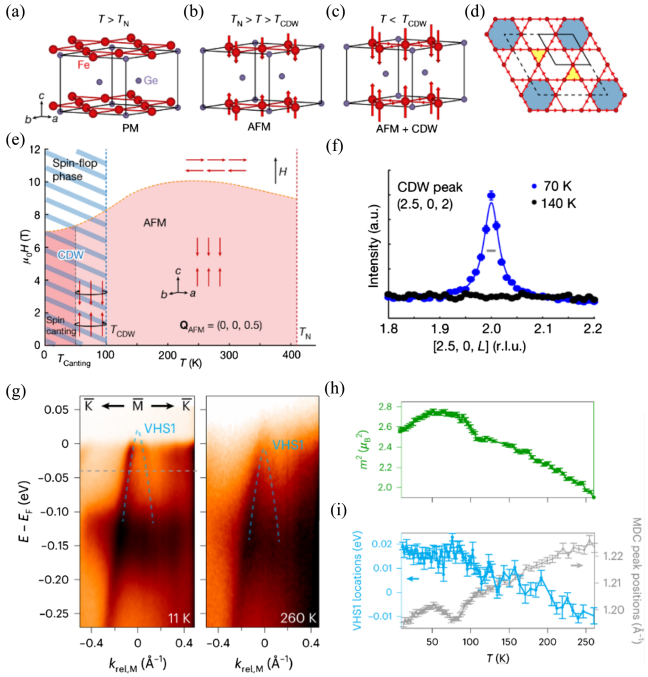

FIG. 19. (a–c) Symmetry-breaking sequence in FeGe. (d) Schematic of the in-plane flux phase. (e) Temperature-field phase diagram of FeGe. (f) Momentum scan across the CDW peak and temperature dependence of the magnetic Bragg peak. (g) Temperature-dependent VHSs from ARPES data. (h) Ordered magnetic moment measured by neutron scattering. (i) Temperature dependence of the VHS binding energy. Adapted from Teng *et al.*, 2022, 2023.

triggered by Fermi-surface nesting, FeGe CDWs emerge from mechanisms like spin-phonon coupling and localized distortions in its kagome lattice geometry (Shao *et al.*, 2023; Wang, 2023).

The antiferromagnetic ground state of FeGe is intricately linked to its CDW behavior. Below T_{CDW}, Ge dimerization acts as an order parameter, enhancing ferromagnetic alignment within the kagome planes and indirectly influencing electronic transport phenomena like the AHE (Yin *et al.*, 2022; Miao *et al.*, 2023; Wang, 2023; B. Zhang *et al.*, 2023). Theoretical models suggest that spin-phonon coupling mechanisms amplify CDW instability through magnetically enhanced spectral weight redistribution near VHSs (Miao *et al.*, 2023; Wang, 2023).

Tuning CDW properties through external parameters such as pressure, annealing, and disorder has emerged as a powerful route to explore emergent CDW phases in FeGe. High-pressure experiments reveal the stabilization of quasi-long-range CDW order with superlattice shifts from $2 \times 2 \times 2$ to $\sqrt{3} \times \sqrt{3} \times 6$ (Korshunov *et al.*, 2024; Wen *et al.*, 2024), while annealing-induced Ge-site disorder disrupts long-range CDWs but enables flexible control of magnetic coupling (Shi *et al.*, 2024; X. Wu *et al.*, 2024; Tan and Yan, 2025). Diffraction studies further point to dimerization-driven bond-orientation order as a precursor to CDW formation (Subires *et al.*, 2025). More broadly, defect engineering through Ge-site vacancy disorder or Sb doping modulates resistivity and suppresses magnetic ordering, offering a handle to tune correlation effects in FeGe kagome lattices (J. Huang *et al.*, 2023; Klemm *et al.*, 2025; Tan and Yan, 2025).

Below ≈60 K spin canting induces transitions to a double-cone magnetic structure accompanied by complex spin excitations (Teng *et al.*, 2022, 2023; Lebing Chen *et al.*, 2024). The nature of this transition is, however, under debate, with recent inelastic neutron scattering measurements suggesting that the incommensurate magnetic structure below ≈60 K could arise from Fermi-surface nesting and takes the form of an itinerant SDW (Lebing Chen *et al.*, 2024; Klemm *et al.*, 2025; Oh *et al.*, 2025). Regardless of the origin, the antiferromagnetic phase introduces magnetic exchange splittings, thus directly influencing the band structure and enabling temperature-dependent modulation of electronic properties (Miao *et al.*, 2023; Teng *et al.*, 2023). Magnetic interactions further stabilize CDWs, with spectral signatures evident in spin-polarized ARPES and scattering studies (Wang, 2023; Z. Chen *et al.*, 2024). Magnetic anisotropies studied via neutron scattering reveal strong interactions between itinerant and localized magnetic moments (Lebing Chen *et al.*, 2024).

Electronic transport in FeGe is highly sensitive to the interplay of CDWs, magnetism, and electronic correlations. Quantum oscillations detected via the de Haas–van Alphen effect reveal reconstructed Fermi surfaces in the CDW phase, suggesting new transport channels mediated by the kagome lattice symmetry (Tang *et al.*, 2024). Anomalous Hall conductivities are frequently reported below T_N and arise from enhanced Berry curvature near the Dirac points and flat bands (Yin *et al.*, 2022; Zhao *et al.*, 2025).

FeGe is a rare example where symmetry-ascending structural transitions are reported at temperatures below the onset of CDWs (S. Wu *et al.*, 2024). This unusual tendency can manifest itself as long as an extremely weak structural instability coexists and competes with the CDW and magnetic orders, rendering FeGe a highly relevant platform for the study of intertwined orders. Its distinct interplay of magnetism, electronic correlations, and topological excitations sets FeGe apart as a paradigmatic material for studying multi-degrees-of-freedom coupling in kagome systems (Setty *et al.*, 2022; Teng *et al.*, 2022), and outstanding questions include determining the precise origin of CDW states under extreme conditions (pressure and doping) and the role of Hund's coupling in driving non-Fermi-liquid behavior. Recent functional renormalization group analyses also hinted at potential SC in FeGe under engineered conditions, opening an avenue for exploring quantum criticality in kagome magnets (Bonetti *et al.*, 2024).

d. Fe_3Sn *compounds*

Here we discuss the relatively less explored binary Fe_3Sn compound, which, despite its collinear magnetic order, also exhibits a large anomalous Nernst effect (ANE) (T. Chen *et al.*, 2022). This phenomenon parallels the ANE seen in the noncollinear antiferromagnet Mn_3Sn (discussed in Sec. IV.A.3). The large ANE in Fe_3Sn is attributed to a nodal plane that creates a flat, hexagonal-shaped electronic band structure with enhanced Berry curvature near the Fermi energy, as clarified via theoretical analysis. The observed ANE reaches up to 3 $\mu V\,K^{-1}$ above room temperature,

making this material a candidate for developing flexible film thermopiles and heat current sensors. A numerical study of the properties of these 3∶1 kagome compounds underscores the potential for high-throughput screening methods to explore a broader range of complex magnetic materials, including both collinear and noncollinear systems (Bouaziz, Nomoto, and Arita, 2025).

2. Co-based compounds: CoSn

CoSn is a key material for studying flat-band physics, Dirac fermions, symmetry breaking, and unique transport properties (Kang *et al.*, 2020a; Liu *et al.*, 2020). Its nonmagnetic kagome lattice and simple Fermi surface make it ideal for understanding intrinsic electronic band properties of the 2D kagome lattice without the complexities of lattice stacking or spin physics. Bulk crystals can be grown via crucible-based Sn-flux methods (Larsson *et al.*, 1996), and CoSn crystallizes in a hexagonal structure (space group $P6/mmm$), with cobalt atoms forming kagome layers interspersed with tin layers. Its electronic structure displays key kagome physics features: flat bands near the Fermi level (confirmed by ARPES) (Kang *et al.*, 2020a; Liu *et al.*, 2020) [see Figs. 20(a) and 20(b)], Dirac dispersions at BZ corners with SOC-induced gaps leading to massive Dirac fermions (Kang *et al.*, 2020a; Liu *et al.*, 2020), and orbital-selective features (d_{xy} and d_{z2} hybridization) revealed by DFT and TB models (Liu *et al.*, 2020; Wan, Lu, and Huang, 2022). The flat bands in CoSn arise from different orbital manifolds and could be directly linked to the compact localized states predicted in 2D kagome toy models (Kang *et al.*, 2020a); see Fig. 20(c).

These flat bands are highly tunable. Strain or doping with Fe, In, or Ni shifts their position relative to the Fermi level. Fe and In doping bring flat bands closer to the Fermi energy, promoting magnetic responses and instabilities, while Ni doping suppresses these effects (Sales *et al.*, 2021, 2022; Cheng *et al.*, 2023). Theoretical models suggest strain could induce transitions to topologically nontrivial states with Weyl fermions or enhanced correlation phenomena (Kang *et al.*, 2020a; Cheng *et al.*, 2023; Mojarro and Ulloa, 2024).

Recent studies show rotational symmetry breaking (*nematicity*) in CoSn at 225 K driven by flat-band thermal excitations (Drucker *et al.*, 2024). This is unique, as it occurs without magnetic order, suggesting that the flat bands in CoSn cause electronic instabilities leading to nematic transitions. While intrinsic CoSn is nonmagnetic, doping introduces localized magnetic states and creates a rich magnetic phase diagram (Meier *et al.*, 2019); see Fig. 20(d). Fe doping induces a spin glass state and ferromagnetic fluctuations linked to flat bands near the Fermi level (Sales *et al.*, 2021, 2022; Vijay *et al.*, 2023). For instance, $Co_{1-x}Fe_xSn$ displays tunable magnetoresistance due to band realignment and localized flat states (Vijay *et al.*, 2023). Theoretical work has proposed CoSn as a platform for interaction-driven quantum order, including CDWs (potentially induced by correlations near VHSs and flat bands under strain or pressure) (Mojarro and Ulloa, 2024) and unconventional SC (suggested by weak correlation effects and kagome physics) (Liu *et al.*, 2020).

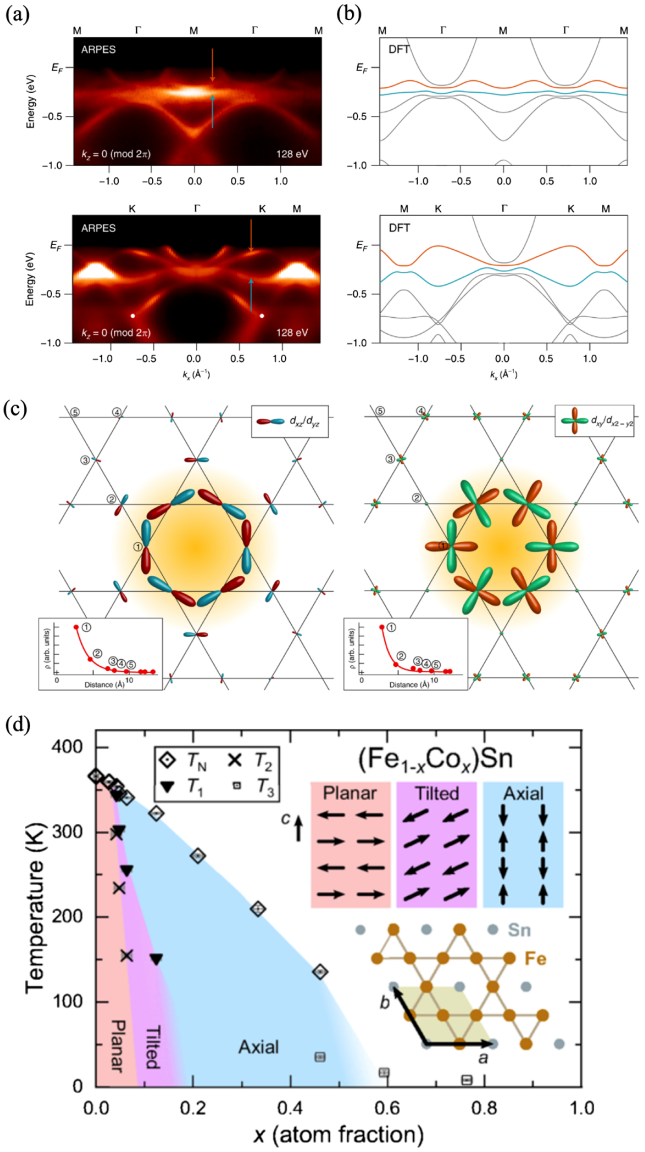

FIG. 20. (a),(b) ARPES data (left panels) and DFT calculations (right) of the electronic bands in CoSn, showing evidence for the presence of a double flat band. (c) Real-space wave functions underlying the flat bands derived from out-of-plane (left panel) and in-plane (right panel) orbitals. (d) Magnetic phase diagram of the mixed-composition kagome compound $(Fe_{1-x}Co_x)Sn$. Adapted from Meier *et al.*, 2019, and Kang *et al.*, 2020a.

CoSn also exhibits significant transport anisotropy, with in-plane resistivity much higher than that of the out-of-plane due to flat-band localization and large effective masses (J. Zhang *et al.*, 2021; Huang *et al.*, 2022). These differences are tied to kagome geometry, particularly flat-band dispersion and scattering near VHSs. Despite being nonmagnetic, CoSn shows flat-band-driven negative magnetoresistance in external fields that is attributed to enhanced scattering and ferromagnetic correlations (J. Zhang *et al.*, 2021). Temperature-dependent transport and spectroscopy studies further reveal strong phonon-electron interactions near flat bands that affect quasiparticle velocities, scattering rates, and resistivity (Yin *et al.*, 2020a; Huang *et al.*, 2022).

STM has visualized the localized real-space kagome flat-band states in CoSn (C. Chen *et al.*, 2023), serving as a fingerprint of ideal kagome physics and a path to exploring strongly correlated phases. While CoSn is topologically trivial, small SOC gaps suggest the proximity to a topological phase. Strain or doping could potentially realize Weyl or Dirac semimetal phases, as suggested theoretically (Kang *et al.*, 2020a; Sales *et al.*, 2021; Cheng *et al.*, 2023).

The development of thin films of CoSn offers added control over its properties, where, for instance, ARPES studies reveal enhanced SOC effects and sharper flat bands than in bulk samples (Cheng *et al.*, 2023). In addition, strain engineering can shift energy levels, modulate Fermi-surface topology, and explore emergent phases (Cheng *et al.*, 2023; Mojarro and Ulloa, 2024).

Compared to magnetic kagome metals like FeSn, CoSn lacks intrinsic magnetism, which simplifies its electronic structure (Kang *et al.*, 2020a; Liu *et al.*, 2020). Unlike superconducting AV_3Sb_5 materials, CoSn displays weaker correlations and no ambient CDWs or superconducting phases (Mojarro and Ulloa, 2024). Its simplicity makes CoSn a benchmark for kagome physics, highlighting the interplay among flat bands, orbital differentiation, and Dirac features.

Despite substantial progress, the following questions remain: How can CoSn be tuned into a robust topological regime? What mechanisms underlie the reported nematic order, and how is it connected to flat-band physics? Addressing these requires systematic doping experiments, thin-film engineering, and advanced spectroscopies. Further research on tunability and correlated phases holds the potential to unlock more exotic properties of this kagome system.

3. Mn-based compounds: Mn_3Sn and Mn_3Ge

The Mn-based family of binary kagome compounds supports unusual magnetically ordered states. Both Mn_3Sn and Mn_3Ge crystallize in the Ni_3Sn-type structure with hexagonal space group $P6_3/mmc$ [see Fig. 21(a)], and crystals can be grown via Bridgman techniques (Krén *et al.*, 1975; Tomiyoshi, 1982). It is known that these structures are stabilized by excess Mn, which randomly occupies the Sn or Ge sites (Krén *et al.*, 1975; Yamada *et al.*, 1988). Both systems realize an exotic antiferromagnetic state that exhibits an antichiral spin texture (Nagamiya, Tomiyoshi, and Yamaguchi, 1982; Tomiyoshi, 1982); see Fig. 21(b). For Mn_3Sn this state occurs at $T_N \approx 430$ K, while for Mn_3Ge it is at $T_N \approx 380$ K. The latter retains this magnetic structure to the lowest temperatures, whereas the former has a transition to a noncoplanar magnetic phase below approximately 50 K (Nakatsuji, Kiyohara, and Higo, 2015; Kiyohara, Tomita, and Nakatsuji, 2016; Nayak *et al.*, 2016). The Mn atoms host a total moment of approximately $3\mu_B$; however, a small tilting of the in-plane moments results in a net ferromagnetic moment of order $0.001\mu_B$.

A striking property of these systems is a large anomalous Hall response observed for magnetic fields in the kagome plane [see Fig. 21(c)], despite the system having only a weak ferromagnetic component in its magnetic order (Nakatsuji, Kiyohara, and Higo, 2015; Kiyohara, Tomita, and Nakatsuji, 2016; Nayak *et al.*, 2016). This is captured by calculations of Berry curvature contributions to the anomalous Hall response (Kübler and Felser, 2014). The presence of Weyl nodes in these materials has been investigated theoretically (Yang *et al.*, 2017) and experimentally (Kuroda *et al.*, 2017).

Several extensions have followed the aforementioned discoveries, including the observation of large responses in other anomalous transport responses, such as large Nernst (Ikhlas *et al.*, 2017) and thermal Hall effects (Li *et al.*, 2017). Given its large anomalous Hall response but weak stray and demagnetizing field owing to its largely antiferromagnetic nature (as well as T_N above room temperature), these systems have attracted significant attention for their possible utility in spintronics. Some of these properties can be rationalized from their connection to antiferromagentic Weyl systems (Liu and Balents, 2017).

These compounds have been studied in a number of spintronic device geometries, and an early study confirmed

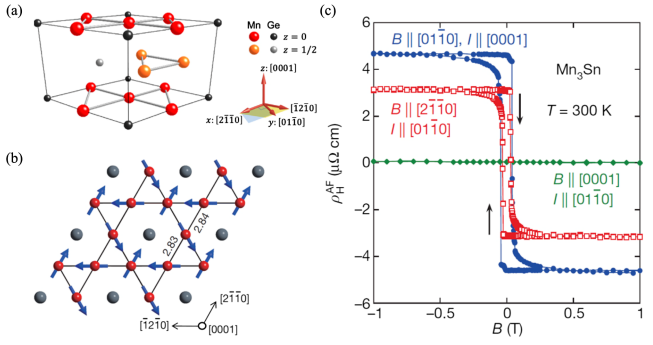

FIG. 21. (a) Crystal structure of Mn_3Ge, which is isostructural to Mn_3Sn. From Kiyohara, Tomita, and Nakatsuji, 2016. (b) Magnetic ordering in the kagome plane for Mn_3Sn. (c) Anomalous Hall response. From Nakatsuji, Kiyohara, and Higo, 2015.

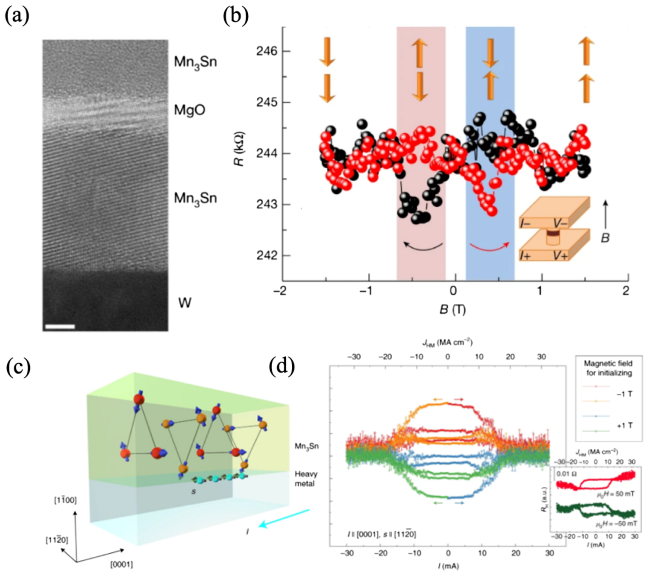

FIG. 22. (a) TMR device geometry and (b) response for Mn_3Sn. (a),(b) From Xianzhe Chen *et al.*, 2023. (c) Kagome/heavy metal heterostructure and (d) spin-orbit torque switching for Mn_3Sn, with the initializing field shown in the upper inset and bipolar switching shown in the lower inset. (c),(d) From Takeuchi *et al.*, 2021.

the presence of spin Hall effects using NiFe electrodes (Kimata *et al.*, 2019). More recently, tunneling magnetoresistance (TMR) device structures using MgO barriers [see Fig. 22(a)] demonstrated a tunneling resistance response at room temperature [see Fig. 22(b)] (Xianzhe Chen *et al.*, 2023). In addition, spin-orbit torques have been demonstrated using conventional heterostructures of Mn_3Sn and heavy element metals (Takeuchi *et al.*, 2021; Higo *et al.*, 2022); see Figs. 22(c) and 22(d). This was extended in recent work on $Si/SiO_2/Mn_3Sn/AlO_x$ structures using all-electrical inputs (Deng, Liu *et al.*, 2023). The development of thin films of these materials has played a crucial role in these efforts (Higo and Nakatsuji, 2022), and further development of spintronic devices based on these and related materials is a primary area of research.

4. Ni-based compounds: Ni_3In

The binary Ni-based kagome metal Ni_3In has been shown to support correlated electronic states. The system crystallizes in the Ni_3Sn-type structure with hexagonal space group $P6_3/mmc$ [see Fig. 23(a)] (Baranova and Pinsker, 1966), and crystals can be grown via a halogen catalyzed reaction and chemical vapor transport (Ye *et al.*, 2024). Recent studies of bulk single crystals (Gim *et al.*, 2023; Ye *et al.*, 2024), thin films (Han *et al.*, 2024), and polycrystalline materials (Garmroudi *et al.*, 2024) have been reported. Of central interest in this system is the expectation from DFT that (before interactions are considered) a partially flat band associated with the Ni ions appears at the Fermi level; see Fig. 23(b).

This electronic configuration appears to give rise to correlated electron phenomena reminiscent of heavy electron systems, including f-electron Kondo systems (Checkelsky *et al.*, 2024). Studies of Raman scattering exhibit a low-temperature renormalization of frequency and line shape that recalls that of the onset of Kondo screening (Gim *et al.*, 2023); see Fig. 23(c). Electrical transport reveals a T-linear behavior below 100 K and points to a strongly correlated Fermi liquid below 2 K (Han *et al.*, 2024; Ye *et al.*, 2024); see Fig. 23(d). By applying a magnetic field and pressure, this can be changed to a more conventional transport response (Ye *et al.*, 2024). Moreover, conventional metalicity is observed for the isostructural system Ni_3Sn, where the Fermi level is shifted away from the bands with quenched kinetic energy, suggesting the role of the flat band in generating strong electronic correlations. The consequences of correlation effects for band topology in these systems is a subject of ongoing study.

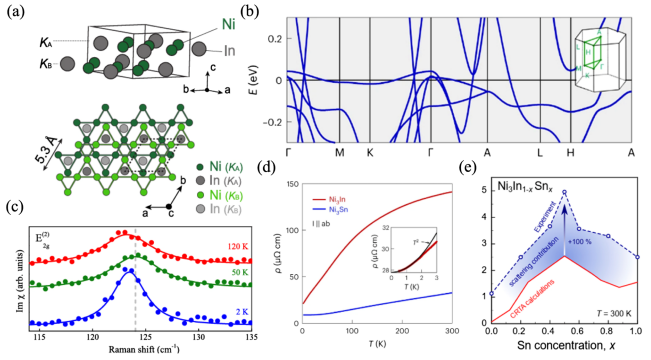

FIG. 23. (a) Crystal structure of Ni_3In. From Han *et al.*, 2024. (b) DFT electronic structure of Ni_3In. From Ye *et al.*, 2024. (c) Temperature dependence of Raman response as a function of temperature in single crystals of Ni_3In. From Gim *et al.*, 2023. (d) Electrical transport of Ni_3In and Ni_3Sn bulk single crystals. From Ye *et al.*, 2024. (e) Concentration dependence of the calculated and observed power factors in polycrystalline $Ni_3(In, Sn)$ alloys. From Garmroudi *et al.*, 2024.

These band features have been identified as a possible source of a large power factor (PF) with potential relevance for metallic thermoelectrics (Garmroudi *et al.*, 2023). As shown in Fig. 23(e), studies of alloys of Ni_3In and Ni_3Sn reveal a maximum in PF that is consistent with the role of asymmetric scattering across the Fermi level between the flat-band states and the highly dispersive bands (Garmroudi *et al.*, 2024). The design of such metallic thermoelectrics in kagome and other flat-band metals [for example, pyrochlore metals (Wakefield *et al.*, 2023)] is an emerging field of study.

5. Nb-based compounds: Nb_3X_8

The Nb_3X_8 family (X = Cl, Br, or I) comprises layered 2D materials, with each unit consisting of two Nb_3X_8 monolayers stacked along the c axis through weak van der Waals interactions. Crystals can be produced via high-temperature sintering (Miller, 1995) or halide liquid flux techniques (Haraguchi *et al.*, 2017), and within each monolayer, a breathing kagome lattice of Nb_3 trimers forms where the intracluster Nb-Nb distance is significantly shorter than the intercluster distance. Strong metal-metal bonding within each trimer results in a localized spin $S = 1/2$ that primarily occupies the Nb $^2a_1$ orbital (Pasco *et al.*, 2019; S. Gao *et al.*, 2023; Wang, Wu *et al.*, 2023). DFT calculations predict a metallic state; however, transport and ARPES measurements consistently indicate that Nb_3X_8 is an insulator (Yoon *et al.*, 2020; Sun *et al.*, 2022; S. Gao *et al.*, 2023). This discrepancy can be attributed to strong electron correlations, suggesting that Nb_3Cl_8 and Nb_3Br_8 are Mott insulators rather than conventional band insulators, with the Fermi level within the Mott gap (S. Gao *et al.*, 2023; Y. Zhang *et al.*, 2023; Grytsiuk *et al.*, 2024; Aretz *et al.*, 2025).

Magnetic susceptibility measurements reveal a first-order phase transition in both Nb_3Cl_8 and Nb_3Br_8 progressing from high-temperature paramagnetic (α phase) to low-temperature nonmagnetic (β phase), accompanied by a structural transition. The transition temperature is ≈90 K for Nb_3Cl_8 and ≈380 K for Nb_3Br_8 (Pasco *et al.*, 2019). At high temperatures, both adopt the $P3\bar{m}1$ space group in the α phase. In the β phase, Nb_3Br_8 has a well-established $R3\bar{m}$ symmetry (Pasco *et al.*, 2019), while recent evidence increasingly supports a similar assignment for Nb_3Cl_8 (Jeff *et al.*, 2023; Kim, Lee *et al.*, 2023). The structural transition is attributed to a mechanical shift of layers that alters the stacking order while retaining the same monolayer structure in both phases.

Weak magnetic interactions between trimer clusters are strongly affected by charge fluctuations within Nb–Nb and Nb–Cl bonds, thus reflecting the interplay between structural and electronic degrees of freedom (Nakamura *et al.*, 2024). The nonmagnetic ground state has been proposed to arise from a spin-singlet configuration with a thermal gap to an excited triplet state rather than charge disproportionation

($[Nb_3]^{7+}$-$[Nb_3]^{9+}$), as the core-level spectra indicate equivalent Nb valence states (S. Gao *et al.*, 2023). In addition, anomalous magnetic susceptibility enhancements of around 1020 K have been observed in specific samples, likely due to defect-induced spins or residual high-temperature phases retained during synthesis (Pasco *et al.*, 2019). These sample-specific effects suggest an extrinsic rather than intrinsic origin. Notably, pressure-induced metallization in Nb_3Cl_8 is coupled with a structural phase transition and pronounced changes in its band structure (Shan *et al.*, 2023).

While flat bands have been identified in several kagome metals, the lack of exfoliatable and semiconducting kagome materials significantly limits their integration into device applications. In a breathing kagome lattice, the absence of inversion symmetry opens a gap in the Dirac cone, resulting in a semiconducting ground state, while flat bands persist owing to the protection of mirror reflection symmetry (Sun *et al.*, 2022). Unlike flat bands in an ideal kagome lattice, those in the trigonally distorted lattice of Nb_3X_8 are highly isolated. Recent ARPES experiments have observed flat bands across various breathing kagome systems, including Nb_3Cl_8, Nb_3Br_8, Nb_3I_8, and Nb_3TeCl_7 (Regmi *et al.*, 2022, 2023; Sun *et al.*, 2022; S. Gao *et al.*, 2023; Hongrun Zhang *et al.*, 2023). These observations align well with theoretical band calculations, confirming that the flat bands originate from the breathing kagome lattice of niobium atoms predominantly involving niobium *d*-orbital character. Furthermore, energy splitting in the lower Hubbard band of bilayer β-Nb_3Cl_8 has been attributed to enhanced interlayer hybridization, resulting in the formation of bonding-antibonding states in the β phase, which further underscores the role of Mott physics in breathing kagome systems (Pasco *et al.*, 2019; Y. Zhang *et al.*, 2023; Grytsiuk *et al.*, 2024).

The magnetic order in the Nb_3X_8 family is predicted to depend on the number of layers in thin-film samples, with unique phenomena emerging as the system approaches the 2D limit (Conte, Ninno, and Cantele, 2020). The van der Waals nature of Nb_3X_8 enables easy exfoliation into monolayers, providing a rare opportunity to explore its magnetic properties, which include monolayer ferromagnetism, all-in antiferromagnetic spin structures, and quantum spin-liquid states (Peng *et al.*, 2020; Wang, Wu *et al.*, 2023). More importantly, the intrinsic breaking of both time-reversal and inversion symmetries positions Nb_3I_8 as a noteworthy 2D anomalous valley Hall material capable of exhibiting spontaneous valley polarization without the need for external tuning (Peng *et al.*, 2020). In ferroelectric bilayer Nb_3I_8 with *A*-type antiferromagnetic coupling, the coupling of electric polarization to spin, valley, and layer degrees of freedom enables the realization of a spin-valley-layer-polarized AHE (Feng, Chen, and Qi, 2023). Furthermore, mechanical exfoliation experiments on Nb_3Cl_8 have successfully yielded few- and single-layer samples with excellent ambient stability and enhanced conductivity (Yoon *et al.*, 2020; Regmi *et al.*, 2023). These exceptional properties, along with the novel low-dimensional magnetic behaviors, establish the Nb_3X_8 family as a versatile platform for exploring fundamental physics and advancing device applications.

B. Ternary structures

The incorporation of a third element into the crystal structures of kagome metals affords an additional degree of tunability and chemical diversity not achievable in simpler binary compounds. Layered kagome planes can be better isolated via layers of interleaving ions, rendering reduced out-of-plane hopping and more two-dimensional electronic properties, and additional modes of symmetry breaking can be interfaced with the kagome network. Key examples are illustrated in Fig. 24. For instance, magnetic layers can be brought into proximity with kagome planes or alternate units that undergo bond or charge order coupled to the kagome network, all within the same structural unit. There is a broad phase space of ternary structure types that host kagome networks and allow for this tunability, much of it unexplored. In this section we highlight some of the most commonly studied variants to date.

1. $M_3A_2X_2$ compounds

The $M_3A_2X_2$ or shandite crystal structure consists of kagome planes of *M*-site transition-metal ions coordinated with main group *A*-site ions and *X*-site chalcogens; see Fig. 25(a). Bulk crystals can be grown typically via

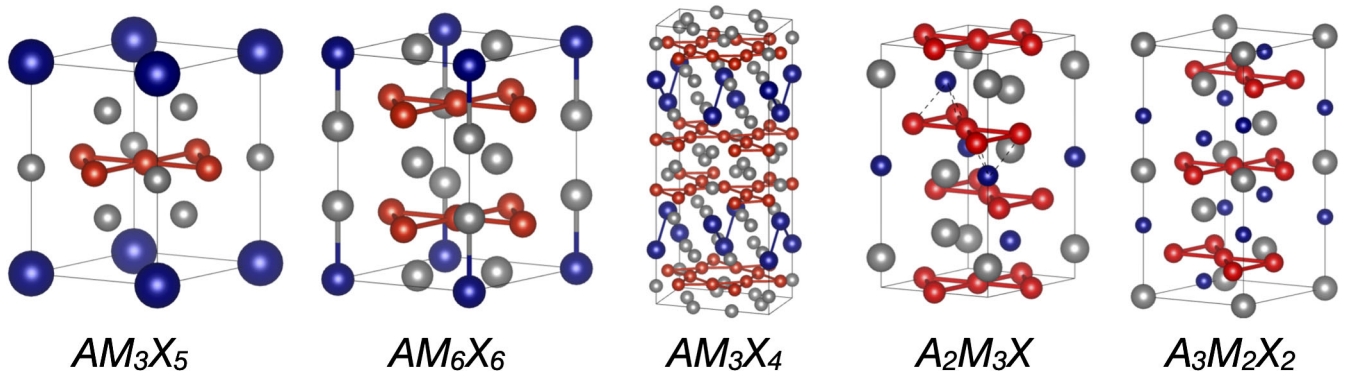

FIG. 24. Crystal structures of common ternary families possessing isolated kagome networks. Kagome networks and the constituent atoms are shown as red spheres connected with red bonds. The out-of-plane bonds highlighted in the bilayer AM_6X_6 structure illustrate the atoms driving the chain instability underlying the CDW-like state in select variants. Blue spheres and bonds shown in the AM_3X_4 structure illustrate the zigzag network of interleaving A-site ions. The dashed lines in the ternary *C*15 Laves AM_3X structure show the native pyrochlore network broken up by the ordered incorporation of *X*-site ions.

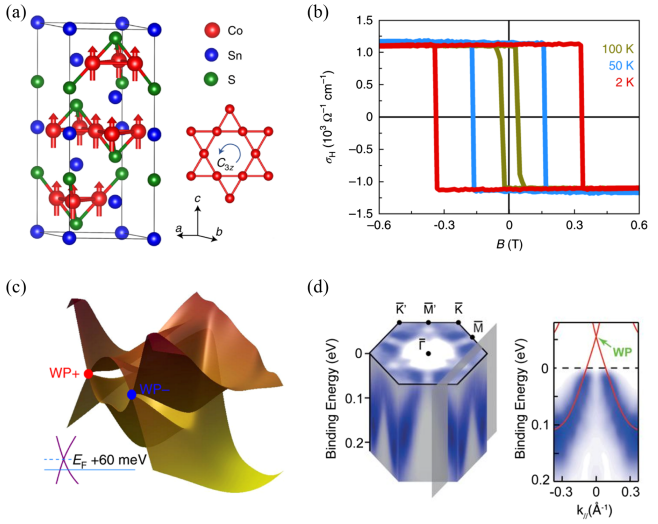

FIG. 25. (a) Crystal structure of layered kagome metal $Co_3Sn_2S_2$. (b) Giant anomalous Hall conductivity. (c) Low-energy electronic structure featuring a pair of Weyl points. (d) Fermi-surface and low-energy bands showing a Weyl point right above E_F. Adapted from Liu *et al.*, 2018, 2019.

Bridgman techniques (Holder *et al.*, 2009) or sintering techniques with mineralizers (Li *et al.*, 2019). The kagome layers are stacked in an ABC sequence and the triangles of the kagome network alternately have one *X*-site ion above and below them. There are two unique *A*-site positions in the cell and one rests within the kagome planes. The most widely studied material in this class in terms of its electronic properties is the half metal ferromagnet $Co_3Sn_2S_2$. Initial work (Vaqueiro and Sobany, 2009) reported ferromagnetic order at a Curie temperature $T_C \approx 180$ K and metallic behavior, with magnetic moments localized within the Co kagome lattice.

Work exploring the electronic structure of $Co_3Sn_2S_2$ identified the compound as an intrinsic magnetic Weyl semimetal. Liu *et al.* observed a giant AHE [Fig. 25(b)] attributed to Berry curvature concentrated around Weyl points near the Fermi energy [Fig. 25(c)]. DFT calculations predicted six Weyl points within 60 meV of the Fermi level, and experiments confirmed a large anomalous Hall conductivity (σ_{xy} up to 1100 Ω^{-1} cm^{-1}) (Liu *et al.*, 2018), with a modulation of the anomalous Hall angle up to a magnitude of 25° (J. Yang *et al.*, 2025). Wang *et al.* (2018) further confirmed the presence of intrinsic ferromagnetism (moment $\approx 0.3\mu_B$ per Co atom) and Weyl points near the Fermi energy using ARPES and DFT. Wang *et al.* provided direct evidence of band crossings and highlighted the connection between topology and magnetism as the source of the exceptional transport properties. Moreover, Yang *et al.* (2020) reported a giant ANE with a significant Nernst conductivity up to 10 μV/K at low temperatures, further emphasizing the role of Berry curvature in anomalous transverse thermoelectric responses.

Focusing on the surface, Morali *et al.* (2019) used ARPES and STM to observe diverse surface terminations and confirm the connectivity of bulk Weyl cones via Fermi arcs, while Xu *et al.* (2018) resolved topological surface states linked to Weyl nodes and SOC. The character of the states at the Fermi level, however, varies depending on the surface termination probed, leading to discrepancies in the literature (Mazzola *et al.*, 2023). Liu *et al.* (2019) mapped the bulk band structure and topology in the magnetic Weyl semimetal phase, linking the giant AHE and anomalous Hall angle to Berry curvature contributions from Weyl nodes; see Fig. 25(d).

Yin *et al.* (2019) discovered *negative-flat-band magnetism*, with a negative effective *g* factor driven by the kagome lattice and dominated by SOC effects. This study proposed that SOC lifts degeneracies in flat bands, creating an orbital moment that suppresses ferromagnetism. The magnetoresistance (MR) and the planar Hall effect (PHE) were connected to topological Berry curvature in Weyl nodes linking PHE anomalies to magnetic field rotation (Shama and Singh, 2020). Howlader *et al.* (2021) visualized temperature-dependent domain structures using magnetic force microscopy, in the process demonstrating strong pinning of domain walls below 130 K.

Additional studies focusing on correlations between magnetic phases, doping, and Berry-phase physics brought advances in understanding the magnetic and electronic properties of $Co_3Sn_2S_2$. A neutron diffraction and DFT investigation detailed the magnetic exchange couplings and predicted a Weyl-dominated intermediate temperature regime with 120 antiferromagnetic orders (Q. Zhang *et al.*, 2021). Other neutron and magnetization studies instead identified an intermediate crossover driven by domain wall nucleation (Soh *et al.*, 2022). Yanagi *et al.* (2021) explored hole- and electron-doped variants, revealing that doping induces band parity inversions and enhances anomalous Nernst conductivity. Shen *et al.* (2020) reported extrinsic AHE enhancement via Fe and Ni doping while introducing Berry curvature hot spots (Thakur *et al.*, 2020).

Other researchers have emphasized experimental tunability. Schilberth *et al.* (2024) showed how magnetization reorientation can generate new Weyl nodes or nodal lines by modulating Berry curvature response. Karmakar *et al.* (2022) found that uniaxial strain enhances thermal Hall and Hall conductivity by realigning band topology. Tanaka *et al.* (2020) demonstrated fabrication of $Co_3Sn_2S_2$ thin films using chemical vapor transport synthesis, achieving quantum-limit mobility, and H.-J. Gao *et al.* (2023) synthesized ultrapure crystals with record-setting 10 490 cm^2/(V s) mobility and 2500% MR. Recently, in fact, there have also been observations of chiral phonons (see Sec. II.C) rising from the coupling between the electronic topology and the magnetic order (Che *et al.*, 2025; R. Yang *et al.*, 2025).

Other than $Co_3Sn_2S_2$, a number of related shandite kagome systems have been explored. Substituting In for Sn and Ni for Co provides access to nonmagnetic counterparts such as $Ni_3In_2S_2$ (H. Fang *et al.*, 2023), which was recently shown to host Dirac nodal lines (T. Zhang *et al.*, 2022). Intermediate substitution in $Co_3Sn_{2-x}In_xS_2$ tunes the magnetic order and electronic structure, while $Co_3In_2S_2$ itself shows a field-induced butterflylike anisotropic MR (Weihrich *et al.*, 2004; Pielnhofer *et al.*, 2014; Corps *et al.*, 2015; Lv *et al.*, 2025). Beyond Co- and Ni-based shandites, compounds incorporating Rh or Pd have also been investigated from first-principles methods, although their properties continue to be far less explored (Buiarelli *et al.*, 2025). These materials

enlarge the accessible parameter space of the kagome shandite family, spanning from magnetic Weyl semimetals to nonmagnetic nodal-line systems, and suggest that further investigation of the less studied members may reveal yet unexplored topological and correlated phases.

2. AM_3X_5 compounds

AM_3X_5 compounds crystallize in a layered structure with kagome nets formed via the M-site (M = V, Ti, or Cr) ion that are octahedrally coordinated via the X site (X = Sb or Bi). M_3X_5 blocks are separated by triangular lattice layers of A-site (A = K, Rb, or Cs) ions, forming a chemically and electronically two-dimensional structure. X-site ions occupy two sites in the lattice. The first is in the kagome plane within the voids of the hexagons of the M-site kagome network, and the second is within a honeycomb network above and below the kagome planes. While the interlayer bonding is ionic, the lattice remains highly exfoliable, and layers as thin as two unit cells have been achieved (Song *et al.*, 2023), as has some degree of gate tunability (Zheng *et al.*, 2023).

a. AV_3Sb_5 *compounds*

AV_3Sb_5 (A = K, Rb, or Cs) compounds were reported as a new structure type featuring a V-based kagome sublattice with kagome-derived saddle points close to E_F (Ortiz *et al.*, 2019). Bulk crystals can be grown via crucible-based self-flux techniques (Ortiz *et al.*, 2020), where a high-temperature CDW transition was observed in electrical transport, heat capacity, and magnetic susceptibility followed by a low-temperature transition into a superconducting state (Ortiz *et al.*, 2020; Ortiz, Sarte *et al.*, 2021; Q. Yin *et al.*, 2021),

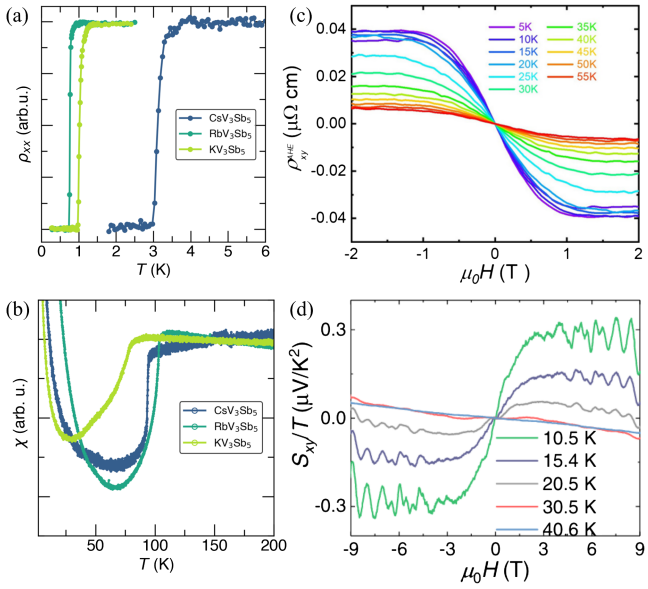

FIG. 26. (a) Resistivity data showing the superconducting transitions for AV_3Sb_5 compounds. (b) Magnetization data showing the CDW transitions for AV_3Sb_5 compounds. (c) Magnetotransport data showing the onset of the AHE below the CDW transition for CsV_3Sb_5. From Yu, Wu *et al.*, 2021. (d) ANE data suggesting the onset of broken TRS below 30 K. From D. Chen *et al.*, 2022.

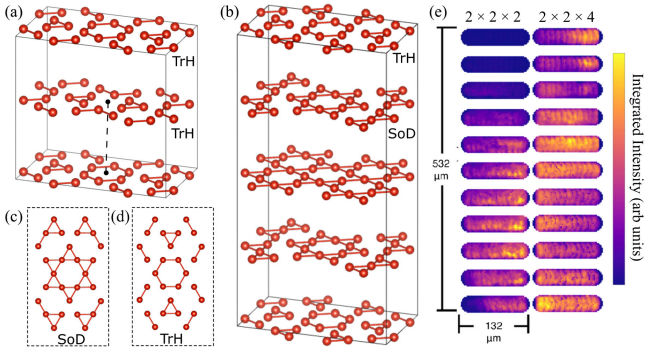

FIG. 27. (a) Staggered trihexagonal structure that comprises the $2 \times 2 \times 2$ reconstructed cells in the CDW states of RbV_3Sb_5 and KV_3Sb_5. (b) Average structure of the $2 \times 2 \times 4$ reconstructed cell in the CDW state of CsV_3Sb_5. (c) The Star-of-David pattern of distortion for a single kagome layer. (d) The trihexagonal pattern of distortion for a single kagome layer. (e) Real-space mapping of the $2 \times 2 \times 2$ and $2 \times 2 \times 4$ cells in a CsV_3Sb_5 crystal, showing phase separation and competition between the two states. Data from Plumb *et al.*, 2024.

as shown in Fig. 26. Between the onsets of the high-temperature CDW transition and the low-temperature SC state, a host of unconventional phenomena have been reported in V-based 135 materials; more extensive, focused reviews were given by K. Jiang *et al.* (2023) and Wilson and Ortiz (2024). In the following sections, we highlight some of the key phenomenology reported to date.

Charge-density-wave state. The CDW order that forms is three dimensional in nature (H. Li *et al.*, 2021; Liang *et al.*, 2021; Ortiz, Teicher *et al.*, 2021; C. Li *et al.*, 2022; Zhu *et al.*, 2023) and forms a staggered trihexagonal (inverse-Star-of-David) pattern of order that is shifted by half a unit cell from layer to layer along the c axis (Tan *et al.*, 2021), as shown in Fig. 27. The distortion and variants of it can be parametrized by three modes along high-symmetry directions in the BZ (Christensen *et al.*, 2021).

The importance of the e-ph interaction in forming the CDW state is suggested by a number of experimental results. High-resolution ARPES on KV_3Sb_5 observed a CDW-induced Fermi-surface reconstruction, associated band folding, and gap opening at the boundary of both pristine and reconstructed BZs, with typical reported signatures of e-ph coupling such as kinks (H. Luo *et al.*, 2022). Broadband optical spectroscopy observed phonon anomalies above and below the CDW transition in KV_3Sb_5, indicating a strong coupling of phonons to the underlying electronic structure (Uykur *et al.*, 2022). Neutron scattering experiments also reveal that the CDW order in CsV_3Sb_5 is linked to a static lattice distortion and a sudden hardening of the B_{3u} longitudinal optical phonon mode at the BZ boundary, further highlighting the significant role of a wave-vector-dependent e-ph coupling (Xie *et al.*, 2022).

One notable exception to the standard $2 \times 2 \times 2$ enlargement of the unit cell is the presence of a coexisting $2 \times 2 \times 4$ CDW order in CsV_3Sb_5 that seemingly also possesses an interleaved Star-of-David character distortion (Stahl *et al.*, 2022; Kautzsch, Ortiz *et al.*, 2023; Xiao *et al.*, 2023; Ning *et al.*, 2024). Regardless of this detail, all three V-based 135 variants show broken rotational symmetry in the CDW state,

as the crystal symmetry is lower from hexagonal to orthorhombic, though this symmetry breaking is largely driven by shifts in the interlayer phasing of breathing modes between kagome planes versus broken rotational symmetry in any one kagome layer, which is seemingly preserved.

As discussed in Sec. III.A, the possibility of flux order on the kagome lattice is a major route of inquiry regarding whether TRS is broken in the CDW state (Fernandes *et al.*, 2025). This can occur because of the presence of p-type VHS at E_F, and theoretical models utilizing this fact have been put forward (Lin and Nandkishore, 2021; Zhou and Wang, 2022; Li, Kim, and Kee, 2024). Electrical and thermal magnetotransport studies identified the onset of an AHE (Yang *et al.*, 2020; Yu, Wu *et al.*, 2021; L. Wang *et al.*, 2023) and an ANE (D. Chen *et al.*, 2022; Zhou *et al.*, 2022) below the CDW transitions of the V-based 135 compounds. There is, however, no spontaneous (zero-field) component to the AHE; instead, at low fields, a strong nonlinear Hall response is observed. The origin of this is under debate. It can potentially arise, for instance, because of TRS-breaking, Berry curvature effects from partial gapping of topological electronic bands (Liang *et al.*, 2018) or from sharp velocity changes along Fermi contours in the CDW-reconstructed band structure (Koshelev *et al.*, 2024).

Further magnetotransport data identified the onset of a chiral transport term at low temperatures (within the CDW state), implying either a field-tunable structural chirality or the presence of a TRS-breaking order parameter (Guo *et al.*, 2022). Coincident with the onset of the CDW, μSR studies report the onset of an unusual source of depolarization that is suggestive of the appearance of a weak magnetic moment (Khasanov *et al.*, 2022; Mielke *et al.*, 2022; Guguchia *et al.*, 2023b). Supporting this suggestion, tuning fork resonator measurements have reported the formation of a magnetic state below 30 K within the CDW state of CsV_3Sb_5 (Gui *et al.*, 2025), and a superconducting diode effect has been observed in the absence of an external magnetic field (Le *et al.*, 2024). Similarly, STM measurements have reported a field-tuned pattern of CDW order (Jiang *et al.*, 2021), which is discussed at greater length later in this section.

Optical measurements have also extensively characterized the CDW transition. Frequency-dependent optical conductivity measurements have quantified the band gap and parametrized the relative role of electronic correlations across the 135 family (Uykur *et al.*, 2021, 2022; Wenzel *et al.*, 2022), and coherent phonon and Raman spectroscopy identified the evolution of lattice modes through the CDW transition (Ratcliff *et al.*, 2021; Z. X. Wang *et al.*, 2021; Wu *et al.*, 2022; Wulferding *et al.*, 2022). Optical studies resolved the onset of circular dichroism and a subdomain structure in the CDW state that is consistent with the appearance of magnetic domains (Y. Xu *et al.*, 2022). This result is, however, under debate. It is seemingly at odds with polar Kerr measurements using Sagnac interferometry that fail to resolve signs of $\mathbf{q} = 0$ magnetic order (Saykin *et al.*, 2023; Wang, Farhang *et al.*, 2024).

Magnetic torque measurements also seemingly report the onset of TRS breaking, though at temperatures slightly above the onset of the CDW transition (Asaba *et al.*, 2024), thus inviting further studies exploring fluctuation phenomena above the CDW transition. Select x-ray studies have identified short-range order or fluctuations in this regime (Q. Chen *et al.*, 2022; Subires *et al.*, 2023), though the transition itself is weakly first order. However, Scheurer and Scammell (2025) recently argued that the torque response above the CDW temperature cannot be explained in terms of conventional CDW fluctuations or intraband magnetic order. Instead, an interband ordering mechanism enabled by symmetry-allowed interband SOC could naturally account for the observed odd-parity TRS-breaking nematic torque signal and associated hysteresis. In this picture the experimental observation is interpreted as a crossover rather than a true phase transition, which challenges the view that nematic or fluctuation-driven physics alone underlies the torque response.

Electronic structure. As discussed in an example in Sec. II.A.2, the electronic structure of V-based 135 compounds contains a multiorbital mixture of V d states and Sb p states crossing E_F. The key features are generally believed to be the p-type VHSs (derived from the V d states) that are close to or cross the Fermi level and an electronlike pocket at the Γ point derived from the Sb p_z states. Bulk quantum oscillation measurements identify several orbits with a nontrivial Berry phase in the CDW state (Fu *et al.*, 2021; Shrestha *et al.*, 2022), and analysis of the band structure classifies these materials as Z_2 topological metals with a protected surface state (Ortiz *et al.*, 2020; Tan *et al.*, 2021).

ARPES studies, in particular, have been instrumental in establishing the electronic band structure of AV_3Sb_5 kagome metals and its role within the rich landscape of symmetry-broken phases. Reviews by Hu, Wu *et al.* (2023) and Zhong, Yin, and Nakayama (2024) compiled the growing evidence of multiphase coexistence and ARPES-based spectral features relevant to kagome SC, and here we highlight a few key points. Early ARPES studies reported a momentum-dependent CDW gap, showing that the electronic states near the M points were particularly affected, whereas those near the Γ point remained gapless (Cho *et al.*, 2021; Nakayama *et al.*, 2021; Zhengguo Wang *et al.*, 2021). Subsequent works focused on the mapping of low-energy band features, uncovering multiple VHSs near the Fermi level and identifying m-type (saddle point) and p-type (symmetric) VHSs (Hu *et al.*, 2022b; Kang *et al.*, 2022).

Using angle- and photon-energy-dependent ARPES, it was further shown that CsV_3Sb_5 exhibits k_z-dependent VHS, indicating a 3D nature of the electronic structure. These studies shed initial light on the link between VHS and CDW formation by demonstrating Fermi-surface nesting, a hallmark of electronic instability. However, a study of KV_3Sb_5 further revealed energy gaps due to CDW-induced band folding and proposed electron-phonon coupling as a primary driver of CDW transitions (H. Luo *et al.*, 2022). The growing focus on electronic reconstruction led to a study of the CDW-induced peak-dip-hump structures in CsV_3Sb_5 (Lou *et al.*, 2022). ARPES data in this work indicated that the CDW phase strongly modulated the low-energy excitations, which is reminiscent of physics seen in strongly correlated superconductors. Collectively, these studies established that CDW ordering reorganizes the electronic structure of kagome metals at the Fermi surface, modifying both the DOS and the Fermi-surface topology.

Scanning tunneling microscopy. A great deal of electronic complexity has been revealed by STM measurements of 135 compounds. A variety of surface terminations and reconstructions contribute to this complexity (H. Chen *et al.*, 2021; Liang *et al.*, 2021; Qi Wang *et al.*, 2021; Xu *et al.*, 2021; Zhao, Li *et al.*, 2021; Li, Zhao, Ortiz *et al.*, 2022) with a large number of possibilities born from the mobile alkali atoms on the surface (Zhao, Li *et al.*, 2021; Nie *et al.*, 2022; Yu *et al.*, 2022; Han *et al.*, 2023; Meng *et al.*, 2023). In general, STM experiments have focused primarily on studying the Sb surface termination after sweeping away these mobile *A*-site ions.

The 2×2 CDW order in the kagome plane is detectable in STM images on both *A* (Liang *et al.*, 2021; Li, Zhao, Ortiz *et al.*, 2022; Nie *et al.*, 2022) and Sb surfaces (Jiang *et al.*, 2021; Liang *et al.*, 2021; Zhao, Li *et al.*, 2021). While the CDW state clearly breaks the translation symmetry of the lattice, which rotation symmetries are broken by this order are under debate. The results can be broadly categorized into two pictures. The first involves breaking of all reflection symmetries in the kagome plane, resulting in an inequivalence of the three CDW peaks in STM data and giving rise to a chiral CDW state (Jiang *et al.*, 2021; Shumiya *et al.*, 2021). The second CDW picture instead maintains a single in-plane reflection symmetry, while the other two are still broken (Li, Zhao, Ortiz *et al.*, 2022; Nie *et al.*, 2022). Experimentally, the distinction is whether two of the three inequivalent *M*-point peaks in the Fourier transform of the CDW pattern are identical or all three are distinct. It is under debate whether the apparent inequivalence of all three CDW peaks can be explained by STM tip anisotropy (Li, Zhao, Ortiz *et al.*, 2022) or strain can locally modulate the intensity of CDW peaks (Xing *et al.*, 2024; Y. Wang *et al.*, 2025). Temperature-dependent STM measurements have revealed that the symmetry-breaking signal persists up to at least 60 K (Li, Zhao *et al.*, 2023), and three 120°-rotated domains are imaged (Li, Zhao, Ortiz *et al.*, 2022; Nie *et al.*, 2022). This is consistent with the orthorhombic twinning and microsized domain formation imaged by optical birefringence measurements (Y. Xu *et al.*, 2022).

Signatures of broken TRS within the 2×2 CDW phase were first reported in STM measurements. Evidence here comes from examining the *M*-point intensities in Fourier-transformed STM data as a function of magnetic field, where *B* is applied and then reversed along the interlayer *c* axis. The reversal of the magnetic field is reported to change the relative intensities of the CDW peaks in some experiments, resulting in an apparent switch in the chirality of the CDW order (Jiang *et al.*, 2021; Xing *et al.*, 2024). Equivalent experiments performed by other groups, however, have reported no field-induced change to the CDW signal (Li, Zhao, Ortiz *et al.*, 2022; Li, Wan *et al.*, 2022; Candelora *et al.*, 2024). Discrepancies between the measurements potentially arise from one of two origins. The first is that the apparent change in the CDW intensities under different magnetic fields results from an experimental artifact from unconsidered, microscopic changes of the STM tip probe (i.e., reconfiguration of the atoms at the tip apex) between the datasets (Li, Zhao, Ortiz *et al.*, 2022; Candelora and Zeljkovic, 2025). The second potential origin is that small amounts of strain may locally

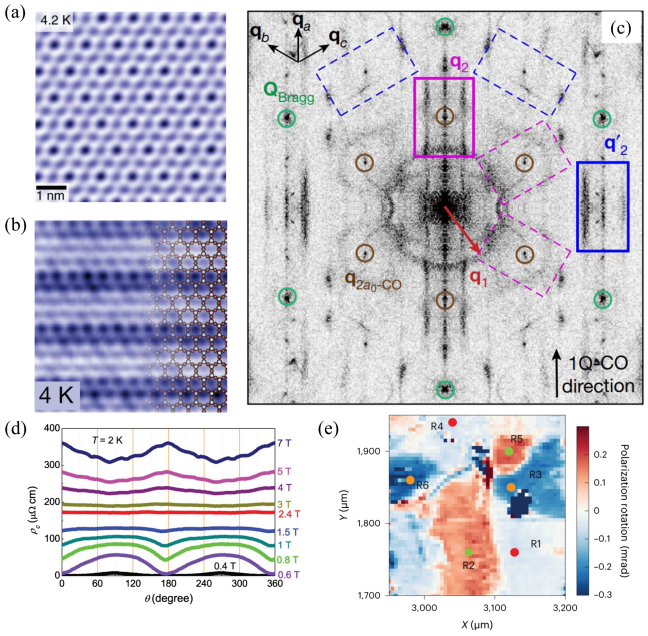

FIG. 28. (a) STM topograph of KV_3Sb_5 showing a 2×2 CDW. From Jiang *et al.*, 2021. (b) STM topograph of CV_3Sb_5 at 4.5 K showing additional 4×1 charge modulations. From Zhao, Li *et al.*, 2021. (c) Fourier transform of STM dI/dV map of CsV_3Sb_5 showing C_2-symmetric QPI from V bands, marked with q_2 and q'_2. From Zhao, Li *et al.*, 2021. (d) Angular dependence of *c*-axis resistivity in CsV_3Sb_5 measured at different in-plane magnetic fields. From Xiang *et al.*, 2021. (e) Spatial mapping of a polarization angle at 6 K in a RbV_3Sb_5 sample showing three types of equivalent domains rotated with respect to one another. From Y. Xu *et al.*, 2022.

suppress the TRS, and spatially inhomogeneous strain fields may generate the differing behaviors seen between STM measurements. Resolving this discrepancy via future STM experiments on strain-free samples attached without epoxy (Guo *et al.*, 2022) and with a meticulous examination of experimental artifacts (Candelora *et al.*, 2024; Candelora and Zeljkovic, 2025) is highly desirable.

STM measurements have also played a key role in identifying charge correlations that form beyond the 2×2 in-plane CDW order; see Fig. 28. Upon cooling in the CDW state, experiments reveal a unidirectional $4a_0$ charge order that forms on the Sb surface termination of CsV_3Sb_5 (below about 60 K) (Qi Wang *et al.*, 2021; Zhiwei Wang *et al.*, 2021; Zhao, Li *et al.*, 2021; Li, Wan *et al.*, 2022) and also in RbV_3Sb_5 (Shumiya *et al.*, 2021); however, it is notably absent, or relatively rare, on the equivalent Sb surface of KV_3Sb_5 (Jiang *et al.*, 2021; Li, Zhao, Ortiz *et al.*, 2022; Li *et al.*, 2023b). One hypothesis is that this stripe order stems from a set of small Fermi pockets, arising because of electronic band reconstruction upon entering the 2×2 CDW state (Zhou and Wang, 2022; Li *et al.*, 2023b). While the $4a_0$ charge-stripe order is absent as a static order parameter in scattering experiments (H. Li *et al.*, 2022), its well-defined onset below 60 K (Zhao, Li *et al.*, 2021) coincides with the temperature scale of lattice anomalies observed in bulk single crystals of CsV_3Sb_5. These include Raman spectroscopy (Wu *et al.*, 2022; Wulferding *et al.*, 2022) and time-resolved optical

reflectivity (Ratcliff *et al.*, 2021), suggesting that it is a manifestation of an energy scale present in the bulk.

Complementing ARPES measurements on 135 compounds, spectroscopic-imaging STM (SISTM) was used to measure electronic band structure at the nanoscale. SISTM mapping detected features associated with both the Sb-derived bands and the V-derived bands (H. Chen *et al.*, 2021; Zhao, Li *et al.*, 2021; Li *et al.*, 2023b; Li, Zhao *et al.*, 2023; Wu *et al.*, 2023); this finding is largely consistent with DFT calculations and ARPES measurements (Ortiz *et al.*, 2019, 2020). The signal from the V-derived bands shows pronounced unidirectional features, while the Sb-derived signal remains rotationally symmetric (Zhao, Li *et al.*, 2021; Li *et al.*, 2023b; Li, Zhao *et al.*, 2023; Wu *et al.*, 2023). Electron-phonon coupling is reported to renormalize the Fermi velocity of the in-plane vanadium bands, but preferentially along the symmetry-breaking direction, making the low-energy dispersion highly nonequivalent along the three lattice directions (Wu *et al.*, 2023).

SISTM measurements of CsV_3Sb_5 and KV_3Sb_5 reveal an emergence of quantum interference of quasiparticles below ≈35 K, a key signature for the formation of a coherent electronic state (Li, Zhao *et al.*, 2023). These quasiparticles, associated with V-derived kagome bands, display a pronounced unidirectional feature in reciprocal space that strengthens as the superconducting state is approached. This temperature is substantially below the formation of the $4a_0$ stripes (Zhao, Li *et al.*, 2021) or the 2×2 CDW phase (Ortiz *et al.*, 2020). This additional temperature scale was confirmed in subsequent STM experiments (Wu *et al.*, 2023; Q. Zhang *et al.*, 2024), as well as by multiple other probes reviwewed by Wilson and Ortiz (2024) such as nuclear magnetic resonance (NMR) measurements (J. Luo *et al.*, 2022; Song *et al.*, 2022), suggesting the formation of electronic coherence correlated with a structural crossover in the system.

Superconducting state. Turning now to the SC state, SC in AV_3Sb_5 compounds has been studied by a large number of probes, including tunnel diode oscillators (Duan *et al.*, 2021), scanning superconducting quantum interference devices (Kaczmarek *et al.*, 2024), ARPES (Zhong *et al.*, 2023b), heat capacity and thermal transport (Hossain *et al.*, 2025), point-contact tunneling (L. Yin *et al.*, 2021), irradiation studies (Roppongi *et al.*, 2023; W. Zhang *et al.*, 2023), μSR (Gupta *et al.*, 2022; Guguchia *et al.*, 2023b), and NMR (Mu *et al.*, 2021). These compounds host highly anisotropic quasi-two-dimensional SC states in the clean limit (Duan *et al.*, 2021). Broadly, the picture is one of a nodeless, multigap, singlet SC state whose smaller gap is anisotropic and whose larger gap is isotropic (Roppongi *et al.*, 2023; Grant *et al.*, 2025). STM experiments generally show a V-shaped superconducting gap, with nonzero conductance at zero energy, which is suggestive of a residual ungapped Fermi surface (H. Chen *et al.*, 2021; Liang *et al.*, 2021; Xu *et al.*, 2021). Some STM experiments also resolve multiple superconducting gaps in differential conductance spectra (Xu *et al.*, 2021). μSR measurements in select compounds claim to resolve a nodal gap (Guguchia *et al.*, 2023b); however, this differs from conclusions of tunnel diode oscillator measurements. Mine *et al.* (2024) recently reported ultra-high-resolution laser-based ARPES to directly probe the anisotropic superconducting gap in CsV_3Sb_5. Strong orbital selectivity was observed in the gap structure: V-based $3d$ orbitals exhibited an 80% gap anisotropy, whereas Sb-derived bands retained an isotropic gap. This provides strong evidence that SC is intertwined with CDW-driven Fermi-surface reconstruction, possibly pointing to an unconventional pairing mechanism.

Constraining interpretations of these combined data, theoretical treatment of a kagome metal with p-type VHS at E_F (Holbæk *et al.*, 2023; Dai, Kreisel, and Andersen, 2024) showed that traditional BCS-like metrics of a Hebel-Slichter peak in NMR (Mu *et al.*, 2021) and resilience to nonmagnetic disorder upon irradiation (Roppongi *et al.*, 2023) fail to exclude sign-changing, singlet SC order parameters. This aggregate picture suggests the pairing symmetry to be s^{++}, s^{+-}, or $d + id$, with $d + id$ favored if TRS is broken in the SC state. Curiously, the signature of TRS reported by μSR measurements below the CDW transition reappears below the SC transition once long-range CDW order is suppressed via hydrostatic pressure (Guguchia *et al.*, 2023b). One additional aspect of research into the SC state of AV_3Sb_5 is the presence of unconventional phenomena in the fluctuation regime of the SC state, such as an unusual extended vortex regime (X. Zhang *et al.*, 2024) and the proposal of a composite $6e$-pairing condensate (Varma and Wang, 2023; Ge *et al.*, 2024).

Studies of the surface-dependent electronic structure include a report of topological surface states and flat bands in CsV_3Sb_5 (Hu *et al.*, 2022a) that is germane to connate models of topological superconductivity (Fu and Kane, 2008). In addition, similar work shows that SC emerges within the CDW-modified structure, with partial CDW gap suppression and enhanced low-energy spectral weight (Kato *et al.*, 2023). Different surface terminations drastically affect the electronic structure, with some terminations suppressing CDW order locally (Huai *et al.*, 2022; Kato, Li *et al.*, 2022). A recent STM study has shown that manipulation of surface alkali ions can locally fault the CDW stacking and suppress the CDW gap, resulting in a higher T_c surface SC state that potentially couples to the Z_2 topological surface state (Han *et al.*, 2025b).

Impact of pressure and strain. A number of studies have also explored the impact of hydrostatic pressure and strain on the electronic properties of V-based 135 compounds. Hydrostatic pressure has been shown to rapidly suppress the CDW transition while enhancing the SC transition, which eventually forms a domelike feature (K. Chen *et al.*, 2021; Du *et al.*, 2021). At even higher pressures (beyond the initial suppression of SC), SC eventually reappears. The disappearance and reemergence of SC correlates to the presence of Sb states at the E_F and suggests their importance for both SC and the CDW order (Jeong *et al.*, 2022; Ritz, Fernandes, and Birol, 2023; Tsirlin *et al.*, 2023).

CsV_3Sb_5, unlike its Rb- and K-based cousins, shows the formation of a "double-dome" SC state in the low-pressure regime (K. Chen *et al.*, 2021; Yu, Ma *et al.*, 2021). This has been linked to the presence of a distinct CDW phase for CsV_3Sb_5 (discussed earlier) and an evolution into a competing

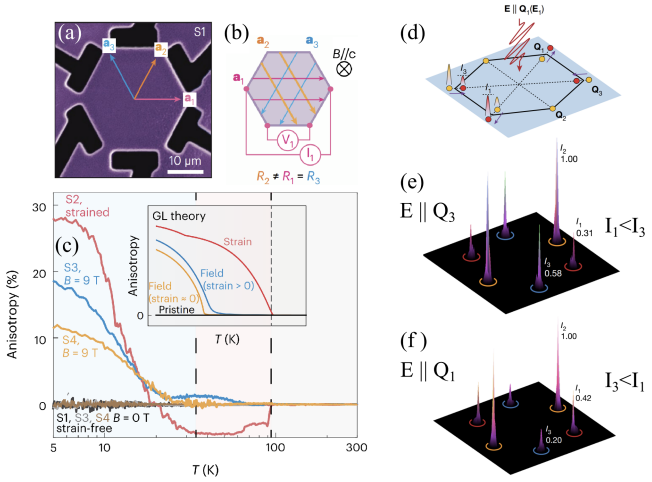

FIG. 29. (a),(b) CsV_3Sb_5 crystal fabricated into a device for mitigating strain and measuring in-plane transport anisotropy and the corresponding measurement geometry. (c) Resulting transport anisotropy measured with and without extrinsic strain showing negligible in-plane anisotropy when strain is largely suppressed. An out-of-plane magnetic field drives the reappearance of in-plane anisotropy in strain-free crystals. From C. Guo *et al.*, 2024. (d) Measurement geometry for STM measurements conducted under optical illumination. From Xing Xing *et al.*, 2024. (e), (f) Change in intensities of the Fourier-transformed pattern of CDW peaks driven via the alignment of an in-plane optical polarization, signifying a shift in the pattern of CDW order.

CDW phase (Stier *et al.*, 2024). Externally applied in-plane strain induces a modest suppression of the CDW state and a slight enhancement of T_c (Qian *et al.*, 2021). STM experiments reveal an unusually high decoupling rate between the direction of electronic unidirectionality and anisotropic strain, revealing weak smectoelastic coupling in the 2×2 CDW phase of kagome superconductors (Y. Wang *et al.*, 2025). The $4a_0$ charge-stripe order appears to be easily suppressed by strain induced by buckling in the sample (Y. Wang *et al.*, 2025). Both the impact of in-plane uniaxial strain and nominally hydrostatic pressure are driven largely by changes in the c axis, either via the Poisson ratio or via anisotropic compressibility of the lattice.

Related to strain, one line of inquiry is the potential impact of extrinsic strain (for example, due to differential cooling between a crystal and its sample mount) on the measured properties of AV_3Sb_5 compounds. Small amounts of strain at the order of 0.1% can suppress the TRS-breaking or chiral signal in transport experiments of nearly strain-free samples (Guo *et al.*, 2022). Experiments have further reported that an applied out-of-plane magnetic field (C. Guo *et al.*, 2024; Xing *et al.*, 2024) or light pulse with an in-plane polarization in select directions can drive an in-plane transport anisotropy or modulate the in-plane propagation vectors of the CDW state (Xing *et al.*, 2024), as shown in Fig. 29. These measurements suggest the presence of an intrinsic piezomagnetic order parameter and a TRS-broken CDW state in AV_3Sb_5, one whose signatures in optics, magnetotransport, and STM measurements would be highly sensitive to the presence of extrinsic global or local strain fields imposed within the crystal under study. The magnetic-field-induced structural and electronic response in STM measurements, however, has subsequently been questioned and alternatively attributed to experimental artifacts (Candelora and Zeljkovic, 2025).

Chemical doping. A tremendous amount of studies exploring the impact of tuning E_F in AV_3Sb_5 via chemical substitution or doping have been performed. Hole-doping (Sn or Ti) (Oey *et al.*, 2022; Y. Liu *et al.*, 2023) and electron-doping (Te or Cr) studies (Ding *et al.*, 2022; Capa Salinas *et al.*, 2023) reveal a CDW order parameter that is rapidly suppressed upon tuning the proximity of the VHS relative to the Fermi level. ARPES studies directly reveal that doping the vanadium site shifts the VHS positions, affecting the CDW stability and enhancing SC (Kato *et al.*, 2022). Compared to the known evolution of the CDW upon doping, the microscopic nature of the CDW state and its relationship to the electronic structure and band folding can be resolved (Kang *et al.*, 2023). The impact of carrier doping is largely orbitally selective, with a large change in the Sb p_z pocket's filling (LaBollita and Botana, 2021), and, as in pressure studies, SC seemingly vanishes coincident with the disappearance of this pocket. Paralleling the phenomenology of pressure studies, CsV_3Sb_5 uniquely develops a double-dome SC feature (Oey *et al.*, 2022) with signatures of a nearby competing pattern of charge correlations (Kautzsch *et al.*, 2023). A nematic quantum critical point has been proposed to account for this unusual evolution of T_c across the phase diagram (Sur *et al.*, 2023). Isoelectronic substitution on the V site similarly has a strong impact on the CDW and SC transitions (Y. Li *et al.*, 2022; M. Liu *et al.*, 2022), while isoelectronic substitution on the alkali site largely interpolates CDW and SC behaviors among the 135 end members (Ortiz, Capa Salinas *et al.*, 2023).

Nematicity and PDW order. Moving beyond conventional CDW descriptions, electronic nematicity in KV_3Sb_5 was identified using ARPES, demonstrating that the CDW phase breaks C_3 symmetry by forming a unidirectional electronic modulation (Z. Jiang *et al.*, 2023b). Similarly, Li *et al.* (2023b) found that the Fermi surface exhibits small reconstructed pockets corresponding to an intertwined charge-stripe order in AV_3Sb_5 compounds. They suggested that, beyond a simple CDW, the fermiology of AV_3Sb_5 might support additional orders, including a potential PDW coexisting with SC. At low temperatures STM studies report the observation of an additional $3q$ CDW-like wave vector linked to the local modulation of the superfluid density, suggesting a PDW instability (H. Chen *et al.*, 2021; Deng *et al.*, 2024b).

A host of experimental studies have revealed a rich landscape of competing and cooperating phases in AV_3Sb_5 materials, but fundamental questions remain unanswered. Chief among them is the potential presence and precise role of TRS breaking in both the CDW and SC states and the underlying SC pairing mechanism. The relative role of electron-phonon coupling versus Fermi-surface nesting effects in driving both CDW and SC order remain under debate (Ritz *et al.*, 2023). Electron-phonon coupling, initially thought to be small (Tan *et al.*, 2021), was later shown to be appreciable, and nonequilibrium studies have shown that lattice vibrations couple kagome band features (Zhong *et al.*, 2024). The role of extrinsic strain in many of the

discrepancies reported between experimental studies using the same technique and different experimental probes (each reporting the existence or absence of TRS) is a key issue that must be resolved. *In situ* strain-tuning techniques as well as careful strain mapping measurements carried out in combination with optical, STM, magnetotransport, and x-ray scattering measurements will be crucial for solving this issue.

b. $CsCr_3Sb_5$ *compounds*

$CsCr_3Sb_5$ is an isostructural cousin of CsV_3Sb_5 (Y. Liu *et al.*, 2024) with a kagome net composed of Cr atoms. This metastable phase can be grown in bulk crystal form via a high-temperature, crucible-based self-flux growth method (Y. Liu *et al.*, 2024). Unlike members of the AV_3Sb_5 family, it exhibits an electronic flat band that is favorably placed near Fermi level (Y. Guo *et al.*, 2024; Y. Liu *et al.*, 2024; Peng *et al.*, 2024; Li *et al.*, 2025; Xie *et al.*, 2025; Z. Wang *et al.*, 2025), and it is also believed to be magnetic and more strongly correlated (Sangiovanni, 2024; Crispino *et al.*, 2025; Chatzieleftheriou *et al.*, 2026). At ambient conditions it undergoes a $4a_0$ structural transition at 55 K observed by XRD measurements that was also reported to be accompanied by a magnetic transition (Y. Liu *et al.*, 2024). Under pressure this phase transition evolves into two separate transitions at different temperatures that are interpreted as spin density waves or CDWs. Both of these density wave transitions are gradually suppressed as SC ultimately emerges above 3.65 GPa, peaking at $T_c \approx 6.4$ K (Y. Liu *et al.*, 2024). Note that at intermediate pressures, both SC and magnetism are believed to coexist (Y. Liu *et al.*, 2024). The nature of emergent SC, however, remains to be determined. Recent STM experiments image a similar $4a_0$ density wave on the surface similar to those in the V-based 135 compounds and further reveal the emergence of another unidirectional charge density wave below 45 K (Cheng *et al.*, 2025). This lower-temperature density wave breaks all mirror symmetries but preserves the mirror-glide symmetry (Cheng *et al.*, 2025), and it may potentially be connected to an altermagnetic state (Huang *et al.*, 2025). First-principles and RPA calculations suggest that antiferromagnetic fluctuations are crucial for mediating SC in this system (Wu *et al.*, 2025). There is also little known about the nature of magnetism, with theoretical proposals for 4×2 altermagnetic spin-density-wave state and other energetically favorable phases close by (Xu *et al.*, 2025).

c. ATi_3Bi_5 *compounds*

ATi_3Bi_5 (A = Cs or Rb) crystallizes in the same structure as its AV_3Sb_5 counterpart but with a kagome net composed of Ti atoms instead of V (Werhahn *et al.*, 2022; Yang *et al.*, 2022). It is synthesized via similar high-temperature crucible-based self-flux growth techniques. Like AV_3Sb_5, it is nonmagnetic (Werhahn *et al.*, 2022; H. Yang *et al.*, 2024). While some studies show that $CsTi_3Bi_5$ is superconducting below $T_c \approx 4.8$ K (H. Yang *et al.*, 2024), SC has not been observed in other studies (Werhahn *et al.*, 2022; Y. Wang *et al.*, 2023). The discrepancy may lie in the small superconducting volume fraction of impurity phases and low critical magnetic fields that necessitate screening Earth's magnetic fields (H. Yang *et al.*, 2024). The superconducting T_c of 4.8 K is substantially higher than the theoretically predicted ≈2 K in both Cs and Rb variants (Yi *et al.*, 2023).

In contrast to AV_3Sb_5, experiments on ATi_3Bi_5 reveal no obvious anomalies in magnetization, resistivity, or heat capacity indicative of a CDW state (Werhahn *et al.*, 2022; Xintong Chen *et al.*, 2023; Y. Wang *et al.*, 2023). Phonon calculations also show no imaginary phonons (Z. Jiang *et al.*, 2023a; Li *et al.*, 2023a), therefore further supporting the absence of a CDW instability. This in turn provides an opportunity to explore electronic phenomena in this class of nonmagnetic kagome metals in the absence of translational symmetry-breaking CDW.

From the fermiology perspective, ATi_3Bi_5 hosts VHS at M points, but they are positioned well above the Fermi level (Y. Hu *et al.*, 2023; Z. Jiang *et al.*, 2023a; B. Liu *et al.*, 2023; Y. Wang *et al.*, 2023; Yang *et al.*, 2023), unlike the equivalent features in AV_3Sb_5 that appear to be closer to the Fermi level. It may be possible to shift these VHSs closer to the Fermi level under pressure (Yi *et al.*, 2023). ARPES experiments reveal that a partial flat band is located several hundred meV below the Fermi level [see Figs. 30(a)and 30(b)] (Y. Hu *et al.*, 2023; Z. Jiang *et al.*, 2023a; Yang *et al.*, 2023), which was also inferred from infrared spectroscopy (Cao *et al.*, 2025).

First-principles calculations have predicted that $CsTi_3Bi_5$ will have robust topological surface states (Y. Wang *et al.*, 2023), some of which could be further tuned by pressure (Yi *et al.*, 2023; W. Wu *et al.*, 2024). Topological surface states have been visualized in ARPES in $RbTi_3Bi_5$ (Y. Hu *et al.*, 2023; Z. Jiang *et al.*, 2023a) and $CsTi_3Bi_5$ (Yang *et al.*, 2023), and the topological nature of certain Fermi surfaces has also been inferred from quantum oscillations (Dong *et al.*, 2024). Dirac nodal lines are also detected in $CsTi_3Bi_5$ (Yang *et al.*, 2023) and $RbTi_3Bi_5$ (Y. Hu *et al.*, 2023; Z. Jiang *et al.*, 2023a). Overall, the electronic band structure extracted from ARPES (Y. Hu *et al.*, 2023; Z. Jiang *et al.*, 2023a; B. Liu *et al.*, 2023; Y. Wang *et al.*, 2023; Yang *et al.*, 2023) and STM (Li *et al.*, 2023a; H. Yang *et al.*, 2024) and the Fermi surface determined from quantum oscillations (Rehfuss *et al.*, 2024) show a reasonable agreement with DFT calculations, suggesting only a modest degree of electronic correlations in the system.

Rotation symmetry breaking, or electronic nematicity, is reported in this family of materials using several complementary probes. Notably, it emerges without any accompanying CDW states, in sharp contrast to AV_3Sb_5. Spectroscopic-imaging STM measurements have revealed electronic rotation symmetry breaking in Fourier transforms of differential conductance maps (Li *et al.*, 2023a; H. Yang *et al.*, 2024); see Fig. 30(c). In particular, by comparing the wavelengths and amplitudes of scattering wave vectors along different directions in reciprocal space, STM experiments have detected electronic anisotropy that breaks the sixfold symmetry of the lattice [see Figs. 30(d) and 30(e)] (Li *et al.*, 2023a; H. Yang *et al.*, 2024) arising from both in-plane and out-of-plane titanium-derived d orbitals (Li *et al.*, 2023a). Polarization-dependent ARPES has shown orbital-selective electronic nematicity in $RbTi_3Bi_5$ (Y. Hu *et al.*, 2023) and $CsTi_3Bi_5$ (Bigi *et al.*, 2026). Autocorrelation of the ARPES Fermi surface of $RbTi_3Bi_5$ is also consistent with rotation symmetry breaking, which has been reported to persist to 200 K

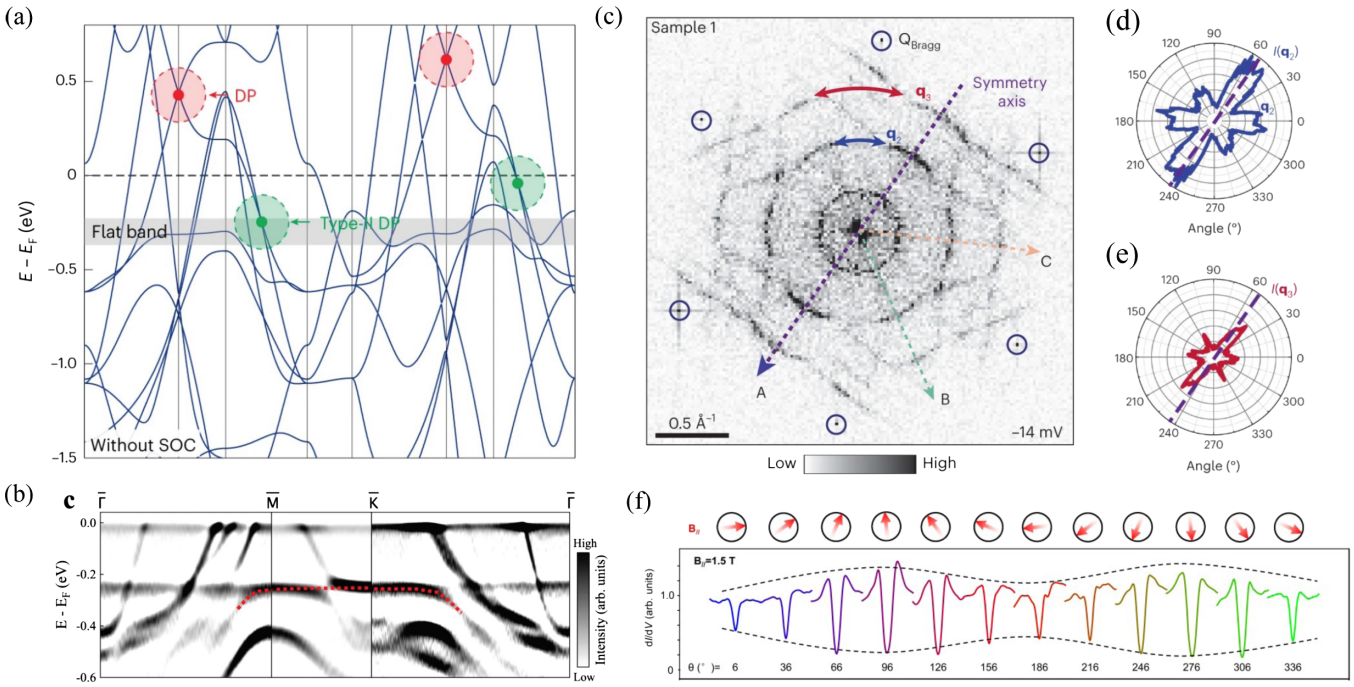

FIG. 30. (a) DFT-calculated electronic structure of $RbTi_3Bi_5$ without SOC (Y. Hu *et al.*, 2023). Flat-band, Dirac point, and type-II Dirac nodal lines are denoted. (b) Second derivative image with respect to energy obtained from raw ARPES data of $CsTi_3Bi_5$ along the Γ–M–K–Γ direction (Yang *et al.*, 2023). The flat band is highlighted by dotted red lines. (c) Fourier transform of a normalized STM differential conductance map at -14 meV showing twofold symmetric scattering and interference of electrons on the surface of $CsTi_3Bi_5$. From Li *et al.*, 2023a. (d),(e) Angle-dependent Fourier-transform amplitudes of q_2 and q_3 scattering wave vectors from (c), both plotted in polar coordinates on the same scale. From Li *et al.*, 2023a. (f) Panorama of dI/dV spectra showing a superconducting gap on the surface of $CsTi_3Bi_5$ at different in-plane magnetic field orientations exhibiting twofold rotational symmetry (H. Yang *et al.*, 2024).

(Z. Jiang *et al.*, 2023a), and a comparable onset temperature of 150 K was inferred from anomalous phonon line shapes in infrared spectroscopy experiments (Wenzel *et al.*, 2025).

The origin of nematicity has been hypothesized to be an electron correlation-driven Pomeranchuk instability (Bigi *et al.*, 2026). An anomalous spin-optical helical effect suggestive of loop current circulation in $CsTi_3Bi_5$ has also been reported (Mazzola *et al.*, 2025). When SC is observed, the superconducting gap size under in-plane magnetic field also exhibits a twofold symmetry that is consistent with the parent state electronic nematicity (H. Yang *et al.*, 2024); see Fig. 30(f). Hu, Le *et al.* (2024) provides a more in-depth review specific to this family of materials.

3. RM_6X_6 compounds

Kagome metals with the chemical formula AM_6X_6, often referred to as 166 compounds, form with a broad array of elements where the R and M sites are occupied predominantly with rare-earth ($R = Y$, Sc, La, or Lu) and transition-metal ions and the M-site ions are commonly Sn or Ge. In the stoichiometric limit, the structures most commonly studied are those that form in the hexagonal $P6/mmm$ $HfFe_6Ge_6$-type cell, and these can be thought of as a modification of the CoSn-type cell due to the addition of a triangular lattice A-site plane between the kagome planes. The result is a bilayer kagome lattice interleaved with a triangular lattice of A-site ions, and it is one where the X-site ions (nominally within the kagome plane in 11-type structures) are now displaced above and below the kagome plane. Studies of 166 materials can be roughly separated into those with magnetic and nonmagnetic kagome sites. AM_6X_6 compounds with $M =$ Fe, Mn, or Cr are the most common magnetic variants, while those with $M =$ V or Nb have nonmagnetic sites. In the following discussion, we first focus on the magnetic M-site variants and then return to the nonmagnetic M-site members.

a. RMn_6Sn_6 *compounds*

Strongly magnetic members of the 166 family have been studied extensively as hosts of noncollinear magnetic ground states born via a number of mechanisms. Interlayer frustration between kagome planes of magnetic M-site variants has long been known to promote the formation of double-flat and other spiral states (Rosenfeld and Mushnikov, 2008), and tuning the relative interactions between the kagome planes as well as coupling magnetic A-site moments can lead to a host of complex magnetic phase diagrams (Schobinger-Papamantellos, Rodríguez-Carvajal, and Buschow, 1997; Malaman *et al.*, 1999; Riberolles *et al.*, 2024; L, Trevisan, and McQueeney, 2025). We do not focus on the diversity of these states here and instead focus on phenomena derived from electronic instabilities and interactions endemic to the kagome networks and band structures of 166 compounds.

An early focus of studies of magnetic Mn-based 166 compounds was their unconventional magnetotransport

properties, and single crystals can be grown via Sn-based flux methods (Clatterbuck and Gschneidner, 1999). When the Dirac crossings arising from the kagome network are close to the Fermi level, an out-of-plane ordering of the magnetic moments can generate a large Chern gap, and a large AHE is predicted to result. Strong SOC can similarly gap the Dirac point, but the appeal of a field-switchable response requires the presence of tunable out-of-plane moments.

Absent anisotropies from interstitial magnetic R-site ions, the M moments orient ferromagnetically within the basal planes modulated along the c axis in a helical ground state in the case of $M = \mathrm{Mn}$. Specifically, when the R sites are nonmagnetic, such as in $R\mathrm{Mn_6Sn_6}$ ($R = \mathrm{Sc}$, Y, and Lu), an incommensurate, spiral state forms within the Mn kagome network, with moments aligning in the kagome plane and winding along the interplane direction (Venturini, Fruchart, and Malaman, 1996). An in-plane field can induce an out-of-plane component to the magnetization and a noncollinear spin texture with real-space spin chirality. For instance, an in-plane field in $\mathrm{YMn_6Sn_6}$ has been shown to induce a transverse conical spiral state induced by thermal fluctuations (Ghimire *et al.*, 2020), leading to the formation of a strong topological Hall effect. Similar effects have been reported in $\mathrm{ScMn_6Sn_6}$ (H. Zhang *et al.*, 2022) and $\mathrm{LuMn_6Sn_6}$ (Mozaffari *et al.*, 2025). By tuning the out-of-plane magnetic field, STM experiments reported an anomalous momentum-dependent g factor associated with the gapped Dirac point (Li, Zhao, Jiang *et al.*, 2022). In-plane magnetic field experiments further show additional tunability of the g factor that is strongly dependent on the in-plane crystalline direction (Jia *et al.*, 2024).

Adding anisotropic moments via magnetic lanthanide R-site ions can induce a ferrimagnetic c-axis aligned moment for strongly uniaxial $\mathrm{Tb^{3+}}$ (El Idrissi *et al.*, 1991), as well as out-of-plane canting for $\mathrm{Ho^{3+}}$ and $\mathrm{Dy^{3+}}$. For $M = \mathrm{Mn}$, all of these ions induce some degree of collinear spin reorientation transitions upon cooling as the in-plane anisotropies of the stronger exchange-coupled Mn moments give way to the anisotropies of the lanthanide moment network (Riberolles *et al.*, 2022). The filling of the kagome band structure places Dirac points and saddle points just below and above E_f (M. Li *et al.*, 2021). Unconventional magnetotransport effects are also reported in $R\mathrm{Mn_6Sn_6}$ ($R = \mathrm{Er}$ or Tm), where an in-plane helical magnetic state persists (Dhakal *et al.*, 2021; Wang, Yi *et al.*, 2022).

For $\mathrm{TbMn_6Sn_6}$ in particular, the ground state forms a c-axis aligned ferrimagnetic state of antialigned Mn and Tb moments, generating a sizable $6\mu_B$ c-axis aligned moment. This ordered state, combined with the Dirac crossing close to E_F led to the report of a Chern-gapped state, intrinsic anomalous Hall conductivity, and topological edge states mapped via STM (Yin *et al.*, 2020b). Quantum oscillation measurements and Nernst effect data reveal a quasi-two-dimensional orbit with a nontrivial Berry phase as well as an anomalous thermal Hall signal (X. Xu *et al.*, 2022). The origin of the anomalous Hall conductivity as deriving primarily from the quasi-2D Dirac band features, however, is under debate (Lee *et al.*, 2023; Jones *et al.*, 2024).

b. $R(\mathrm{Fe,Cr})_6(\mathrm{Sn,Ge})_6$ *compounds*

Other variants with potentially magnetic M sites include $R\mathrm{Fe_6(Ge,Sn)_6}$ and $R\mathrm{Cr_6(Ge,Sn)_6}$ (Schobinger-Papamantellos, Rodríguez-Carvajal, and Buschow, 1997; Cadogan *et al.*, 2000), though these compounds often suffer from vacancies and off-stoichiometries within the Ge/Sn sublattices. Bulk crystals are typically grown via Sn- or other metal-based flux methods (Avila *et al.*, 2005). Compounds such as $\mathrm{YFe_6Sn_6}$ form in both disordered $\mathrm{YCo_6Ge_6}$-type and vacancy-ordered $\mathrm{HoFe_6Sn_6}$-type structures, and magnetic R-site variants form various mixtures of these phases (El Idrissi, Venturini, and Malaman, 1991). A similar case occurs with $M = \mathrm{Cr}$ variants (Schobinger-Papamantellos, Rodríguez-Carvajal, and Buschow, 1997), though some reports claim that $\mathrm{YCr_6Ge_6}$ forms in the fully ordered structure where elements of the Cr-based kagome band structure were investigated (Wang *et al.*, 2020). The structurally ordered $\mathrm{YCr_6Ge_6}$ variant is characterized as a Pauli paramagnet with moderate correlation effects in transport and a partially flat band predicted to form just below E_F (Ishii *et al.*, 2013). There is considerable opportunity in the future exploration of these compounds if processing routes forming stoichiometric crystals can be developed. This is interesting, in particular, because of their ability to mix magnetic R-site networks with magnetic kagome (M-site) networks with variable electronic filling.

c. $R\mathrm{V_6Sn_6}$ *compounds*

An ordered 166 structure also forms with the nonmagnetic M-site ion V, where an array of fully ordered $R\mathrm{V_6Sn_6}$ ($R = \mathrm{Sc}$, Y, Gd, or Lu) compounds are known to stabilize (Romaka *et al.*, 2011), and bulk crystals can again be grown via Sn-based flux methods (Pokharel *et al.*, 2021). The band structures of these compounds, like their Mn-based cousins, have Dirac crossings and saddle points that are close to E_F (Peng *et al.*, 2021; Hu, Wu *et al.*, 2022), and, for nonmagnetic R sites, they can be categorized as topological $\mathbb{Z}_2$ metals (Pokharel *et al.*, 2021).

Magnetism within the R-site network is determined by a combination of the frustrated triangular lattice motif, Ruderman-Kittel-Kasuya-Yosida coupling, and anisotropies imposed by the spin-orbit entangled wave function of the lanthanide ground state multiplet. Varying the character of the magnetic R site can tune the magnetic anisotropy and the nature of the order (Lee and Mun, 2022; X. Zhang *et al.*, 2022). While $(\mathrm{Y,Lu})\mathrm{V_6Sn_6}$ is nonmagnetic, $\mathrm{YbV_6Sn_6}$ has an easy-plane anisotropy and exhibits signs of heavy fermion behavior in its low-temperature electronic properties (Guo *et al.*, 2023), and $(\mathrm{Tm,Er})\mathrm{V_6Sn_6}$ also possesses easy-plane anisotropy and antiferromagnetic order (Zhou *et al.*, 2024). $(\mathrm{Ho,Dy})\mathrm{V_6Sn_6}$ shows weak easy-axis anisotropy and ferromagnetism, while $\mathrm{TbV_6Sn_6}$ is strongly uniaxial with $\mathrm{Tb^{3+}}$ moments oriented out of the plane (Pokharel *et al.*, 2022; Rosenberg *et al.*, 2022). $\mathrm{GdV_6Sn_6}$, in contrast, has a nearly isotropic spin-only state that forms an incommensurate helical modulation along the interplane direction (Porter *et al.*, 2023). Larger R-site ions such as Sm result in the formation a disordered 166 variant (X. Huang *et al.*, 2023).

In strongly uniaxial TbV_6Sn_6, strong SOC and the resulting mass gap of Dirac bands at the Fermi level generates strong spin-Berry curvature effects and large orbital magnetic moments, which were detected via their Zeeman coupling to a magnetic field in QPI measurements (Li *et al.*, 2024). Spin-resolved ARPES also provides evidence for finite spin-Berry curvature contributions at the center of the BZ, where the electronic flat band detaches from the Dirac band because of SOC (Di Sante *et al.*, 2023). Even when magnetism is absent, such as in YV_6Sn_6, quantum oscillation measurements similarly detect a nontrivial Berry phase and light electron masses assigned to multiple Dirac crossings near E_F in addition to heavy orbits attributed to nearby VHSs (Rosenberg *et al.*, 2024). Similar effects are seen in GdV_6Sn_6 (Dhital *et al.*, 2024) and have recently been reported as nonmagnetic variants $(Ti, Zr, Hf)V_6Sn_6$ (He *et al.*, 2024).

Despite VHSs existing close to E_F across the broader family of RV_6Sn_6 compounds and a qualitatively similar filling of the kagome sublattice to AV_3Sb_5 compounds, no purely electronic phase transitions manifest in the absence of magnetic order. Owing to the lack of a dominant steric role, neither CDW order nor SC emerge down to 50 mK in stoichiometric (undoped compounds). However, one notable exception occurs when the size of the *R*-site ion is decreased below a critical threshold, as in the case of ScV_6Sn_6, which we discuss next.

d. ScV_6Sn_6 *compounds*

Like YV_6Sn_6, ScV_6Sn_6 can be grown via a Sn-based flux method and does not show magnetic ordering or SC down to 80 mK (Arachchige *et al.*, 2022). It hosts a band structure similar to YV_6Sn_6, and quantum oscillation experiments have suggested that the electron Dirac band located at the *K* point is characterized by a finite Berry phase, which infers a topologically nontrivial Fermi surface (Shrestha *et al.*, 2023; Yi, Feng, Mao *et al.*, 2024; Zheng *et al.*, 2024). Topological Dirac surface states have also been observed near the Γ point in ARPES measurements (Hu *et al.*, 2024).

Notably, ScV_6Sn_6 is unique in that it hosts a first-order phase transition into a CDW-like phase below $T^* \approx 92$ K with the $\bar{K}$ $\mathbf{q} = (1/3, 1/3, 1/3)$ wave vector (Arachchige *et al.*, 2022). This corresponds to an enlargement of the unit cell by $\sqrt{3} \times \sqrt{3} \times 3$ and a lowering of the lattice symmetry to an *R*32 cell. The transition is reflected in concomitant discontinuities in magnetization, resistivity, and heat capacity data (Arachchige *et al.*, 2022); see Fig. 31(a). The absence of a gradual spectral gap opening from optical spectroscopy (T. Hu *et al.*, 2023) and abrupt spectral weight redistribution at T^* from ARPES (S. Cheng *et al.*, 2024) further indicate the first-order nature of the transition. Lattice distortions accompanying the CDW-like transition come primarily from a chainlike instability driven by the motion of the out-of-plane Sc and Sn_1 atoms, each with up to 0.16 Å out-of-plane displacements. The kagome net V atoms, however, show substantially weaker displacements (Arachchige *et al.*, 2022) that are consistent with *ab initio* calculations (Tan and Yan, 2023).

Understanding charge ordering in ScV_6Sn_6 is the subject of a number of theoretical works (Cao *et al.*, 2023; Tan and Yan, 2023; S. Liu *et al.*, 2024; Subedi, 2024; Wang, Chen *et al.*, 2024). Strong anharmonic effects (Wang, Chen *et al.*, 2024), order-disorder transitions (S. Liu *et al.*, 2024), and an interplay between electron-phonon coupling soft-phonon fluctuations of a locally flat *H* mode are a few examples (Hu *et al.*, 2025). In particular, the $(1/3, 1/3, 1/2)$ CDW wave vector initially appeared from theory to be energetically favorable (Cao *et al.*, 2023; Tan and Yan, 2023; S. Liu *et al.*, 2024), which contrasts with the experimentally observed $\mathbf{q} = (1/3, 1/3, 1/3)$ distortion (Arachchige *et al.*, 2022). Both elastic and inelastic x-ray scattering experiments instead reveal short-range charge order and phonon softening along $\mathbf{q} = (1/3, 1/3, 1/2)$ at temperatures much higher than T^* (Cao *et al.*, 2023; Korshunov *et al.*, 2023; Pokharel *et al.*, 2023).

The apparent onset temperature of this short-range charge order varies among reports due to differences in experimental resolution, but signatures are reported as high as room temperature. In addition, weak short-range order in some cases persists below T^*, potentially pinned by variable levels

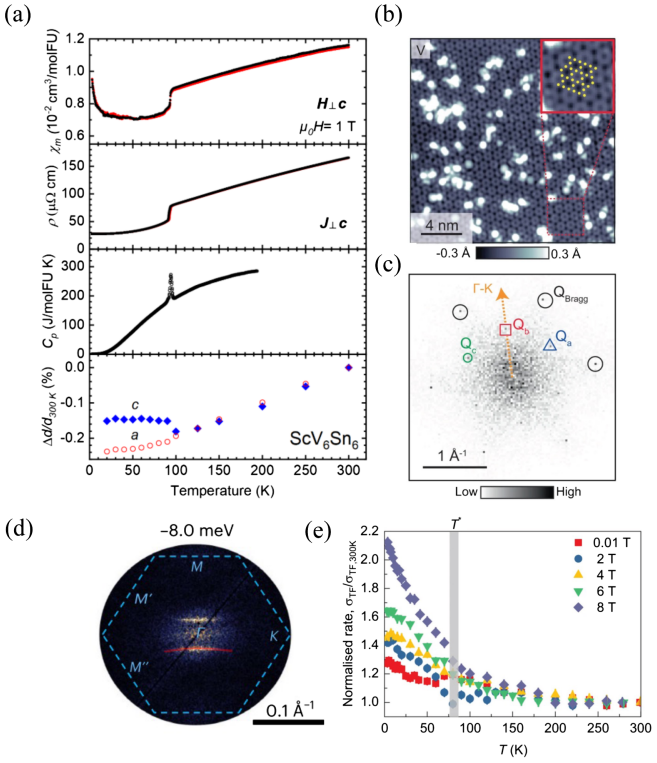

FIG. 31. (a) Temperature dependence of magnetic susceptibility on cooling (black line) and warming (red line) of bulk single crystals of ScV_6Sn_6 (top panel), temperature dependence of resistivity in the *a*-*b* plane measured on cooling (black line) and warming (red line) (second panel), specific heat capacity (third panel), and relative change in lattice parameters vs temperature (bottom panel). From Arachchige *et al.*, 2022. (b),(c) STM topograph and associated Fourier transform showing the CDW peaks (enclosed by triangles). From S. Cheng *et al.*, 2024. (d) Fourier transform of STM dI/dV map showing unidirectional electron scattering and interference signature. From Jiang *et al.*, 2024. (e) Temperature dependence of the high transverse field muon spin relaxation rate in μSR normalized to the value at 300 K, measured under different *c*-axis magnetic fields. From Guguchia *et al.*, 2023a.

of disorder in different samples (Pokharel *et al.*, 2023). The fluctuations associated with the buildup of short-range $(1/3, 1/3, 1/2)$ order couple to charge carriers, where transport data suggest the presence of a pseudogap phase above T^* (DeStefano *et al.*, 2023).

In general, phonons and lattice effects are believed to play the primary role in the formation of the CDW-like phase in ScV_6Sn_6 (Korshunov *et al.*, 2023; Tuniz *et al.*, 2023; Hu *et al.*, 2024; S. Lee *et al.*, 2024), and any purely electronic instabilities are likely to play a secondary role. This notion has been supported by ARPES measurements, which have observed similar VHSs near the Fermi level in both ScV_6Sn_6 and other 166 systems (S. Cheng *et al.*, 2024; Z.-J. Cheng *et al.*, 2024; Hu *et al.*, 2024; S. Lee *et al.*, 2024), whereas a bulk CDW is reported only in ScV_6Sn_6. As such, any potential Fermi-surface nesting is believed to only have a marginal effect on the CDW formation (S. Cheng *et al.*, 2024; S. Lee *et al.*, 2024; Yu *et al.*, 2024), and, instead, steric effects and dynamics associated with an inherent out-of-plane chain instability of the Sn-Sc-Sn-Sn ions drive its unconventional behavior. A real-space model of frustration of this chain instability, one whose in-plane correlations are frustrated via steric effects mediated via the kagome network, was shown to capture and quantitatively model the short-range $(1/3, 1/3, 1/2)$ charge correlations using a 2D Ising model (Alvarado *et al.*, 2024).

Supporting the notion of a primarily one-dimensional lattice instability, the CDW-like correlations in ScV_6Sn_6 are highly sensitive to disorder effects within the chains. Substituting Sc for larger R ions such as Lu or Y rapidly suppresses both long-range and short-range CDW order (Meier *et al.*, 2023; Pokharel *et al.*, 2023), which are attributed to the smallness of the Sc atoms compared to other possible R atoms (Tan and Yan, 2023) and the impact of Sn-ion rattling along the chain axis. Small amounts of substitution at the V site (Yi, Feng, Kumar *et al.*, 2024) or the use of high pressure (Y. Gu *et al.*, 2023; Yi, Feng, Kumar *et al.*, 2024) also suppress the CDW transition temperature. A strong coupling to lattice disorder is also reflected in the varied transition temperatures T^* reported of nominally stoichiometric crystals.

Of all the stoichiometric RV_6Sn_6 compounds studied thus far, only the Sc variant exhibits a bulk CDW phase. Theory suggests that some RV_6Sn_6 systems may exhibit surface charge orders ($\sqrt{3} \times \sqrt{3}$ or 2×2), even in the absence of a bulk CDW phase on kagome surface terminations (Tan and Yan, 2024). The $(1/3, 1/3)$ bulk, in-plane CDW wave vector is consistent with STM measurements of ScV_6Sn_6, which observe periodic $\sqrt{3} \times \sqrt{3}$ modulations rotated by 30° with respect to the atomic lattice (S. Cheng *et al.*, 2024; Jiang *et al.*, 2024; Kundu *et al.*, 2024); see Figs. 31(b) and 31(c). The out-of-plane periodicity was further resolved by imaging the charge order across different terraces (S. Cheng *et al.*, 2024; Kundu *et al.*, 2024). The CDW has, however, been observed only on some surface terminations (S. Cheng *et al.*, 2024; Jiang *et al.*, 2024), and there are conflicting reports in the literature reporting the presence (S. Cheng *et al.*, 2024; Kundu *et al.*, 2024) or absence (Jiang *et al.*, 2024) of charge order on the V termination. There are similarly dissonant reports on the honeycomb Sn_2 termination (S. Cheng *et al.*, 2024; Jiang *et al.*, 2024) and the triangular $Sn_1/ScSn_3$ termination (Jiang *et al.*, 2024; Kundu *et al.*, 2024). The multitude of inequivalent surface terminations possible in 166 systems (up to six different ones) complicate identification of surfaces imaged via STM.

STM experiments generally observe no spectral gap opening at E_f (Jiang *et al.*, 2024; Kundu *et al.*, 2024), albeit a small partial gap of about 20 meV has been reported in dI/dV spectra on one surface termination (S. Cheng *et al.*, 2024). Some ARPES (S. Lee *et al.*, 2024) and optical spectroscopy experiments (Kim, Liu *et al.*, 2023) suggest the largest gap opening occurs for $k_z \approx \pi$ along the A-L direction of 260–270 meV. STM dI/dV maps suggest the existence of another spectral gap at positive energies on the order of 50 meV based on charge modulations that exhibit an abrupt phase shift near that energy (S. Cheng *et al.*, 2024).

Beyond translation symmetry breaking induced by the CDW, additional rotational symmetries are reported to be broken in this system, potentially via a secondary instability of the V sublattice. Signatures of rotational symmetry breaking in the electronic structure are reported by STM experiments (Jiang *et al.*, 2024). First, spectroscopic-imaging STM detected a deformation of the low-energy electronic states on the V termination where the CDW signal is absent (Jiang *et al.*, 2024); see Fig. 31(d). Second, anisotropy in the intensity of atomic Bragg peaks in STM topographs is also observed on the same termination below about 70 K (Jiang *et al.*, 2024). No structural transition is observed in the temperature range, suggesting the electronic nature of electronic nematicity observed. No rotation symmetry breaking is detected in the intensities of the three in-plane CDW peaks (S. Cheng *et al.*, 2024; Jiang *et al.*, 2024), in sharp contrast to AV_3Sb_5 (Jiang *et al.*, 2021; Li, Zhao, Ortiz *et al.*, 2022). Electronic nematicity observed in ScV_6Sn_6 by STM is phenomenologically similar to that previously reported in $CsTi_3Bi_5$ (Li *et al.*, 2023a), where Fermi-surface deformation, anisotropic spectral weight and inequivalent atomic Bragg peaks have also been reported. It has been suggested that favorably positioned VHSs near the Fermi level play a role in the emergence of electronic nematicity in ScV_6Sn_6 (Jiang *et al.*, 2024).

Adding to these considerations, TRS is suggested to be broken below T^*. Here the enhancement of the internal field width within the CDW-like state sensed by the μSR spectroscopy suggests TRS breaking from "hidden" magnetism (Guguchia *et al.*, 2023a); see Fig. 31(e). Anomalous Hall-like behavior up to the CDW phase transition was also suggested to hint at TRS breaking (Mozaffari *et al.*, 2024; Yi, Feng, Mao *et al.*, 2024). We mention that ^{51}V NMR measurements have not observed any signatures of underlying magnetism, possibly because the signals are below the resolution of the experiment of $10^{-2}\mu_B$ (Guehne *et al.*, 2024), or due to nuclear fields and alternative fermiology effects accounting for the μSR and AHE results

e. RNb_6Sn_6 *compounds*

A new class of nonmagnetic M-site 166 variants was recently reported in RNb_6Sn_6, with $R = Y$, Ce, or Lu

(Ortiz *et al.*, 2025), with crystals grown via a high-temperature self-flux growth technique. These compounds also form a nonmagnetic Nb-based kagome net with K-point Dirac crossings at E_F and M-point saddle points nearly at and above E_F. A rich spectrum of magnetic states reported upon vary the R-site ion, where Gd, Tb, and Dy stabilize a variety of intermediate plateau states. $R = \mathrm{Lu}$ seemingly crosses the steric barrier necessary to stabilize an out-of-plane chain CDW-like instability in $LuNb_6Sn_6$. Below $T^* \approx 68$ K, transport, heat capacity, and magnetization record a transition into a lower symmetry $\bar{K}$-type distortion with $\mathbf{q} = (1/3, 1/3, 1/3)$. This is identical to the distortion observed in ScV_6Sn_6, and the distortion is frustrated with short-range charge correlations observed along $\mathbf{q} = (1/3, 1/3, 1/2)$, with phonon softening likely to occur along that wave vector as well.

f. $CsCr_6Sb_6$ *compounds*

Another member of the 166 family is the recently discovered $CsCr_6Sb_6$ (Liu *et al.*, 2025; Song *et al.*, 2025), which consists of Cr-based kagome networks and whose crystals can be grown via a high-temperature self-flux growth technique. ARPES and theoretical calculations reveal flat bands at the Fermi level that are composed of Cr $3d$ electrons (Song *et al.*, 2025). The material exhibits magnetic frustration and Kondo insulating behavior at low temperature, enabling the investigation of Kondo physics in kagome systems (Song *et al.*, 2025). As the thickness of the material is reduced to a few layers, its bulk magnetic frustration leads to A-type antiferromagnetic order and anomalous Hall response dependent on the parity of the number of layers (Song *et al.*, 2025).

4. AM_3X_4 compounds

AM_3X_4 compounds form with a formula unit where A can be either a trivalent or divalent rare-earth ion or a divalent alkali earth ion such as Ca. The M site can be nonmagnetic V or Ti with the anion X comprising Sb or Bi, respectively, and crystals are typically grown using high-temperature metal-flux methods (Ovchinnikov and Bobev, 2020; Ortiz *et al.*, 2023a, 2023b; Long Chen *et al.*, 2024). The structure is formed from units of buckled kagome bilayers that are spaced from one another via zigzag chains of the A-site ions in an orthorhombic cell. The magnetic A-site variants often form ferromagnetic ground states, though Ce, Gd, and Tb order antiferromagnetically in ATi_3Bi_4 (Motoyama *et al.*, 2018; Ortiz *et al.*, 2023a, 2024; K. Guo *et al.*, 2024). Low-field helical states may exist for the Eu^{2+} variants, and a number of magnetic plateau states have been reported in antiferromagnetic members when the field is oriented along the chain axis.

While band features reflective of the kagome networks such as flat bands, saddle points, and Dirac crossings have been identified in ARPES investigations of these compounds (Ortiz *et al.*, 2023a, 2023b; Sakhya *et al.*, 2024), electronic instabilities within the V kagome network are typically not observed. One notable exception is the recent STM report of a CDW intertwined with magnetic order in the $GdTi_3Bi_4$ compound (Han *et al.*, 2025a). Studies of this compound and related variants are ongoing.

5. Other compounds

a. A_2M_3X *compounds*

Another subset of kagome intermetallic compounds can be formed within ternary variants of three-dimensional Laves phases. $C14$ and $C15$ Laves phases have the chemical formula AM_2 where the M-site ions form kagome nets stacked with equidistant triangular lattice networks. The in-plane translational phasing between these stacked layers generates alternating face- and vertex-sharing tetrahedra in the $C14$ case and an extended pyrochlore network in the $C15$ case. By adding a third main group X ion that chemically orders within the triangular lattice network, an ordered ternary Laves phase can be formed, comprising chemically unique kagome layers, which are often distorted by a breathing mode. For example, the prototypical $C15$ Laves compound $MgCu_2$ forms a pyrochlore network of corner-sharing Cu tetrahedra. A third element such as Si can be incorporated to form Mg_2Cu_3Si, where Si occupies one tetrahedral Cu site in an ordered fashion. This results in planes of Cu kagome nets stacked with triangular nets of Si ions embedded within a lattice of Mg.

Many ordered Laves phases compounds are superconductors, for example, Mg_2Ir_3Si (Kudo, Hiiragi *et al.*, 2020) and Li_2IrSi_3 (Hirai *et al.*, 2014) with Ir- and Si-based kagome networks, respectively. The former can be grown in bulk crystal form via a high-temperature melt with excess Mg (Kudo, Hiiragi *et al.*, 2020). SC also appears when there is partial ordering of the kagome lattice (Kudo, Honda *et al.*, 2020), suggesting that it is not an instability derived exclusively from the kagome networks. Indeed, the electronic structure of ordered Laves phases remains three-dimensional, although a recent report of SC in Ta_2V_3Si discussed a connection between enhanced SC and the presence of kagome-derived VHS close to E_F (H. Liu *et al.*, 2023).

b. $RM_3(\mathrm{Si,B})_2$ *compounds*

A structurally distinct family of compounds with a chemical formula similar to ordered Laves phases are $RM_3(\mathrm{Si,B})_2$, where R is a lanthanide ion and M is a transition metal. These compounds possess distorted kagome nets of M-site ions separated by $M(\mathrm{Si,B})_2$ planes. The structure is distinct from the ordered Laves phase description, and the M-site kagome nets intersect with chains of R and $(\mathrm{Si,B})$ ions that thread the triangles and hexagons of the kagome network, respectively. A complicated interplay of magnetism and SC is realized across the phase diagrams of these materials (Barz, 1980; Ku *et al.*, 1980). SC occurs in a number of members of this materials class, with $LaRu_3Si_2$ the most widely studied owing to its higher T_c. There are a large number of compounds, so we focus on the $LaRu_3Si_2$ variant in this review as emblematic of the phenomena possible in these materials. Crystals can be obtained via standard melt-cool techniques (Mielke *et al.*, 2024).

$LaRu_3Si_2$ was reported to possess moderate electron-electron correlation effects via an enhanced Wilson ratio (Li *et al.*, 2011) with a conventional, nodeless BCS superconducting state (Kishimoto *et al.*, 2004) whose enhanced T_c is attributed to a narrow band of conduction elections. The narrow conduction band is proposed to arise from the proximity of a kagome-derived flatband close to E_F

(Mielke *et al.*, 2021), and correlation effects are further evident via a high-temperature charge-ordered phase that evolves upon cooling (Plokhikh *et al.*, 2024). Recently, Mielke *et al.* (2024) reported muon spin relaxation in μSR and magnetotransport data showing an unconventional coupling to external magnetic fields upon cooling into a modified CDW state. The impact of both the kagome-derived flat bands and the nearby saddle points on this phenomenology is a topic of current experimental (Chakrabortty, Kumar, and Mohapatra, 2023; Misawa *et al.*, 2025) and theoretical study (Deng *et al.*, 2025).

c. Homologous variants

The phase space for ternary kagome compounds is vast, and we highlight a few additional structural motifs here. For example, the AV_3Sb_5 structure exists within a broader, homologous family $(A_{m-1}Sb_{2m})(V_3Sb)_n$, where filled V_3Sb kagome planes are stacked with variable modulations of alkali and antimony layers. For instance, this generates AV_6Sb_6- and AV_8Sb_{12}-type structures with bilayer and higher groupings of the kagome planes (Q. Yin *et al.*, 2021; Mantravadi *et al.*, 2023). While the bilayer member of this family shows SC under high pressure (Shi *et al.*, 2022), no other member of this expanded family is reported to form CDW or SC order under ambient pressure.

Another kagome-related structure is the partially disordered $Ln_{2x}Ti_{6+x}Bi_9$ class of compounds (Ortiz *et al.*, 2024). The buckled Ti-based kagome layers partially connect out of the plane, and low-temperature magnetic transitions arising from the partial Ln-chain networks in the lattice have been reported. Another hybrid kagome structure is exemplified by $Yb_{0.5}Co_3Ge_3$. This compound possesses partially occupied Yb and Ge sublattices (Weiland *et al.*, 2020) and provides another example of the diversity of kagome structures possible. It exhibits a CDW-like low-temperature distortion of the kagome lattice as well as Yb-based magnetic order (Wang, McCandless *et al.*, 2022).

V. CONCLUSIONS

A. Summary

There has been tremendous progress in both experimental and theoretical aspects of kagome metals. Previously, existing (and often well-studied) materials were revisited using new theoretical frameworks, and new experimental probes were leveraged to test predictions of unconventional electronic states and phase behaviors in kagome compounds. This is readily apparent in the notable shift in the research focus from magnetic to electronic structure in numerous classes of magnetic kagome lattices. The notion of topological bands intrinsic to the band structure and the potential for combining these features with electronic correlations has become a topic of central focus.

From the perspective of materials, both binary and ternary kagome metals have grown into a broad and diverse class of exotic quantum materials. The binary systems have established the relevance of the kagome band structure in real materials, including Dirac crossings and flat bands, and sources of strong electronic correlation and have opened new opportunities for spintronic devices. The ternary systems, with the addition of a third element into the crystal structure, have brought an enhanced degree of chemical tunability and diversity, which in turn have provided a richer plethora of electronic properties and symmetry breaking than their binary kagome siblings.

In terms of experimentally observed phenomena, there have now been observations of the Dirac, Van Hove, and flat-band features that are expected for the kagome network. Positioning these features at the Fermi level has led to a variety of phenomena ranging from aspects of electronic topology to strong electronic correlations. For example, narrow-band-induced strange metal behavior has been observed in binary kagome metals, while electronic symmetry breaking tied to the presence of p-type Van Hove points has been observed in ternary systems. The interplay between these kagome-derived phase behaviors and other types of order and energy scales (for example, local moment magnetism and structural instabilities) in both ternary and binary compounds adds a layer of richness to the reported phenomena.

The theoretical investigation of kagome metals has also made significant progress and has offered a deep understanding of how their lattice geometry leads to a wide spectrum of electronic and collective phenomena. At the single-particle level, theoretical models of spinless electrons reveal the emergence of electronic features rooted in the kagome lattice's intrinsic symmetry and topology. The inclusion of SOC has further enriched this landscape, enabling the realization of topologically nontrivial phases. Lattice dynamics, treated through phonon calculations, highlights the importance of soft modes and structural instabilities, setting the stage for intertwined electron-phonon and many-body effects.

Building on this foundation, theoretical work to treat the interaction-driven phases that we have surveyed in this review has now advanced. Models of CDWs describe the nesting-driven instabilities supported by VHS, whereas mean-field and beyond-mean-field treatments have provided frameworks to understand unconventional SC, including signatures of PDWs. Treatments of electron-phonon coupling have shed light on its role in competing with electronic orders, and models incorporating local moment fluctuations and strong electron correlations have begun to describe the emergence of magnetism. Taken together, these developments not only provide solid theoretical foundations to the experimental discoveries in binary and ternary kagome metals but also suggest a rich and tunable platform for exploring novel quantum phases. In fact, understanding kagome metals means taking on the interacting electron problem in its entire complexity, treating electronic correlations and electron-phonon coupling on an equal footing. As such, kagome metals promise to play the role of an incubator and benchmark for understanding electronic quantum matter.

B. Future questions

Despite the rapid theoretical and experimental progress in understanding kagome metals, a wide array of open questions and challenges remain that demand further refinement and exploration. In terms of materials, much of the recent progress

in these systems has leveraged the use of metallic systems with a significant number of electronic bands. While this overcomes the challenge of introducing charge carriers previously encountered with chemical and electrostatic doping in insulating kagome systems, finding materials with simpler Fermi surfaces is of significant interest. In addition, finding compounds with more ideal *s*-electron orbitals, thereby better matching idealized models, is an open frontier. Many of the kagome systems to date are based on *d* electrons with multiple orbital states present at the Fermi level. Often, the bandwidth of the kagome band structure is broader than the energetic spacing within the *d*-electron manifold. Remedying this and finding systems with, for example, large crystal-field splittings and finding schemes where this would be possible with absent localization due to Coulomb interactions are open challenges. Finally, a broader range of effectively two-dimensional systems is a clear target.

Achieving such effectively two-dimensional kagome systems remains a crucial challenge for the field. Out-of-plane hopping strongly perturbs the ideal kagome band structure, thus reducing both the flat-band localization and the separation from non-kagome-derived states. To overcome this, several promising approaches could be pursued. The first approach involves van der Waals kagome metals, which are naturally prone to exfoliation and integration into atomically thin heterostructures. The second approach exploits thin-film growth and surface-engineering techniques, which enable the controlled realization of ultrathin kagome lattices or even artificial kagome layers. Both strategies open new opportunities for enhancing correlation effects, tuning topology, and engineering interactions in a manner not possible in bulk crystals.

Beyond these approaches, while it is now established that both correlated electronic phases and topological electronic phases can be realized in kagome materials, to what degree these two phenomena can enrich one another to create fundamentally new electronic phases is an open question. In addition, while the kagome network is now recognized as the chemically most common line-graph compound, to what extent other theoretically well-known line-graph lattices could be realized experimentally (and would also have the potential richness of kagome metals) is an emerging area of investigation.

From the theoretical side, one of the most pressing challenges lies in developing accurate minimal models that can faithfully capture the essential band features responsible for the emergence of CDW order, SC, nematicity, and TRS breaking in AV_3Sb_5 compounds. Theories must address the complex roles played by VHS, SOC, and multiorbital effects near the Fermi level, as well as the interplay between in-plane and out-of-plane Sb *p* orbitals, which remain poorly understood but are crucial to stabilizing correlated phases. The diversity of newly discovered AM_3X_5 materials, such as Ti-, Cr-, and V-based variants, further expands the parameter space of kagome systems, demonstrating the urgent need for theoretical tools that can adapt to different electronic fillings, orbital makeups, and structural distortions while remaining predictive and physically transparent.

Another frontier involves the theoretical treatment of strain and disorder. Experimental findings increasingly suggest a strong sensitivity of certain classes of kagome metals to mechanical strain, which appears to modulate TRS-breaking signatures and influence CDW domain formation. Theoretical models that incorporate the coupling of strain and structural deformation to electronic, magnetic, and orbital degrees of freedom are necessary for understanding emergent piezomagnetic responses and chirality switching observed in surface-sensitive probes. Such models will be fundamental for understanding whether the exotic signatures, such as Kerr rotation or nematic anisotropy, arise intrinsically or are mediated by strain-induced symmetry breaking.

A closely related challenge is uncovering the origins and consequences of intertwined orders. Kagome metals often exhibit similar energy scales for competing or coexisting states such as SC, charge order, magnetism and nematicity. Capturing the competition and entanglement of these orders, particularly in materials near Van Hove filling or in the presence of sizable correlations, will require beyond-mean-field approaches such as renormalization group methods, in which different electron orders compete toward the final ground state instability. Furthermore, the coupling of topology with magnetism, SC, and correlation effects presents another rich area for theoretical advancement. Several kagome metals present bands with a nontrivial topology, namely, Dirac cones, flat bands, and Weyl nodes, and their interplay with electronic correlations, electron-phonon interaction, and magnetism is still an underexplored direction.

The exploration of unconventional SC in kagome metals is equally promising and challenging. In fact, the pairing mechanisms leading to SC in systems like AV_3Sb_5, whether conventionally mediated by phonons or involving unconventional pairing channels, remain unresolved despite intense research activity. Resolving this puzzle requires studies that integrate realistic band structures with dynamical interactions. The field must also address the modeling of kagome materials with partial flat-band filling, which opens the door to strongly correlated quantum phases such as Mott insulators, non-Fermi liquid metals, and fractional Chern insulators. Here understanding how electronic interactions drive localization will be vital, especially in systems with minimal bandwidth and strong SOC.

Another important open question is to connect the conceptual viewpoints traditionally used for geometrically frustrated systems. Historically, frustrated lattices such as the kagome have been extensively explored within the context of Hubbard and spin models, often from the angle of strong correlations, Mott physics, and magnetic ground states. In contrast, much of the recent progress in kagome metals has been pushed by Fermi-liquid-based approaches that center on band structure instabilities, VHS, and weak-to-intermediate correlation effects. However, as evidence grows for strong-coupling phenomena, such as charge ordering, unconventional SC, and potential Mott-like behavior in certain regimes, it becomes important to investigate the link between these two approaches. This puts forward the necessity of theoretical frameworks that interpolate between weak-coupling Fermi liquid and nonperturbative many-body physics, particularly in systems with flat bands or partial band fillings. Developing a unified understanding that captures both itinerant and localized electron behavior in kagome systems will be fundamental for shedding light onto the full range of correlated phases that they can support.

Furthermore, an interesting question in kagome metals is the role of excitons and how they relate to charge and spin

orders. In multiband systems with strong SOC, particularly when TRS is broken, the distinctions among CDWs, SDWs, and exciton condensates become vague. Yet, most studies treat these orders separately. A more unified view that considers all these possibilities together could offer new insights into the nature of the symmetry-breaking phases in kagome materials.

Beyond their rich interplay of topology, correlation, and lattice frustration, kagome metals also offer a new and natural setting to explore the quantum geometry of Bloch states, which is captured by the quantum geometric tensor. Their flat bands, which arise from compact localized states, are classified as singular flat bands (Rhim and Yang, 2021). Under strong magnetic fields, these flat bands give rise to an anomalous Landau level spectrum that directly encodes the quantum metric (Rhim, Kim, and Yang, 2020), with predicted consequences such as diverging orbital magnetic susceptibility and nonlinear Hall effects. Building on these insights, recent work has proposed and demonstrated a photoemission-based approach to directly measure the quantum geometric tensor in kagome systems (Kang *et al.*, 2025), establishing them as a promising class of materials to experimentally probe band geometry and its role in topological and transport phenomena.

Last, kagome metals potentially represent an interesting platform for new device applications that could range from spintronics to orbitronics and quantum information. Investigations that link bulk properties to nanoscale or interface phenomena, such as proximity-induced SC, spin-orbit torque effects and charge-to-spin-to-orbit interconversion, will be important for future experimental efforts that aim at constructing functional kagome-based heterostructures and quantum devices. In this context the recent demonstration of a sizable modulation of the anomalous Hall angle in the magnetic Weyl semimetal $Co_3Sn_2S_2$ represents a significant advance. By achieving Hall angles far beyond those of conventional magnetic materials and realizing Fe-doped nanoflake devices with ultrahigh sensitivity and nanoscale magnetic field detectability, kagome metals are a highly promising platform for next-generation magnetic sensors and spintronic applications (J. Yang *et al.*, 2025).

In summary, while the study of kagome metals has already revealed a rich landscape of correlated and topological phenomena, the field remains full of open questions that span materials discovery, theoretical modeling, and emergent functionalities. The search for new kagome systems continues, and so too does the promise of discovering entirely new states of quantum matter, many of which may lie just beyond the current frontier.

LIST OF SYMBOLS AND ABBREVIATIONS

AFM	antiferromagnetism
AHE	anomalous Hall effect
ANE	anomalous Nernst effect
ARPES	angle-resolved photoemission spectroscopy
BCS	Bardeen-Cooper-Schrieffer
BZ	Brillouin zone
CDW	charge density wave
CL	circular left
CR	circular right
DFT	density functional theory
DMFT	dynamical mean-field theory
DOS	density of states
EBR	elementary band representation
EDC	energy distribution curve
MR	magnetoresistance
μSR	muon spin spectroscopy
PDW	pair density wave
PES	photoemission spectroscopy
PHE	planar Hall effect
QPI	quasiparticle interference
RPA	random phase approximation
SBC	spin-Berry curvature
SC	superconductivity
SDW	spin density wave
SOC	spin-orbit coupling
STM	scanning tunneling microscopy
TB	tight binding
TMO	transition-metal oxide
TMR	tunneling magnetoresistance
TRS	time-reversal symmetry
VHS	Van Hove singularity
XRD	x-ray diffraction

ACKNOWLEDGMENTS

We acknowledge Armando Consiglio, Matteo Dürrnagel, and Niklas Wagner for their help with the preparation of the manuscript as well as Brian M. Andersen, Ryotaro Arita, Morten H. Christensen, Rafael Fernandes, Mark H. Fischer, Julian Ingham, Dante Kennes, Federico Mazzola, Harley Scammell, Roser Valentí, Maia Vergniory, and Binghai Yan for the discussions and critical comments. D. D. S. acknowledges the Deutsche Forschungsgemeinschaft (DFG, German Research Foundation) through the SFB 1170 ToCoTronics Mercator Fellowship. R. T., G. S., and T. N. acknowledge support from the FOR 5249 (QUAST) project of the DFG and the associated funding from the Swiss National Science Foundation (Project No. 200021E198011). R. T., G. S, and D. D. S. acknowledge support from the DFG Cluster of Excellence ctd.qmat (Project No. 390858490). R. C., J. G. C., and S. D. W. were supported by the Air Force Office of Scientific Research under Grant No. FA9550-22-1-0432. I. Z. acknowledges the support from National Science Foundation (NSF), Division of Materials Research, Grant No. 2216080. T. N. acknowledges support from the Swiss National Science Foundation through a Consolidator Grant (iTQC, Grant No. TMCG-2213805).

REFERENCES

Agterberg, Daniel F., J. C. Samus Davis, Stephen D. Edkins, Eduardo Fradkin, Dale J. Van Harlingen, Steven A. Kivelson, Patrick A. Lee, Leo Radzihovsky, John M. Tranquada, and Yuxuan Wang, 2020, Annu. Rev. Condens. Matter Phys. **11**, 231.

Aichhorn, Markus, Silke Biermann, Takashi Miyake, Antoine Georges, and Masatoshi Imada, 2010, Phys. Rev. B **82**, 064504.

Alvarado, S. J. Gomez, G. Pokharel, B. R. Ortiz, Joseph A. M. Paddison, Suchismita Sarker, J. P. C. Ruff, and Stephen D. Wilson, 2024, Phys. Rev. B **110**, L140304.

Andrei, Eva Y., Dmitri K. Efetov, Pablo Jarillo-Herrero, Allan H. MacDonald, Kin Fai Mak, T. Senthil, Emanuel Tutuc, Ali Yazdani, and Andrea F. Young, 2021, Nat. Rev. Mater. **6**, 201.

Andrei, Eva Y., and Allan H. MacDonald, 2020, Nat. Mater. **19**, 1265.

Arachchige, Hasitha W. Suriya, William R. Meier, Madalynn Marshall, Takahiro Matsuoka, Rui Xue, Michael A. McGuire, Raphael P. Hermann, Huibo Cao, and David Mandrus, 2022, Phys. Rev. Lett. **129**, 216402.

Aretz, Joost, *et al.*, 2025, arXiv:2501.10320.

Aryasetiawan, F., 2011, in *The LDA+DMFT Approach to Strongly Correlated Materials*, Modeling and Simulation Vol. 1, edited by E. Pavarini, E. Koch, D. Vollhardt, and A. Lichtenstein (Verlag des Forschungszentrum Jülich, Jülich, Germany), ISBN: 978-3-89336-734-4.

Asaba, T., *et al.*, 2024, Nat. Phys. **20**, 40.

Avila, M. A., T. Takabatake, Y. Takahashi, S. L. Budko, and P. C. Canfield, 2005, J. Phys. Condens. Matter **17**, 6969.

Baranova, R. V., and Z. G. Pinsker, 1966, Sov. Phys. Crystallogr. **10**, 523.

Barz, H., 1980, Mater. Res. Bull. **15**, 1489.

Bauer, Bela, Lukasz Cincio, Brendan P. Keller, Michele Dolfi, Guifre Vidal, Simon Trebst, and Andreas W. W. Ludwig, 2014, Nat. Commun. **5**, 5137.

Bergman, Doron L., Congjun Wu, and Leon Balents, 2008, Phys. Rev. B **78**, 125104.

Bernevig, B. Andrei, and Dmitri K. Efetov, 2024, Phys. Today **77**, No. 4, 38.

Bigi, Chiara, *et al.*, 2026, Nat. Commun. **17**, 325.

Biswas, A., O. Iakutkina, Q. Wang, H. C. Lei, M. Dressel, and E. Uykur, 2020, Phys. Rev. Lett. **125**, 076403.

Bonetti, Pietro M., Yi Jiang, Haoyu Hu, Dumitru Călugăru, Michael M. Scherer, B. Andrei Bernevig, and Laura Classen, 2024, arXiv:2411.10931.

Bouaziz, Juba, Takuya Nomoto, and Ryotaro Arita, 2025, Phys. Rev. B **112**, 014406.

Bradlyn, Barry, Luis Elcoro, Jennifer Cano, Maia G. Vergniory, Zhijun Wang, Claudia Felser, Mois I. Aroyo, and B. Andrei Bernevig, 2017, Nature (London) **547**, 298.

Buiarelli, Luca, Turan Birol, Brian M. Andersen, and Morten H. Christensen, 2025, arXiv:2507.23329.

Bulla, R., and M. Potthoff, 2000, Eur. Phys. J. B **13**, 257.

Cadogan, J. M., Suharyana, D. H. Ryan, O. Moze, and W. Kockelmann, 2000, J. Appl. Phys. **87**, 6046.

Candelora, Christopher, Hong Li, Muxian Xu, Brenden R. Ortiz, Andrea Capa Salinas, Siyu Cheng, Alexander LaFleur, Ziqiang Wang, Stephen D. Wilson, and Ilija Zeljkovic, 2024, Phys. Rev. B **109**, 155121.

Candelora, Christopher, and Ilija Zeljkovic, 2025, arXiv:2509.22634.

Cano, Jennifer, Barry Bradlyn, Zhijun Wang, Luis Elcoro, Maia Garcia Vergniory, Claudia Felser, Mois I. Aroyo, and B. Andrei Bernevig, 2018, Phys. Rev. B **97**, 035139.

Cao, Liye, Xiangqi Liu, Jiayi Cheng, Bixia Gao, Xiaoting Zhang, Yanfeng Guo, Fengjie Ma, and Rongyan Chen, 2025, Phys. Rev. B **111**, 075147.

Cao, Saizheng, Chenchao Xu, Hiroshi Fukui, Taishun Manjo, Ying Dong, Ming Shi, Yang Liu, Chao Cao, and Yu Song, 2023, Nat. Commun. **14**, 7671.

Cao, Yuan, Valla Fatemi, Shiang Fang, Kenji Watanabe, Takashi Taniguchi, Efthimios Kaxiras, and Pablo Jarillo-Herrero, 2018, Nature (London) **556**, 43.

Capa Salinas, Andrea N., Brenden R. Ortiz, Calvin Bales, Jonathan Frassineti, Vesna F. Mitrović, and Stephen D. Wilson, 2023, Front. Electron. Mater. **3**, 1257490.

Chakrabortty, S., Ram Kumar, and N. Mohapatra, 2023, Phys. Rev. B **107**, 024503.

Chatzieleftheriou, Maria, Jonas B. Profe, Ying Li, and Roser Valentí, 2026, arXiv:2601.14439.

Che, Mengqian, *et al.*, 2025, Phys. Rev. Lett. **134**, 196906.

Checkelsky, Joseph G., B. Andrei Bernevig, Piers Coleman, Qimiao Si, and Silke Paschen, 2024, Nat. Rev. Mater. **9**, 509.

Chen, Caiyun, Jiangchang Zheng, Ruopeng Yu, Soumya Sankar, Kam Tuen Law, Hoi Chun Po, and Berthold Jäck, 2023, Phys. Rev. Res. **5**, 043269.

Chen, Dong, Bin He, Mengyu Yao, Yu Pan, Haicheng Lin, Walter Schnelle, Yan Sun, Johannes Gooth, Louis Taillefer, and Claudia Felser, 2022, Phys. Rev. B **105**, L201109.

Chen, Hao, Weikang Wu, Shengyuan A. Yang, Xiao Li, and Lifa Zhang, 2019, Phys. Rev. B **100**, 094303.

Chen, Hui, Hussein Nassar, Andrew N. Norris, G. K. Hu, and G. L. Huang, 2018, Phys. Rev. B **98**, 094302.

Chen, Hui, *et al.*, 2021, Nature (London) **599**, 222.

Chen, K. Y., *et al.*, 2021, Phys. Rev. Lett. **126**, 247001.

Chen, Lebing, *et al.*, 2024, Nat. Commun. **15**, 1918.

Chen, Long, *et al.*, 2024, Commun. Mater. **5**, 73.

Chen, Q., D. Chen, W. Schnelle, C. Felser, and B. D. Gaulin, 2022, Phys. Rev. Lett. **129**, 056401.

Chen, Taishi, *et al.*, 2022, Sci. Adv. **8**, eabk1480.

Chen, Xianzhe, *et al.*, 2023, Nature (London) **613**, 490.

Chen, Xintong, *et al.*, 2023, Phys. Rev. B **107**, 174510.

Chen, Ziyuan, *et al.*, 2024, Nat. Commun. **15**, 6262.

Cheng, Shuyu, Binbin Wang, Igor Lyalin, Núria Bagués, Alexander J. Bishop, David W. McComb, and Roland K. Kawakami, 2022, APL Mater. **10**, 061112.

Cheng, Shuyu, *et al.*, 2023, Nano Lett. **23**, 7107.

Cheng, Siyu, Keyu Zeng, Yi Liu, Christopher Candelora, Ziqiang Wang, Guang-Han Cao, and Ilija Zeljkovic, 2025, arXiv:2510.06168.

Cheng, Siyu, *et al.*, 2024, npj Quantum Mater. **9**, 14.

Cheng, Zi-Jia, *et al.*, 2024, Phys. Rev. B **109**, 075150.

Chiu, Christie S., Annette N. Carroll, Nicolas Regnault, and Andrew A. Houck, 2022, Phys. Rev. Res. **4**, 023063.

Cho, Soohyun, *et al.*, 2021, Phys. Rev. Lett. **127**, 236401.

Christensen, Morten H., Turan Birol, Brian M. Andersen, and Rafael M. Fernandes, 2021, Phys. Rev. B **104**, 214513.

Christensen, Morten H., Turan Birol, Brian M. Andersen, and Rafael M. Fernandes, 2022, Phys. Rev. B **106**, 144504.

Claassen, Martin, Lede Xian, Dante M. Kennes, and Angel Rubio, 2022, Nat. Commun. **13**, 4915.

Clatterbuck, D. M., and K. A. Gschneidner, Jr., 1999, J. Magn. Magn. Mater. **207**, 78.

Consiglio, Armando, Tilman Schwemmer, Xianxin Wu, Werner Hanke, Titus Neupert, Ronny Thomale, Giorgio Sangiovanni, and Domenico Di Sante, 2022, Phys. Rev. B **105**, 165146.

Conte, Felice, Domenico Ninno, and Giovanni Cantele, 2020, Phys. Rev. Res. **2**, 033001.

Corps, Jack, Paz Vaqueiro, Alex Aziz, Ricardo Grau-Crespo, Winfried Kockelmann, Jean-Claude Jumas, and Anthony V. Powell, 2015, Chem. Mater. **27**, 3946.

Crispino, Matteo, Niklas Witt, Stefan Enzner, Tommaso Gorni, Luca de' Medici, Domenico Di Sante, and Giorgio Sangiovanni, 2025, arXiv:2512.22576.

Cvetkovic, Dragoš, Peter Rowlinson, and Slobodan Simic, 2004, *Spectral Generalizations of Line Graphs: On Graphs with Least Eigenvalue-2* (Cambridge University Press, Cambridge, England).
Dai, P., J. Hu, and E. Dagotto, 2012, Nat. Phys. **8**, 709.
Dai, Yi, Andreas Kreisel, and Brian M. Andersen, 2024, Phys. Rev. B **110**, 144516.
de' Medici, Luca, Jernej Mravlje, and Antoine Georges, 2011, Phys. Rev. Lett. **107**, 256401.
Deng, Hanbin, *et al.*, 2024a, Nat. Mater. **23**, 1639.
Deng, Hanbin, *et al.*, 2024b, Nature (London) **632**, 775.
Deng, Junze, Ruihan Zhang, Yue Xie, Xianxin Wu, and Zhijun Wang, 2023, Phys. Rev. B **108**, 115123.
Deng, Junze, *et al.*, 2025, arXiv:2503.20867.
Deng, Yongcheng, Xionghua Liu, Yiyuan Chen, Zongzheng Du, Nai Jiang, Chao Shen, Enze Zhang, Houzhi Zheng, Hai-Zhou Lu, and Kaiyou Wang, 2023, Natl. Sci. Rev. **10**, nwac154.
Denner, M. Michael, Ronny Thomale, and Titus Neupert, 2021, Phys. Rev. Lett. **127**, 217601.
DeStefano, Jonathan M., Elliott Rosenberg, Olivia Peek, Yongbin Lee, Zhaoyu Liu, Qianni Jiang, Liqin Ke, and Jiun-Haw Chu, 2023, npj Quantum Mater. **8**, 65.
Devakul, Trithep, Valentin Crépel, Yang Zhang, and Liang Fu, 2021, Nat. Commun. **12**, 6730.
Dhakal, Gyanendra, *et al.*, 2021, Phys. Rev. B **104**, L161115.
Dhital, C., G. Pokharel, B. Wilson, I. Kendrick, M. M. Asmar, D. Graf, J. Guerrero-Sanchez, R. Gonzalez-Hernandez, and S. D. Wilson, 2024, Phys. Rev. B **109**, 235145.
Ding, Gaofeng, Hongliang Wo, Yiqing Gu, Yimeng Gu, and Jun Zhao, 2022, Phys. Rev. B **106**, 235151.
Di Sante, Domenico, Johanna Erdmenger, Martin Greiter, Ioannis Matthaiakakis, René Meyer, David Rodríguez Fernández, Ronny Thomale, Erik van Loon, and Tim Wehling, 2020, Nat. Commun. **11**, 3997.
Di Sante, Domenico, Bongjae Kim, Werner Hanke, Tim Wehling, Cesare Franchini, Ronny Thomale, and Giorgio Sangiovanni, 2023, Phys. Rev. Res. **5**, L012008.
Di Sante, Domenico, *et al.*, 2023, Nat. Phys. **19**, 1135.
Do, Seung-Hwan, *et al.*, 2022, Phys. Rev. B **105**, L180403.
Dong, Zixian, Lei Shi, Bin Wang, Mengwu Huo, Xing Huang, Chaoxin Huang, Peiyue Ma, Yunwei Zhang, Bing Shen, and Meng Wang, 2024, Chin. Phys. B **33**, 107102.
Drucker, Nathan, *et al.*, 2024, arXiv:2401.17141.
Du, Feng, Shuaishuai Luo, Brenden R. Ortiz, Ye Chen, Weiyin Duan, Dongting Zhang, Xin Lu, Stephen D. Wilson, Yu Song, and Huiqiu Yuan, 2021, Phys. Rev. B **103**, L220504.
Du, Qianheng, Zhixiang Hu, Myung-Geun Han, Fernando Camino, Yimei Zhu, and C. Petrovic, 2022, Phys. Rev. Lett. **129**, 236601.
Du, Zengyi, Hui Li, Sang Hyun Joo, Elizabeth P. Donoway, Jinho Lee, J. C. Séamus Davis, Genda Gu, Peter D. Johnson, and Kazuhiro Fujita, 2020, Nature (London) **580**, 65.
Duan, Weiyin, *et al.*, 2021, Sci. China Phys. Mech. Astron. **64**, 107462.
Ebad-Allah, J., *et al.*, 2024, Phys. Rev. B **109**, L201106.
Ekahana, Sandy Adhitia, *et al.*, 2024, Nature (London) **627**, 67.
Elcoro, Luis, Benjamin J. Wieder, Zhida Song, Yuanfeng Xu, Barry Bradlyn, and B. Andrei Bernevig, 2021, Nat. Commun. **12**, 5965.
El Idrissi, B. Chafik, G. Venturini, and B. Malaman, 1991, Mater. Res. Bull. **26**, 1331.
El Idrissi, B. Chafik, G. Venturini, B. Malaman, and D. Fruchart, 1991, J. Less-Common Met. **175**, 143.
Engelsberg, Schrieffer, and J. R. Schrieffer, 1963, Phys. Rev. **131**, 993.
Enzner, Stefan, Jan Berges, Arne Schobert, Dongjin Oh, Mingu Kang, Riccardo Comin, Ronny Thomale, Tim O. Wehling, Domenico Di Sante, and Giorgio Sangiovanni, 2025, arXiv:2504.07883.
Fang, Hongwei, *et al.*, 2023, Sci. China Mater. **66**, 2032.
Fang, Yuqiang, Xin Feng, Dong Wang, Yang Ding, Tianquan Lin, Tianyou Zhai, and Fuqiang Huang, 2023, Small **19**, 2207934.
Feng, Li, Xiaofang Chen, and Jingshan Qi, 2023, Phys. Rev. B **108**, 115407.
Fenner, L. A., A. A. Dee, and A. S. Wills, 2009, J. Phys. Condens. Matter **21**, 452202.
Fernandes, Rafael M., Turan Birol, Mengxing Ye, and David Vanderbilt, 2025, arXiv:2502.16657.
Ferrari, Francesco, Federico Becca, and Roser Valentí, 2022, Phys. Rev. B **106**, L081107.
Forsyth, J. B., C. Wilkinson, and P. Gardner, 1978, J. Phys. F **8**, 2195.
Fu, Liang, and C. L. Kane, 2008, Phys. Rev. Lett. **100**, 096407.
Fu, Liang, Charles L. Kane, and Eugene J. Mele, 2007, Phys. Rev. Lett. **98**, 106803.
Fu, Yang, *et al.*, 2021, Phys. Rev. Lett. **127**, 207002.
Fulde, Peter, and Richard A. Ferrell, 1964, Phys. Rev. **135**, A550.
Gao, Hong-Jun, *et al.*, 2023, 10.21203/rs.3.rs-2774220/v1.
Gao, Shunye, *et al.*, 2023, Phys. Rev. X **13**, 041049.
Garmroudi, Fabian, Michael Parzer, Alexander Riss, Cédric Bourgès, Sergii Khmelevskyi, Takao Mori, Ernst Bauer, and Andrej Pustogow, 2023, Sci. Adv. **9**, eadj1611.
Garmroudi, Fabian *et al.*, 2024, arXiv:2404.08067.
Ge, Jun, Pinyuan Wang, Ying Xing, Qiangwei Yin, Anqi Wang, Jie Shen, Hechang Lei, Ziqiang Wang, and Jian Wang, 2024, Phys. Rev. X **14**, 021025.
Georges, A., and G. Kotliar, 2024, Phys. Today **77**, No. 4, 46.
Georges, A., Luca de' Medici, and J. Mravlje, 2013, Annu. Rev. Condens. Matter Phys. **4**, 137.
Georges, Antoine, 2004, in *Lectures on the Physics of Highly Correlated Electron Systems VIII*, edited by Adolfo Avella and Ferdinando Mancini, AIP Conf. Proc. Vol. 715 (AIP, New York), pp. 3–74.
Ghimire, Nirmal J., *et al.*, 2020, Sci. Adv. **6**, eabe2680.
Gim, Dong-Hyeon, Dirk Wulferding, Chulwan Lee, Hengbo Cui, Kiwan Nam, Myung Joon Han, and Kee Hoon Kim, 2023, Phys. Rev. B **108**, 115143.
Grandi, Francesco, Armando Consiglio, Michael A. Sentef, Ronny Thomale, and Dante M. Kennes, 2023, Phys. Rev. B **107**, 155131.
Grant, Morgan J., Yi Liu, Guang-Han Cao, Joseph A. Wilcox, Yanfeng Guo, Xiaofeng Xu, and Antony Carrington, 2025, J. Phys. Condens. Matter **37**, 065601.
Grosso, Giuseppe, and Giuseppe Pastori Parravicini, 2013, *Solid State Physics* (Academic Press, New York).
Grytsiuk, Sergii, Mikhail I. Katsnelson, Erik G. C. P. van Loon, and Malte Rösner, 2024, npj Quantum Mater. **9**, 8.
Gu, Qiangqiang, *et al.*, 2023, Nature (London) **618**, 921.
Gu, Yanhong, Ethan T. Ritz, William R. Meier, Avery Blockmon, Kevin Smith, Richa Pokharel Madhogaria, Shirin Mozaffari, David Mandrus, Turan Birol, and Janice L. Musfeldt, 2023, npj Quantum Mater. **8**, 58.
Guehne, Robin, Jonathan Noky, Changjiang Yi, Chandra Shekhar, Maia G. Vergniory, Michael Baenitz, and Claudia Felser, 2024, Nat. Commun. **15**, 8213.
Guguchia, Z., *et al.*, 2023a, Nat. Commun. **14**, 7796.
Guguchia, Z., *et al.*, 2023b, Nat. Commun. **14**, 153.
Gui, Hengrui, *et al.*, 2025, Nat. Commun. **16**, 4275.
Guo, Chunyu, *et al.*, 2022, Nature (London) **611**, 461.
Guo, Chunyu, *et al.*, 2024, Nat. Phys. **20**, 579.
Guo, Chunyu, *et al.*, 2025, Nature (London) **647**, 68.

Guo, H.-M., and M. Franz, 2009, Phys. Rev. B **80**, 113102.
Guo, Kaizhen, Zeyu Ma, Hongxiong Liu, Ziyang Wu, Junfeng Wang, Youguo Shi, Yuan Li, and Shuang Jia, 2024, Phys. Rev. B **110**, 064416.
Guo, Kaizhen, Junyao Ye, Shuyue Guan, and Shuang Jia, 2023, Phys. Rev. B **107**, 205151.
Guo, Yucheng, *et al.*, 2024, arXiv:2406.05293.
Gupta, Ritu, *et al.*, 2022, npj Quantum Mater. **7**, 49.
Guterding, Daniel, Harald O. Jeschke, and Roser Valentí, 2016, Sci. Rep. **6**, 25988.
Häggström, L., T. Ericsson, R. Wäppling, and K. Chandra, 1975, Phys. Scr. **11**, 47.
Haldane, F. Duncan M., 1988, Phys. Rev. Lett. **61**, 2015.
Han, Minyong, Caolan John, Jingxu Zheng, Shiang Fang, and Joseph G. Checkelsky, 2024, Phys. Rev. B **109**, L121112.
Han, Shulun, *et al.*, 2023, Adv. Mater. **35**, 2209010.
Han, Xianghe, *et al.*, 2025a, arXiv:2503.05545.
Han, Xianghe, *et al.*, 2025b, Nat. Nanotechnol. **20**, 1017.
Hansmann, P., R. Arita, A. Toschi, S. Sakai, G. Sangiovanni, and K. Held, 2010, Phys. Rev. Lett. **104**, 197002.
Haraguchi, Yuya, Chishiro Michioka, Manabu Ishikawa, Yoshiaki Nakano, Hideki Yamochi, Hiroaki Ueda, and Kazuyoshi Yoshimura, 2017, Inorg. Chem. **56**, 3483.
Haule, K., and G. Kotliar, 2009, New J. Phys. **11**, 025021.
Hausoel, A., M. Karolak, E. Şaşıoğlu, A. Lichtenstein, K. Held, A. Katanin, A. Toschi, and G. Sangiovanni, 2017, Nat. Commun. **8**, 16062.
He, Miao, Xitong Xu, Ding Li, Qingqi Zeng, Yonglai Liu, Haitian Zhao, Shiming Zhou, Jianhui Zhou, and Zhe Qu, 2024, Phys. Rev. B **109**, 155117.
He, Yin-Chen, Michael P. Zaletel, Masaki Oshikawa, and Frank Pollmann, 2017, Phys. Rev. X **7**, 031020.
Hengsberger, M., R. Frésard, D. Purdie, P. Segovia, and Y. Baer, 1999, Phys. Rev. B **60**, 10796.
Higo, Tomoya, and Satoru Nakatsuji, 2022, J. Magn. Magn. Mater. **564**, 170176.
Higo, Tomoya, *et al.*, 2022, Nature (London) **607**, 474.
Hirai, Daigorou, Rui Kawakami, Oxana V. Magdysyuk, Robert E. Dinnebier, Alexander Yaresko, and Hidenori Takagi, 2014, J. Phys. Soc. Jpn. **83**, 103703.
Holbæk, Sofie Castro, Morten H. Christensen, Andreas Kreisel, and Brian M. Andersen, 2023, Phys. Rev. B **108**, 144508.
Holbæk, Sofie Castro, and Mark H. Fischer, 2025, Phys. Rev. Res. **7**, 023129.
Holder, M., Yu. S. Dedkov, A. Kade, H. Rosner, W. Schnelle, A. Leithe-Jasper, R. Weihrich, and S. L. Molodtsov, 2009, Phys. Rev. B **79**, 205116.
Hossain, Md Shafayat, *et al.*, 2025, Nat. Phys. **21**, 556.
Hou, Zhipeng, *et al.*, 2017, Adv. Mater. **29**, 1701144.
Howlader, Sandeep, Ranjani Ramachandran, Shama, Yogesh Singh, and Goutam Sheet, 2021, J. Phys. Condens. Matter **33**, 075801.
Hu, Haoyu, Yi Jiang, and Dumitru Călugăru, Xiaolong Feng, David Subires, Maia G. Vergniory, Claudia Felser, Santiago Blanco-Canosa, and B. Andrei Bernevig, 2025, Phys. Rev. B **111**, 054113.
Hu, Tianchen, *et al.*, 2023, Phys. Rev. B **107**, 165119.
Hu, Yong, Congcong Le, Xianxin Wu, and Ming Shi, 2024, Supercond. Sci. Technol. **37**, 123004.
Hu, Yong, Xianxin Wu, Andreas P. Schnyder, and Ming Shi, 2023, npj Quantum Mater. **8**, 67.
Hu, Yong, Xianxin Wu, Yongqi Yang, Shunye Gao, Nicholas C. Plumb, Andreas P. Schnyder, Weiwei Xie, Junzhang Ma, and Ming Shi, 2022, Sci. Adv. **8**, eadd2024.
Hu, Yong, *et al.*, 2022a, Sci. Bull. **67**, 495.
Hu, Yong, *et al.*, 2022b, Nat. Commun. **13**, 2220.
Hu, Yong, *et al.*, 2023, Nat. Phys. **19**, 1827.
Hu, Yong, *et al.*, 2024, Nat. Commun. **15**, 1658.
Huai, Linwei, *et al.*, 2022, Chin. Phys. B **31**, 057403.
Huang, Hao, *et al.*, 2022, Phys. Rev. Lett. **128**, 096601.
Huang, Jiale, *et al.*, 2023, Phys. Rev. B **108**, 184431.
Huang, Xing, *et al.*, 2023, Phys. Rev. Mater. **7**, 054403.
Huang, Zihao, *et al.*, 2025, arXiv:2510.05018.
Huber, Sebastian D., 2016, Nat. Phys. **12**, 621.
Ikhlas, Muhammad, Takahiro Tomita, Takashi Koretsune, Michi-To Suzuki, Daisuke Nishio-Hamane, Ryotaro Arita, Yoshichika Otani, and Satoru Nakatsuji, 2017, Nat. Phys. **13**, 1085.
Imada, Masatoshi, Atsushi Fujimori, and Yoshinori Tokura, 1998, Rev. Mod. Phys. **70**, 1039.
Imhof, Stefan, *et al.*, 2018, Nat. Phys. **14**, 925.
Inoue, Hisashi, Minyong Han, Linda Ye, Takehito Suzuki, and Joseph G. Checkelsky, 2019, Appl. Phys. Lett. **115**, 072403.
Iqbal, Yasir, Federico Becca, Sandro Sorella, and Didier Poilblanc, 2013, Phys. Rev. B **87**, 060405.
Ishii, Yui, Hisatomo Harima, Yoshihiko Okamoto, Jun-ichi Yamaura, and Zenji Hiroi, 2013, J. Phys. Soc. Jpn. **82**, 023705.
Jeff, Dylan A., *et al.*, 2023, 2D Mater. **10**, 045030.
Jeong, Min Yong, Hyeok-Jun Yang, Hee Seung Kim, Yong Baek Kim, SungBin Lee, and Myung Joon Han, 2022, Phys. Rev. B **105**, 235145.
Jia, Liangguang, *et al.*, 2024, Nano Lett. **24**, 8843.
Jiang, Kun, Tao Wu, Jia-Xin Yin, Zhenyu Wang, M. Zahid Hasan, Stephen D. Wilson, Xianhui Chen, and Jiangping Hu, 2023, Natl. Sci. Rev. **10**, nwac199.
Jiang, Yi, Haoyu Hu, Dumitru Călugăru, Claudia Felser, Santiago Blanco-Canosa, Hongming Weng, Yuanfeng Xu, and B. Andrei Bernevig, 2025, Phys. Rev. B **111**, 125163.
Jiang, Yu-Xiao, *et al.*, 2021, Nat. Mater. **20**, 1353.
Jiang, Yu-Xiao, *et al.*, 2024, Nat. Mater. **23**, 1214.
Jiang, Zhicheng, *et al.*, 2023a, Nat. Commun. **14**, 4892.
Jiang, Zhicheng, *et al.*, 2023b, Nano Lett. **23**, 5625.
Jo, Gyu-Boong, Jennie Guzman, Claire K. Thomas, Pavan Hosur, Ashvin Vishwanath, and Dan M. Stamper-Kurn, 2012, Phys. Rev. Lett. **108**, 045305.
Jones, D. Connor, Suvadip Das, Hari Bhandari, Xiaoxiong Liu, Peter Siegfried, Madhav P. Ghimire, Stepan S. Tsirkin, I. I. Mazin, and Nirmal J. Ghimire, 2024, Phys. Rev. B **110**, 115134.
Kaczmarek, Austin, Andrea Capa Salinas, Stephen D. Wilson, and Katja C. Nowack, 2024, arXiv:2412.19919.
Kagan, Yu, and L. A. Maksimov, 2008, Phys. Rev. Lett. **100**, 145902.
Kane, Charles L., and Tom C. Lubensky, 2014, Nat. Phys. **10**, 39.
Kane, Charles L., and Eugene J. Mele, 2005a, Phys. Rev. Lett. **95**, 146802.
Kane, Charles L., and Eugene J. Mele, 2005b, Phys. Rev. Lett. **95**, 226801.
Kang, Mingu, *et al.*, 2020a, Nat. Commun. **11**, 4004.
Kang, Mingu, *et al.*, 2020b, Nat. Mater. **19**, 163.
Kang, Mingu, *et al.*, 2022, Nat. Phys. **18**, 301.
Kang, Mingu, *et al.*, 2023, Nat. Mater. **22**, 186.
Kang, Mingu, *et al.*, 2025, Nat. Phys. **21**, 110.
Karmakar, Roy, Abhirup, S. Nandy, A. Taraphder, and G. P. Das, 2022, Phys. Rev. B **106**, 245133.
Kato, Takemi, Yongkai Li, Kosuke Nakayama, Zhiwei Wang, Seigo Souma, Miho Kitamura, Koji Horiba, Hiroshi Kumigashira, Takashi Takahashi, and Takafumi Sato, 2022, Phys. Rev. B **106**, L121112.
Kato, Takemi, *et al.*, 2022, Phys. Rev. Lett. **129**, 206402.
Kato, Takemi, *et al.*, 2023, Phys. Rev. B **107**, 245143.

Kautzsch, Linus, Brenden R. Ortiz, Krishnanand Mallayya, Jayden Plumb, Ganesh Pokharel, Jacob P. C. Ruff, Zahirul Islam, Eun-Ah Kim, Ram Seshadri, and Stephen D. Wilson, 2023, Phys. Rev. Mater. **7**, 024806.
Kautzsch, Linus, *et al.*, 2023, npj Quantum Mater. **8**, 37.
Kelly, Z. A., M. J. Gallagher, and T. M. McQueen, 2016, Phys. Rev. X **6**, 041007.
Kennes, Dante M., Martin Claassen, Lede Xian, Antoine Georges, Andrew J. Millis, James Hone, Cory R. Dean, D. N. Basov, Abhay N. Pasupathy, and Angel Rubio, 2021, Nat. Phys. **17**, 155.
Kenney, Eric M., Brenden R. Ortiz, Chennan Wang, Stephen D. Wilson, and Michael J. Graf, 2021, J. Phys. Condens. Matter **33**, 235801.
Khan, Kacho Imtiyaz Ali, Ram Singh Yadav, Himanshu Bangar, Akash Kumar, Niru Chowdhury, Prasanta Kumar Muduli, and Pranaba Kishor Muduli, 2022, Nanoscale **14**, 8484.
Khasanov, Rustem, *et al.*, 2022, Phys. Rev. Res. **4**, 023244.
Kida, T., L. A. Fenner, A. A. Dee, I. Terasaki, M. Hagiwara, and A. S. Wills, 2011, J. Phys. Condens. Matter **23**, 112205.
Kiesel, Maximilian L., Christian Platt, and Ronny Thomale, 2013, Phys. Rev. Lett. **110**, 126405.
Kiesel, Maximilian L., and Ronny Thomale, 2012, Phys. Rev. B **86**, 121105.
Kim, D. W., Shuyuan Liu, Chongze Wang, H. W. Nam, G. Pokharel, Stephen D. Wilson, Jun-Hyung Cho, and S. J. Moon, 2023, Phys. Rev. B **108**, 205118.
Kim, Dongwook, and Feng Liu, 2023, Phys. Rev. B **107**, 205130.
Kim, Jangwon, Youjin Lee, Young Woo Choi, Taek Sun Jung, Suhan Son, Jonghyeon Kim, Hyoung Joon Choi, Je-Geun Park, and Jae Hoon Kim, 2023, ACS Omega **8**, 14190.
Kimata, Motoi, *et al.*, 2019, Nature (London) **565**, 627.
Kishimoto, Yutaka, Yu Kawasaki, Takashi Ohno, Laxmi C. Gupta, and Goutam Ghosh, 2004, J. Magn. Magn. Mater. **272–276**, 507.
Kiyohara, Naoki, Takahiro Tomita, and Satoru Nakatsuji, 2016, Phys. Rev. Appl. **5**, 064009.
Klemm, Mason L., *et al.*, 2025, Nat. Commun. **16**, 3313.
Kolli, Sanjeev Krishna, Anirudh Raju Natarajan, and Anton Van der Ven, 2021, Acta Mater. **221**, 117429.
Korshunov, A., *et al.*, 2023, Nat. Commun. **14**, 6646.
Korshunov, A., *et al.*, 2024, arXiv:2409.04325.
Koshelev, A. E., R. Chapai, D. Y. Chung, J. F. Mitchell, and U. Welp, 2024, Phys. Rev. B **110**, 024512.
Krén, E., J. Paitz, G. Zimmer, and É. Zsoldos, 1975, Physica (Amsterdam) **80B+C**, 226.
Ku, H. C., G. P. Meisner, F. Acker, and D. C. Johnston, 1980, Solid State Commun. **35**, 91.
Kübler, Jürgen, and Claudia Felser, 2014, Europhys. Lett. **108**, 67001.
Kudo, Kazutaka, Hikaru Hiiragi, Toshiaki Honda, Kazunori Fujimura, Hiroyuki Idei, and Minoru Nohara, 2020, J. Phys. Soc. Jpn. **89**, 013701.
Kudo, Kazutaka, Toshiaki Honda, Hikaru Hiiragi, Hiromi Ota, and Minoru Nohara, 2020, J. Phys. Soc. Jpn. **89**, 123701.
Kulshreshtha, S. K., and P. Raj, 1981, J. Phys. F **11**, 281.
Kundu, Asish K., *et al.*, 2024, Nat. Commun. **15**, 5008.
Kuroda, K., *et al.*, 2017, Nat. Mater. **16**, 1090.
L, Nil, Thais Victa Trevisan, and R. J. McQueeney, 2025, Phys. Rev. B **111**, 054410.
LaBollita, Harrison, and Antia S. Botana, 2021, Phys. Rev. B **104**, 205129.
Lacroix, Claudine, Philippe Mendels, and Frédéric Mila, 2011, *Introduction to Frustrated Magnetism: Materials, Experiments, Theory*, Springer Series in Solid-State Sciences Vol. 164 (Springer, New York).
Larkin, A. I., and Yu. N. Ovchinnikov, 1964, Zh. Eksp. Teor. Fiz. **47**, 1136 [Sov. Phys. JETP **20**, 762 (1965)], https://www.osti.gov/biblio/4653415.
Larsson, A. K., M. Haeberlein, S. Lidin, and U. Schwarz, 1996, J. Alloys Compd. **240**, 79.
Le, Tian, *et al.*, 2024, Nature (London) **630**, 64.
Le Caer, G., B. Malaman, L. Haggstrom, and T. Ericsson, 1979, J. Phys. F **9**, 1905.
Le Caer, G., B. Malaman, and B. Roques, 1978, J. Phys. F **8**, 323.
Lee, Ching Hua, Stefan Imhof, Christian Berger, Florian Bayer, Johannes Brehm, Laurens W. Molenkamp, Tobias Kiessling, and Ronny Thomale, 2018, Commun. Phys. **1**, 39.
Lee, Jae Hyuck, *et al.*, 2024, ACS Nano **18**, 25535.
Lee, Jeonghun, and Eundeok Mun, 2022, Phys. Rev. Mater. **6**, 083401.
Lee, Patrick A., Naoto Nagaosa, and Xiao-Gang Wen, 2006, Rev. Mod. Phys. **78**, 17.
Lee, Seongyong, *et al.*, 2024, npj Quantum Mater. **9**, 15.
Lee, Y., *et al.*, 2023, Phys. Rev. B **108**, 045132.
Li, Cong, *et al.*, 2022, Phys. Rev. Res. **4**, 033072.
Li, Guowei, *et al.*, 2019, Sci. Adv. **5**, eaaw9867.
Li, Hang, Bei Ding, Jie Chen, Xuekui Xi, Hongwei Zhang, Yong-Chang Lau, and Wenhong Wang, 2023, J. Phys. Condens. Matter **35**, 475701.
Li, Haoxiang, *et al.*, 2021, Phys. Rev. X **11**, 031050.
Li, Haoxiang, *et al.*, 2022, Nat. Commun. **13**, 6348.
Li, Heqiu, Yong Baek Kim, and Hae-Young Kee, 2024, Phys. Rev. Lett. **132**, 146501.
Li, Hong, He Zhao, Kun Jiang, Qi Wang, Qiangwei Yin, Ning-Ning Zhao, Kai Liu, Ziqiang Wang, Hechang Lei, and Ilija Zeljkovic, 2022, Nat. Phys. **18**, 644.
Li, Hong, He Zhao, Brenden R. Ortiz, Yuzki Oey, Ziqiang Wang, Stephen D. Wilson, and Ilija Zeljkovic, 2023, Nat. Phys. **19**, 637.
Li, Hong, He Zhao, Brenden R. Ortiz, Takamori Park, Mengxing Ye, Leon Balents, Ziqiang Wang, Stephen D. Wilson, and Ilija Zeljkovic, 2022, Nat. Phys. **18**, 265.
Li, Hong, He Zhao, Qiangwei Yin, Qi Wang, Zheng Ren, Shrinkhala Sharma, Hechang Lei, Ziqiang Wang, and Ilija Zeljkovic, 2022, Sci. Rep. **12**, 14525.
Li, Hong, *et al.*, 2023a, Nat. Phys. **19**, 1591.
Li, Hong, *et al.*, 2023b, Phys. Rev. X **13**, 031030.
Li, Hong, *et al.*, 2024, Nat. Phys. **20**, 1103.
Li, Huazhou, Siyuan Wan, Han Li, Qing Li, Qiangqiang Gu, Huan Yang, Yongkai Li, Zhiwei Wang, Yugui Yao, and Hai-Hu Wen, 2022, Phys. Rev. B **105**, 045102.
Li, Man, *et al.*, 2021, Nat. Commun. **12**, 3129.
Li, Sheng, Bin Zeng, Xiangang Wan, Jian Tao, Fei Han, Huan Yang, Zhihe Wang, and Hai-Hu Wen, 2011, Phys. Rev. B **84**, 214527.
Li, Xiaokang, Liangcai Xu, Linchao Ding, Jinhua Wang, Mingsong Shen, Xiufang Lu, Zengwei Zhu, and Kamran Behnia, 2017, Phys. Rev. Lett. **119**, 056601.
Li, Yidian, *et al.*, 2025, Nat. Commun. **16**, 3229.
Li, Yongkai, *et al.*, 2022, Phys. Rev. B **105**, L180507.
Li, Zhenglu, Meng Wu, Yang-Hao Chan, and Steven G. Louie, 2021, Phys. Rev. Lett. **126**, 146401.
Liang, Tian, *et al.*, 2018, Nat. Phys. **14**, 451.
Liang, Zuowei, *et al.*, 2021, Phys. Rev. X **11**, 031026.
Lieb, Elliott H., 1989, Phys. Rev. Lett. **62**, 1201.
Ligenza, S., 1971, Phys. Status Solidi B **44**, 775.
Ligenza, S., 1972, Phys. Status Solidi B **50**, 379.

Lin, Yu-Ping, and Rahul M. Nandkishore, 2021, Phys. Rev. B **104**, 045122.
Lin, Zhiyong, *et al.*, 2018, Phys. Rev. Lett. **121**, 096401.
Lin, Zhiyong, *et al.*, 2020, Phys. Rev. B **102**, 155103.
Liu, Bo, *et al.*, 2023, Phys. Rev. Lett. **131**, 026701.
Liu, D. F., *et al.*, 2019, Science **365**, 1282.
Liu, Enke, *et al.*, 2018, Nat. Phys. **14**, 1125.
Liu, Gan, *et al.*, 2022, Nat. Commun. **13**, 3461.
Liu, HongXiong, *et al.*, 2023, Phys. Rev. B **108**, 104504.
Liu, Jianpeng, and Leon Balents, 2017, Phys. Rev. Lett. **119**, 087202.
Liu, Mengqin, Tao Han, Xinran Hu, Yubing Tu, Zongyuan Zhang, Mingsheng Long, Xingyuan Hou, Qingge Mu, and Lei Shan, 2022, Phys. Rev. B **106**, L140501.
Liu, Min, Zhiwei Wang, and Jin-Jian Zhou, 2022, Phys. Rev. B **105**, 235130.
Liu, Shuyuan, Chongze Wang, Shichang Yao, Yu Jia, Zhenyu Zhang, and Jun-Hyung Cho, 2024, Phys. Rev. B **109**, L121103.
Liu, Xiangqi, *et al.*, 2025, arXiv:2508.08580.
Liu, Xiaolong, Yi Xue Chong, Rahul Sharma, and J. C. Séamus Davis, 2021, Science **372**, 1447.
Liu, Yi, *et al.*, 2024, Nature (London) **632**, 1032.
Liu, Yixuan, *et al.*, 2023, Phys. Rev. Mater. **7**, 064801.
Liu, Zhonghao, *et al.*, 2020, Nat. Commun. **11**, 4002.
Lou, Rui, Alexander Fedorov, Qiangwei Yin, Andrii Kuibarov, Zhijun Tu, Chunsheng Gong, Eike F. Schwier, Bernd Bchner, Hechang Lei, and Sergey Borisenko, 2022, Phys. Rev. Lett. **128**, 036402.
Lu, Ling, John D. Joannopoulos, and Marin Soljačić, 2014, Nat. Photonics **8**, 821.
Luo, Hailan, *et al.*, 2022, Nat. Commun. **13**, 273.
Luo, J., Z. Zhao, Y. Z. Zhou, J. Yang, A. F. Fang, H. T. Yang, H. J. Gao, R. Zhou, and Guo-qing Zheng, 2022, npj Quantum Mater. **7**, 30.
Luo, Yang, *et al.*, 2023, Nat. Commun. **14**, 3819.
Lv, Senhao, *et al.*, 2025, Adv. Funct. Mater. **35**, 2412876.
Ma, Da-Shuai, Yuanfeng Xu, Christie S. Chiu, Nicolas Regnault, Andrew A. Houck, Zhida Song, and B. Andrei Bernevig, 2020, Phys. Rev. Lett. **125**, 266403.
Malaman, B., D. Fruchart, and G. Le Caer, 1978, J. Phys. F **8**, 2389.
Malaman, B., B. Roques, A. Courtois, and J. Protas, 1976, Acta Crystallogr. Sect. B **32**, 1348.
Malaman, B., G. Venturini, R. Welter, J. P. Sanchez, P. Vulliet, and E. Ressouche, 1999, J. Magn. Magn. Mater. **202**, 519.
Mantravadi, Aishwarya, Volodymyr Gvozdetskyi, Arka Sarkar, Yaroslav Mudryk, and Julia V. Zaikina, 2023, Phys. Rev. Mater. **7**, 115002.
Mantravadi, Aishwarya, *et al.*, 2024, J. Am. Chem. Soc. **146**, 26786.
Mazin, I. I., Harald O. Jeschke, Frank Lechermann, Hunpyo Lee, Mario Fink, Ronny Thomale, and Roser Valentí, 2014, Nat. Commun. **5**, 4261.
Mazzola, Federico, *et al.*, 2023, Nano Lett. **23**, 8035.
Mazzola, Federico, *et al.*, 2025, arXiv:2502.19589.
Meier, William R., Jiaqiang Yan, Michael A. McGuire, Xiaoping Wang, Andrew D. Christianson, and Brian C. Sales, 2019, Phys. Rev. B **100**, 184421.
Meier, William R., *et al.*, 2023, J. Am. Chem. Soc. **145**, 20943.
Mendels, Philippe, and Fabrice Bert, 2010, J. Phys. Soc. Jpn. **79**, 011001.
Meng, Yu-Xin, Cheng-Long Xue, Li-Guo Dou, Wei-Min Zhao, Qi-Wei Wang, Yong-Jie Xu, Xiangqi Liu, Wei Xia, Yanfeng Guo, and Shao-Chun Li, 2023, Chin. Phys. B **32**, 096801.
Miao, H., *et al.*, 2023, Nat. Commun. **14**, 6183.
Miao, Hu, *et al.*, 2021, Phys. Rev. B **104**, 195132.
Mielke, Andreas, 1991a, J. Phys. A **24**, L73.
Mielke, Andreas, 1991b, J. Phys. A **24**, 3311.
Mielke, C., *et al.*, 2021, Phys. Rev. Mater. **5**, 034803.
Mielke III, C., *et al.*, 2024, arXiv:2402.16219.
Mielke III, Charles, *et al.*, 2022, Nature (London) **602**, 245.
Mihalyuk, Alexey N., Dimitry V. Gruznev, Leonid V. Bondarenko, Alexandra Y. Tupchaya, Yuriy E. Vekovshinin, Sergey V. Eremeev, Andrey V. Zotov, and Alexander A. Saranin, 2022, Nanoscale **14**, 14732.
Miller, Gordon J., 1995, J. Alloys Compd. **217**, 5.
Mine, Akifumi, *et al.*, 2024, arXiv:2404.18472.
Misawa, Ryo, Markus Kriener, Rinsuke Yamada, Ryota Nakano, Milena Jovanovic, Leslie M. Schoop, and Max Hirschberger, 2025, Phys. Rev. Res. **7**, 033032.
Mojarro, M. A., and Sergio E. Ulloa, 2024, Phys. Rev. B **110**, 235129.
Morali, Noam, Rajib Batabyal, Pranab Kumar Nag, Enke Liu, Qiunan Xu, Yan Sun, Binghai Yan, Claudia Felser, Nurit Avraham, and Haim Beidenkopf, 2019, Science **365**, 1286.
Motoyama, Gaku, Masumi Sezaki, Jun Gouchi, Kiyotaka Miyoshi, Shijo Nishigori, Tetsuya Mutou, Kenji Fujiwara, and Yoshiya Uwatoko, 2018, Physica (Amsterdam) **536B**, 142.
Mozaffari, Shirin, Seung-Hwan Do, Richa P. Madhogaria, Aikaterini Flessa Savvidou, Brian W. Casas, William R. Meier, Rui Xue, Eun Sang Choi, Luis Balicas, and David G. Mandrus, 2025, Phys. Rev. B **112**, 115147.
Mozaffari, Shirin, *et al.*, 2024, Phys. Rev. B **110**, 035135.
Mravlje, Jernej, Markus Aichhorn, Takashi Miyake, Kristjan Haule, Gabriel Kotliar, and Antoine Georges, 2011, Phys. Rev. Lett. **106**, 096401.
Mu, Chao, Qiangwei Yin, Zhijun Tu, Chunsheng Gong, Hechang Lei, Zheng Li, and Jianlin Luo, 2021, Chin. Phys. Lett. **38**, 077402.
Multer, Daniel, *et al.*, 2023, Commun. Mater. **4**, 17.
Nagamiya, T., S. Tomiyoshi, and Y. Yamaguchi, 1982, Solid State Commun. **42**, 385.
Nakamura, R., *et al.*, 2024, Phys. Rev. B **110**, L081109.
Nakatsuji, Satoru, Naoki Kiyohara, and Tomoya Higo, 2015, Nature (London) **527**, 212.
Nakayama, Kosuke, Yongkai Li, Takemi Kato, Min Liu, Zhiwei Wang, Takashi Takahashi, Yugui Yao, and Takafumi Sato, 2021, Phys. Rev. B **104**, L161112.
Nayak, Ajaya K., *et al.*, 2016, Sci. Adv. **2**, e1501870.
Nayak, Chetan, 2000, Phys. Rev. B **62**, 4880.
Neupert, Titus, M. Michael Denner, Jia-Xin Yin, Ronny Thomale, and M. Zahid Hasan, 2022, Nat. Phys. **18**, 137.
Neupert, Titus, Luiz Santos, Claudio Chamon, and Christopher Mudry, 2011, Phys. Rev. Lett. **106**, 236804.
Nie, Linpeng, *et al.*, 2022, Nature (London) **604**, 59.
Ning, Honglie, *et al.*, 2024, Nat. Commun. **15**, 7286.
Norman, M. R., 2016, Rev. Mod. Phys. **88**, 041002.
Oey, Yuzki M., Brenden R. Ortiz, Farnaz Kaboudvand, Jonathan Frassineti, Erick Garcia, Rong Cong, Samuele Sanna, Vesna F. Mitrović, Ram Seshadri, and Stephen D. Wilson, 2022, Phys. Rev. Mater. **6**, L041801.
Oh, Ji Seop, *et al.*, 2025, Sci. Adv. **11**, eadt2195.
Okamoto, Satoshi, Narayan Mohanta, Elbio Dagotto, and D. N. Sheng, 2022, Commun. Phys. **5**, 198.
Ortiz, Brenden R., Andrea N. Capa Salinas, Miles J. Knudtson, Paul M. Sarte, Ganesh Pokahrel, and Stephen D. Wilson, 2023, Phys. Rev. Mater. **7**, 014801.
Ortiz, Brenden R., Paul M. Sarte, Eric M. Kenney, Michael J. Graf, Samuel M. L. Teicher, Ram Seshadri, and Stephen D. Wilson, 2021, Phys. Rev. Mater. **5**, 034801.

Ortiz, Brenden R., Samuel M. L. Teicher, Linus Kautzsch, Paul M. Sarte, Noah Ratcliff, John Harter, Jacob P. C. Ruff, Ram Seshadri, and Stephen D. Wilson, 2021, Phys. Rev. X **11**, 041030.
Ortiz, Brenden R., *et al.*, 2019, Phys. Rev. Mater. **3**, 094407.
Ortiz, Brenden R., *et al.*, 2020, Phys. Rev. Lett. **125**, 247002.
Ortiz, Brenden R., *et al.*, 2023a, Chem. Mater. **35**, 9756.
Ortiz, Brenden R., *et al.*, 2023b, Phys. Rev. Mater. **7**, 064201.
Ortiz, Brenden R., *et al.*, 2024, Chem. Mater. **36**, 8002.
Ortiz, Brenden R., *et al.*, 2025, J. Am. Chem. Soc. **147**, 5279.
Ovchinnikov, Alexander, and Svilen Bobev, 2020, Inorg. Chem. **59**, 3459.
Park, Seunghyun, *et al.*, 2020, Sci. Rep. **10**, 20998.
Pasco, Christopher M., Ismail El Baggari, Elisabeth Bianco, Lena F. Kourkoutis, and Tyrel M. McQueen, 2019, ACS Nano **13**, 9457.
Peng, Rui, Yandong Ma, Xilong Xu, Zhonglin He, Baibiao Huang, and Ying Dai, 2020, Phys. Rev. B **102**, 035412.
Peng, Shuting, *et al.*, 2021, Phys. Rev. Lett. **127**, 266401.
Peng, Shuting, *et al.*, 2024, arXiv:2406.17769.
Pham, Tuan Anh, Seoung-Hun Kang, Yasemin Ozbek, Mina Yoon, and Pengpeng Zhang, 2024, ACS Nano **18**, 8768.
Pielnhofer, Florian, Jan Rothballer, Philipp Peter, Wenjie Yan, Falko M. Schappacher, Rainer Pöttgen, and Richard Weihrich, 2014, Z. Anorg. Allg. Chem. **640**, 286.
Plokhikh, I., *et al.*, 2024, Commun. Phys. **7**, 182.
Plumb, Jayden, *et al.*, 2024, Phys. Rev. Mater. **8**, 093601.
Pokharel, Ganesh, Brenden Ortiz, Juan Chamorro, Paul Sarte, Linus Kautzsch, Guang Wu, Jacob Ruff, and Stephen D. Wilson, 2022, Phys. Rev. Mater. **6**, 104202.
Pokharel, Ganesh, Brenden R. Ortiz, Linus Kautzsch, S. J. Gomez Alvarado, Krishnanand Mallayya, Guang Wu, Eun-Ah Kim, Jacob P. C. Ruff, Suchismita Sarker, and Stephen D. Wilson, 2023, Phys. Rev. Mater. **7**, 104201.
Pokharel, Ganesh, Samuel M. L. Teicher, Brenden R. Ortiz, Paul M. Sarte, Guang Wu, Shuting Peng, Junfeng He, Ram Seshadri, and Stephen D. Wilson, 2021, Phys. Rev. B **104**, 235139.
Porter, Zach, Ganesh Pokharel, Jong-Woo Kim, Phillip J. Ryan, and Stephen D. Wilson, 2023, Phys. Rev. B **108**, 035134.
Profe, Jonas B., Lennart Klebl, Francesco Grandi, Hendrik Hohmann, Matteo Dürrnagel, Tilman Schwemmer, Ronny Thomale, and Dante M. Kennes, 2024, Phys. Rev. Res. **6**, 043078.
Qian, Tiema, Morten H. Christensen, Chaowei Hu, Amartyajyoti Saha, Brian M. Andersen, Rafael M. Fernandes, Turan Birol, and Ni Ni, 2021, Phys. Rev. B **104**, 144506.
Ratcliff, Noah, Lily Hallett, Brenden R. Ortiz, Stephen D. Wilson, and John W. Harter, 2021, Phys. Rev. Mater. **5**, L111801.
Regmi, Sabin, *et al.*, 2022, Commun. Mater. **3**, 100.
Regmi, Sabin, *et al.*, 2023, Phys. Rev. B **108**, L121404.
Rehfuss, Zackary, *et al.*, 2024, Phys. Rev. Mater. **8**, 024003.
Ren, Zheng, *et al.*, 2022, npj Quantum Mater. **7**, 109.
Ren, Zheng, *et al.*, 2024, Nat. Commun. **15**, 9376.
Rhim, Jun-Won, Kyoo Kim, and Bohm-Jung Yang, 2020, Nature (London) **584**, 59.
Rhim, Jun-Won, and Bohm-Jung Yang, 2021, Adv. Phys. X **6**, 1901606.
Riberolles, S. X. M., Tyler J. Slade, D. L. Abernathy, G. E. Granroth, Bing Li, Y. Lee, P. C. Canfield, B. G. Ueland, Liqin Ke, and R. J. McQueeney, 2022, Phys. Rev. X **12**, 021043.
Riberolles, Simon X. M., *et al.*, 2024, npj Quantum Mater. **9**, 42.
Richardson, Marcus, 1967, Acta Chem. Scand. **21**, 753.
Ritz, Ethan T., Rafael M. Fernandes, and Turan Birol, 2023, Phys. Rev. B **107**, 205131.
Ritz, Ethan T., Henrik S. Røising, Morten H. Christensen, Turan Birol, Brian M. Andersen, and Rafael M. Fernandes, 2023, Phys. Rev. B **108**, L100510.
Romaka, L., Yu. Stadnyk, V. V. Romaka, P. Demchenko, M. Stadnyshyn, and M. Konyk, 2011, J. Alloys Compd. **509**, 8862.
Rømer, Astrid T., Shinibali Bhattacharyya, Roser Valentí, Morten H. Christensen, and Brian M. Andersen, 2022, Phys. Rev. B **106**, 174514.
Roppongi, M., *et al.*, 2023, Nat. Commun. **14**, 667.
Rosenberg, Elliott, Jonathan M. DeStefano, Yongbin Lee, Chaowei Hu, Yue Shi, David Graf, Shermane M. Benjamin, Liqin Ke, and Jiun-Haw Chu, 2024, Phys. Rev. B **110**, 035119.
Rosenberg, Elliott, *et al.*, 2022, Phys. Rev. B **106**, 115139.
Rosenfeld, E. V., and N. V. Mushnikov, 2008, Physica (Amsterdam) **403B**, 1898.
Roychowdhury, Krishanu, Jan Attig, Simon Trebst, and Michael J. Lawler, 2024, Phys. Rev. Res. **6**, 043273.
Sakhya, Anup Pradhan, *et al.*, 2024, Commun. Mater. **5**, 241.
Sales, B. C., *et al.*, 2021, Phys. Rev. Mater. **5**, 044202.
Sales, Brian C., Jiaqiang Yan, William R. Meier, Andrew D. Christianson, Satoshi Okamoto, and Michael A. McGuire, 2019, Phys. Rev. Mater. **3**, 114203.
Sales, Brian C., *et al.*, 2022, Chem. Mater. **34**, 7069.
Sangiovanni, G., 2024, Nature (London) **632**, 988.
Sankar, Soumya, *et al.*, 2024, Phys. Rev. X **14**, 021046.
Saykin, David R., *et al.*, 2023, Phys. Rev. Lett. **131**, 016901.
Scammell, Harley D., Julian Ingham, Tommy Li, and Oleg P. Sushkov, 2023, Nat. Commun. **14**, 605.
Scheurer, Mathias S., and Harley D. Scammell, 2025, arXiv:2507.15527.
Schilberth, F., *et al.*, 2024, arXiv:2408.03575.
Schüler, Michael, Umberto De Giovannini, Hannes Hbener, Angel Rubio, Michael A. Sentef, and Philipp Werner, 2020, Sci. Adv. **6**, eaay2730.
Schobinger-Papamantellos, P., J. Rodríguez-Carvajal, and K. H. J. Buschow, 1997, J. Alloys Compd. **256**, 92.
Schwemmer, Tilman, *et al.*, 2024, Phys. Rev. B **110**, 024501.
Setty, Chandan, Christopher A. Lane, Lei Chen, Haoyu Hu, Jian-Xin Zhu, and Qimiao Si, 2022, arXiv:2203.01930.
Shama, R. K., and Yogesh Singh, 2020, J. Magn. Magn. Mater. **502**, 166547.
Shan, P. F., *et al.*, 2023, Mater. Today Phys. **38**, 101267.
Shao, Sen, *et al.*, 2023, ACS Nano **17**, 10164.
Shen, Jianlei, *et al.*, 2020, Adv. Funct. Mater. **30**, 2000830.
Sheng, L., D. N. Sheng, and C. S. Ting, 2006, Phys. Rev. Lett. **96**, 155901.
Shi, Chenfei, *et al.*, 2024, arXiv:2404.00996.
Shi, Mengzhu, *et al.*, 2022, Nat. Commun. **13**, 2773.
Shrestha, K., *et al.*, 2022, Phys. Rev. B **105**, 024508.
Shrestha, Keshav, Binod Regmi, Ganesh Pokharel, Seong-Gon Kim, Stephen D. Wilson, David E. Graf, Birendra A. Magar, Cole Phillips, and Thinh Nguyen, 2023, Phys. Rev. B **108**, 245119.
Shumiya, Nana, *et al.*, 2021, Phys. Rev. B **104**, 035131.
Si, Q., R. Yu, and E. Abrahams, 2016, Nat. Rev. Mater. **1**, 16017.
Soh, Jian-Rui, ChangJiang Yi, Ivica Zivkovic, Navid Qureshi, Anne Stunault, Bachir Ouladdiaf, J. Alberto Rodríguez-Velamazán, YouGuo Shi, Henrik M. Rønnow, and Andrew T. Boothroyd, 2022, Phys. Rev. B **105**, 094435.
Song, Boqin, *et al.*, 2023, Nat. Commun. **14**, 2492.
Song, Boqin, *et al.*, 2025, Nat. Commun. **16**, 5643.
Song, DianWu, *et al.*, 2022, Sci. China Phys. Mech. Astron. **65**, 247462.

Stahl, Q., D. Chen, T. Ritschel, C. Shekhar, E. Sadrollahi, M. C. Rahn, O. Ivashko, M. v. Zimmermann, C. Felser, and J. Geck, 2022, Phys. Rev. B **105**, 195136.
Stier, F., *et al.*, 2024, Phys. Rev. Lett. **133**, 236503.
Strohm, C., G. L. J. A. Rikken, and P. Wyder, 2005, Phys. Rev. Lett. **95**, 155901.
Subedi, Alaska, 2024, Phys. Rev. Mater. **8**, 014006.
Subires, D., A. Korshunov, A. H. Said, L Sánchez, Brenden R. Ortiz, Stephen D. Wilson, A. Bosak, and S. Blanco-Canosa, 2023, Nat. Commun. **14**, 1015.
Subires, D., *et al.*, 2025, Nat. Commun. **16**, 4091.
Sun, Kai, Zhengcheng Gu, Hosho Katsura, and S. Das Sarma, 2011, Phys. Rev. Lett. **106**, 236803.
Sun, Zhenyu, *et al.*, 2022, Nano Lett. **22**, 4596.
Sur, Yeahan, Kwang-Tak Kim, Sukho Kim, and Kee Hoon Kim, 2023, Nat. Commun. **14**, 3899.
Süsstrunk, Roman, and Sebastian D. Huber, 2015, Science **349**, 47.
Sutherland, Bill, 1986, Phys. Rev. B **34**, 5208.
Takeuchi, Yutaro, Yuta Yamane, Ju-Young Yoon, Ryuichi Itoh, Butsurin Jinnai, Shun Kanai, Junichi Ieda, Shunsuke Fukami, and Hideo Ohno, 2021, Nat. Mater. **20**, 1364.
Tan, Hengxin, Yizhou Liu, Ziqiang Wang, and Binghai Yan, 2021, Phys. Rev. Lett. **127**, 046401.
Tan, Hengxin, and Binghai Yan, 2023, Phys. Rev. Lett. **130**, 266402.
Tan, Hengxin, and Binghai Yan, 2024, Phys. Rev. B **109**, 195428.
Tan, Hengxin, and Binghai Yan, 2025, Phys. Rev. B **111**, 045160.
Tanaka, M., *et al.*, 2020, Nano Lett. **20**, 7476.
Tang, Evelyn, Jia-Wei Mei, and Xiao-Gang Wen, 2011, Phys. Rev. Lett. **106**, 236802.
Tang, Kaixin, *et al.*, 2024, Phys. Rev. Res. **6**, 013276.
Tao, Yu, Luke Daemen, Yongqiang Cheng, Joerg C. Neuefeind, and Despina Louca, 2023, Phys. Rev. B **107**, 174407.
Tasaki, Hal, 1992, Phys. Rev. Lett. **69**, 1608.
Teng, Xiaokun, *et al.*, 2022, Nature (London) **609**, 490.
Teng, Xiaokun, *et al.*, 2023, Nat. Phys. **19**, 814.
Thakur, Gohil S., Praveen Vir, Satya N. Guin, Chandra Shekhar, Richard Weihrich, Yan Sun, Nitesh Kumar, and Claudia Felser, 2020, Chem. Mater. **32**, 1612.
Tomiyoshi, Shoichi, 1982, J. Phys. Soc. Jpn. **51**, 803.
Tsirlin, Alexander A., Brenden R. Ortiz, Martin Dressel, Stephen D. Wilson, Stephan Winnerl, and Ece Uykur, 2023, Phys. Rev. B **107**, 174107.
Tuniz, Manuel, *et al.*, 2023, Commun. Mater. **4**, 103.
Tuniz, Manuel, *et al.*, 2025, Phys. Rev. Lett. **134**, 066501.
Ugeda, Miguel M., *et al.*, 2016, Nat. Phys. **12**, 92.
Uykur, E., B. R. Ortiz, O. Iakutkina, M. Wenzel, S. D. Wilson, M. Dressel, and A. A. Tsirlin, 2021, Phys. Rev. B **104**, 045130.
Uykur, Ece, Brenden R. Ortiz, Stephen D. Wilson, Martin Dressel, and Alexander A. Tsirlin, 2022, npj Quantum Mater. **7**, 16.
Vaqueiro, Paz, and Gerard G. Sobany, 2009, Solid State Sci. **11**, 513.
Varma, C. M., and A. L. Simons, 1983, Phys. Rev. Lett. **51**, 138.
Varma, Chandra M., and Ziqiang Wang, 2023, Phys. Rev. B **108**, 214516.
Vekovshinin, Yuriy E., Leonid V. Bondarenko, Alexandra Y. Tupchaya, Alexey N. Mihalyuk, Nikita V. Denisov, Dimitry V. Gruznev, Andrey V. Zotov, and Alexander A. Saranin, 2024, Nano Lett. **24**, 9931.
Venderbos, J. W. F., 2016, Phys. Rev. B **93**, 115107.
Venturini, G., D. Fruchart, and B. Malaman, 1996, J. Alloys Compd. **236**, 102.
Vijay, Kritika, L. S. Chandra, Kawsar Ali, Archna Sagdeo, Pragya Tiwari, M. K. Chattopadhyay, A. Arya, and Soma Banik, 2023, Appl. Phys. Lett. **122**, 233103.
Vonsovskii, S. V., M. I. Katsnelson, and A. V. Trefilov, 1993, Phys. Met. Metallogr. **76**, 247, https://theorphys.science.ru.nl/people/katsnelson/VKT93_part1.pdf.
Wagner, Glenn, Chunyu Guo, Philip J. W. Moll, Titus Neupert, and Mark H. Fischer, 2023, Phys. Rev. B **108**, 125136.
Wakao, Hiromasa, Tsuneya Yoshida, Hiromu Araki, Tomonari Mizoguchi, and Yasuhiro Hatsugai, 2020, Phys. Rev. B **101**, 094107.
Wakefield, Joshua P., *et al.*, 2023, Nature (London) **623**, 301.
Wan, Sicong, Haiyan Lu, and Li Huang, 2022, Phys. Rev. B **105**, 155131.
Wang, Bin, Enkui Yi, Leyi Li, Jianwei Qin, Bing-Feng Hu, Bing Shen, and Meng Wang, 2022, Phys. Rev. B **106**, 125107.
Wang, Chongze, Yu Jia, Zhenyu Zhang, and Jun-Hyung Cho, 2023, Phys. Rev. B **108**, L060503.
Wang, Jian-Sheng, and Lifa Zhang, 2009, Phys. Rev. B **80**, 012301.
Wang, Jingyuan, Camron Farhang, Brenden R. Ortiz, Stephen D. Wilson, and Jing Xia, 2024, Phys. Rev. Mater. **8**, 014202.
Wang, Kang, Siyu Chen, Sun-Woo Kim, and Bartomeu Monserrat, 2024, Nat. Commun. **15**, 10428.
Wang, Lingfei, *et al.*, 2023, J. Phys. Mater. **6**, 02LT01.
Wang, N. N., *et al.*, 2021, Phys. Rev. Res. **3**, 043018.
Wang, Pengdong, *et al.*, 2020, Chin. Phys. Lett. **37**, 087102.
Wang, Qi, Yuanfeng Xu, Rui Lou, Zhonghao Liu, Man Li, Yaobo Huang, Dawei Shen, Hongming Weng, Shancai Wang, and Hechang Lei, 2018, Nat. Commun. **9**, 3681.
Wang, Qi, *et al.*, 2021, Adv. Mater. **33**, 2102813.
Wang, Wan-Sheng, Zheng-Zhao Li, Yuan-Yuan Xiang, and Qiang-Hua Wang, 2013, Phys. Rev. B **87**, 115135.
Wang, Yaojia, Gregory T. McCandless, Xiaoping Wang, Kulatheepan Thanabalasingam, Heng Wu, Damian Bouwmeester, Herre S. J. van der Zant, Mazhar N. Ali, and Julia Y. Chan, 2022, Chem. Mater. **34**, 7337.
Wang, Yaojia, Heng Wu, Gregory T. McCandless, Julia Y. Chan, and Mazhar N. Ali, 2023, Nat. Rev. Phys. **5**, 635.
Wang, Yidi, Hong Li, Siyu Cheng, He Zhao, Brenden R. Ortiz, Andrea Capa Salinas, Stephen D. Wilson, Ziqiang Wang, and Ilija Zeljkovic, 2025, Phys. Rev. X **15**, 021074.
Wang, Yilin, 2023, Phys. Rev. Mater. **7**, 104006.
Wang, Yuan, *et al.*, 2023, Chin. Phys. Lett. **40**, 037102.
Wang, Z. X., *et al.*, 2021, Phys. Rev. B **104**, 165110.
Wang, Zehao, *et al.*, 2025, Nat. Commun. **16**, 7573.
Wang, Zhengguo, *et al.*, 2021, arXiv:2104.05556.
Wang, Zhiwei, *et al.*, 2021, Phys. Rev. B **104**, 075148.
Watanabe, Hiroshi, and Nobuhiko Kunitomi, 1966, J. Phys. Soc. Jpn. **21**, 1932.
Watzenböck, C., M. Edelmann, D. Springer, G. Sangiovanni, and A. Toschi, 2020, Phys. Rev. Lett. **125**, 086402.
Weihrich, Richard, A. C. Stückl, M. Zabel, and W. Schnelle, 2004, Z. Anorg. Allg. Chem. **630**, 1767.
Weiland, Ashley, Lucas J. Eddy, Gregory T. McCandless, Halyna Hodovanets, Johnpierre Paglione, and Julia Y. Chan, 2020, Cryst. Growth Des. **20**, 6715.
Wen, Xikai, *et al.*, 2024, Phys. Rev. Res. **6**, 033222.
Wenger, Anja, Armando Consiglio, Hendrik Hohmann, Matteo Dürrnagel, Fabian O. von Rohr, Harley D. Scammell, Julian Ingham, Domenico Di Sante, and Ronny Thomale, 2024, arXiv:2411.03563.
Wenzel, M., B. R. Ortiz, S. D. Wilson, M. Dressel, A. A. Tsirlin, and E. Uykur, 2022, Phys. Rev. B **105**, 245123.
Wenzel, M., E. Uykur, A. A. Tsirlin, A. N. Capa Salinas, B. R. Ortiz, S. D. Wilson, and M. Dressel, 2025, Phys. Rev. B **112**, L041122.

Werhahn, Dominik, Brenden R. Ortiz, Aurland K. Hay, Stephen D. Wilson, Ram Seshadri, and Dirk Johrendt, 2022, Z. Naturforsch. B **77**, 757.
Wilson, Stephen D., and Brenden R. Ortiz, 2024, Nat. Rev. Mater. **9**, 420.
Wu, Peng, *et al.*, 2021, Appl. Phys. Lett. **119**, 082401.
Wu, Ping, *et al.*, 2023, Nat. Phys. **19**, 1143.
Wu, Shangfei, Brenden R. Ortiz, Hengxin Tan, Stephen D. Wilson, Binghai Yan, Turan Birol, and Girsh Blumberg, 2022, Phys. Rev. B **105**, 155106.
Wu, Shangfei, *et al.*, 2024, Phys. Rev. X **14**, 011043.
Wu, Siqi, Chenchao Xu, Xiaoqun Wang, Hai-Qing Lin, Chao Cao, and Guang-Han Cao, 2025, Nat. Commun. **16**, 1375.
Wu, Wenfeng, Xiaocheng Bai, Xianlong Wang, Dayong Liu, Zhi Zeng, and Liangjian Zou, 2024, arXiv:2403.16119.
Wu, Xianxin, *et al.*, 2021, Phys. Rev. Lett. **127**, 177001.
Wu, Xueliang, Xinrun Mi, Long Zhang, Chin-Wei Wang, Nour Maraytta, Xiaoyuan Zhou, Mingquan He, Michael Merz, Yisheng Chai, and Aifeng Wang, 2024, Phys. Rev. Lett. **132**, 256501.
Wu, Yi-Ming, Ronny Thomale, and S. Raghu, 2023, Phys. Rev. B **108**, L081117.
Wulferding, Dirk, *et al.*, 2022, Phys. Rev. Res. **4**, 023215.
Xiang, Ying, Qing Li, Yongkai Li, Wei Xie, Huan Yang, Zhiwei Wang, Yugui Yao, and Hai-Hu Wen, 2021, Nat. Commun. **12**, 6727.
Xiao, Di, Ming-Che Chang, and Qian Niu, 2010, Rev. Mod. Phys. **82**, 1959.
Xiao, Qian, *et al.*, 2023, Phys. Rev. Res. **5**, L012032.
Xie, Fang, Yuan Fang, Ying Li, Yuefei Huang, Lei Chen, Chandan Setty, Shouvik Sur, Boris Yakobson, Roser Valentí, and Qimiao Si, 2025, Phys. Rev. Res. **7**, L022061.
Xie, Yaofeng, *et al.*, 2022, Phys. Rev. B **105**, L140501.
Xing, Yuqing, *et al.*, 2024, Nature (London) **631**, 60.
Xu, Chenchao, Siqi Wu, Guo-Xiang Zhi, Guanghan Cao, Jianhui Dai, Chao Cao, Xiaoqun Wang, and Hai-Qing Lin, 2025, Nat. Commun. **16**, 3114.
Xu, Gang, Biao Lian, and Shou-Cheng Zhang, 2015, Phys. Rev. Lett. **115**, 186802.
Xu, Han-Shu, Ya-Jun Yan, Ruotong Yin, Wei Xia, Shijie Fang, Ziyuan Chen, Yuanji Li, Wenqi Yang, Yanfeng Guo, and Dong-Lai Feng, 2021, Phys. Rev. Lett. **127**, 187004.
Xu, Qiunan, Enke Liu, Wujun Shi, Lukas Muechler, Jacob Gayles, Claudia Felser, and Yan Sun, 2018, Phys. Rev. B **97**, 235416.
Xu, Xitong, *et al.*, 2022, Nat. Commun. **13**, 1197.
Xu, Yishuai, Zhuoliang Ni, Yizhou Liu, Brenden R. Ortiz, Qinwen Deng, Stephen D. Wilson, Binghai Yan, Leon Balents, and Liang Wu, 2022, Nat. Phys. **18**, 1470.
Xue, Haoran, Yihao Yang, and Baile Zhang, 2022, Nat. Rev. Mater. **7**, 974.
Yamada, Nobuyoshi, Hideki Sakai, Hideaki Mori, and Tetuo Ohoyama, 1988, Physica (Amsterdam) **149B+C**, 311.
Yamaguchi, Kazuyuki, and Hiroshi Watanabe, 1967, J. Phys. Soc. Jpn. **22**, 1210.
Yamamoto, Hisao, 1966, J. Phys. Soc. Jpn. **21**, 1058.
Yan, Shaohua, *et al.*, 2022, Phys. Rev. B **105**, 155115.
Yanagi, Yuki, Junya Ikeda, Kohei Fujiwara, Kentaro Nomura, Atsushi Tsukazaki, and Michi-To Suzuki, 2021, Phys. Rev. B **103**, 205112.
Yang, Haitao, *et al.*, 2022, arXiv:2209.03840.
Yang, Haitao, *et al.*, 2024, Nat. Commun. **15**, 9626.
Yang, Hao, Yan Sun, Yang Zhang, Wu-Jun Shi, Stuart S. P. Parkin, and Binghai Yan, 2017, New J. Phys. **19**, 015008.
Yang, Jiangang, *et al.*, 2023, Nat. Commun. **14**, 4089.
Yang, Jinying, *et al.*, 2025, Nat. Electron. **8**, 386.
Yang, Qing-Geng, Meng Yao, Da Wang, and Qiang-Hua Wang, 2024, Phys. Rev. B **109**, 075130.
Yang, R., Y.-Y. Zhu, M. Steigleder, Y.-C. Liu, C.-C. Liu, X.-G. Qiu, Tiantian Zhang, and M. Dressel, 2025, Phys. Rev. Lett. **134**, 196905.
Yang, Shuo-Ying, *et al.*, 2020, Sci. Adv. **6**, eabb6003.
Yang, Zhaoju, Fei Gao, Xihang Shi, Xiao Lin, Zhen Gao, Yidong Chong, and Baile Zhang, 2015, Phys. Rev. Lett. **114**, 114301.
Yao, M., H. Lee, N. Xu, Y. Wang, J. Ma, OV Yazyev, Y. Xiong, M. Shi, G. Aeppli, and Y. Soh, 2018, arXiv:1810.01514.
Ye, Linda, *et al.*, 2018, Nature (London) **555**, 638.
Ye, Linda, *et al.*, 2024, Nat. Phys. **20**, 610.
Yi, Changjiang, Xiaolong Feng, Nitesh Kumar, Claudia Felser, and Chandra Shekhar, 2024, New J. Phys. **26**, 052001.
Yi, Changjiang, Xiaolong Feng, Ning Mao, Premakumar Yanda, Subhajit Roychowdhury, Yang Zhang, Claudia Felser, and Chandra Shekhar, 2024, Phys. Rev. B **109**, 035124.
Yi, Shaohui, *et al.*, 2025, Phys. Rev. Lett. **134**, 086902.
Yi, Xin-Wei, Zheng-Wei Liao, Jing-Yang You, Bo Gu, and Gang Su, 2023, Research **6**, 0238.
Yin, Jia-Xin, *et al.*, 2018, Nature (London) **562**, 91.
Yin, Jia-Xin, *et al.*, 2019, Nat. Phys. **15**, 443.
Yin, Jia-Xin, *et al.*, 2020a, Nat. Commun. **11**, 4003.
Yin, Jia-Xin, *et al.*, 2020b, Nature (London) **583**, 533.
Yin, Jia-Xin, *et al.*, 2022, Phys. Rev. Lett. **129**, 166401.
Yin, Lichang, *et al.*, 2021, Phys. Rev. B **104**, 174507.
Yin, Qiangwei, Zhijun Tu, Chunsheng Gong, Shangjie Tian, and Hechang Lei, 2021, Chin. Phys. Lett. **38**, 127401.
Yin, Z. P., K. Haule, and G. Kotliar, 2011, Nat. Mater. **10**, 932.
Yoon, Jiho, Edouard Lesne, Kornelia Sklarek, John Sheckelton, Chris Pasco, Stuart S. P. Parkin, Tyrel M. McQueen, and Mazhar N. Ali, 2020, J. Phys. Condens. Matter **32**, 304004.
You, Jing-Yang, Chih-En Hsu, Mauro Del Ben, and Zhenglu Li, 2025, Phys. Rev. Lett. **134**, 106401.
Yu, F. H., D. H. Ma, W. Z. Zhuo, S. Q. Liu, X. K. Wen, B. Lei, J. J. Ying, and X. H. Chen, 2021, Nat. Commun. **12**, 3645.
Yu, F. H., T. Wu, Z. Y. Wang, B. Lei, W. Z. Zhuo, J. J. Ying, and X. H. Chen, 2021, Phys. Rev. B **104**, L041103.
Yu, Jiawei, *et al.*, 2022, Nano Lett. **22**, 918.
Yu, Tianye, Junwen Lai, Xiangyang Liu, Peitao Liu, Xing-Qiu Chen, and Yan Sun, 2024, Phys. Rev. B **109**, 195145.
Yun, Jo Hyun, *et al.*, 2025, Adv. Mater. **37**, 2415045.
Zeng, Keyu, Zhan Wang, Kun Jiang, and Ziqiang Wang, 2025, Phys. Rev. B **111**, 235114.
Zeng, Keyu, and Ziqiang Wang, 2024, npj Quantum Mater. **9**, 74.
Zhang, Binhua, Junyi Ji, Changsong Xu, and Hongjun Xiang, 2023, arXiv:2307.10565.
Zhang, Dongyao, Zhipeng Hou, and Wenbo Mi, 2022, Appl. Phys. Lett. **120**, 232401.
Zhang, Hongrun, *et al.*, 2023, Adv. Mater. **35**, 2301790.
Zhang, Huai, Can Liu, Yajiu Zhang, Zhipeng Hou, Xuewen Fu, Xiaoming Zhang, Xingsen Gao, and Junming Liu, 2022, Appl. Phys. Lett. **121**, 202401.
Zhang, Huimin, Basu Dev Oli, Qiang Zou, Xu Guo, Zhengfei Wang, and Lian Li, 2023, Nat. Commun. **14**, 6167.
Zhang, Jian-Feng, Kai Liu, and Zhong-Yi Lu, 2021, Phys. Rev. B **104**, 195130.
Zhang, Jie, *et al.*, 2021, arXiv:2105.08888.
Zhang, Lifa, and Qian Niu, 2015, Phys. Rev. Lett. **115**, 115502.
Zhang, Lifa, Jie Ren, Jian-Sheng Wang, and Baowen Li, 2010, Phys. Rev. Lett. **105**, 225901.

Zhang, Qiang, Satoshi Okamoto, German D. Samolyuk, Matthew B. Stone, Alexander I. Kolesnikov, Rui Xue, Jiaqiang Yan, Michael A. McGuire, David Mandrus, and D. Alan Tennant, 2021, Phys. Rev. Lett. **127**, 117201.
Zhang, Quanzhen, *et al.*, 2024, Nano Lett. **24**, 6560.
Zhang, Tiantian, T. Yilmaz, Elio Vescovo, H. X. Li, Rob G. Moore, Ho Nyung Lee, Hu Miao, Shuichi Murakami, and Michael A. McGuire, 2022, npj Comput. Mater. **8**, 155.
Zhang, Wei, *et al.*, 2023, Nano Lett. **23**, 872.
Zhang, Xiaoxiao, *et al.*, 2022, Phys. Rev. Mater. **6**, 105001.
Zhang, Xinyang, Mark P. Zic, Dong Chen, Chandra Shekhar, Claudia Felser, Ian R. Fisher, and Aharon Kapitulnik, 2024, Phys. Rev. B **109**, 144507.
Zhang, Yi, Yuhao Gu, Hongming Weng, Kun Jiang, and Jiangping Hu, 2023, Phys. Rev. B **107**, 035126.
Zhang, Yi-Fan, Xiao-Sheng Ni, Trinanjan Datta, Meng Wang, Dao-Xin Yao, and Kun Cao, 2022, Phys. Rev. B **106**, 184422.
Zhao, He, Hong Li, Brenden R. Ortiz, Samuel M. L. Teicher, Takamori Park, Mengxing Ye, Ziqiang Wang, Leon Balents, Stephen D. Wilson, and Ilija Zeljkovic, 2021, Nature (London) **599**, 216.
Zhao, Jianzhou, Weikang Wu, Yilin Wang, and Shengyuan A. Yang, 2021, Phys. Rev. B **103**, L241117.
Zhao, Zhisheng, *et al.*, 2025, Sci. China Phys. Mech. Astron. **68**, 267012.
Zheng, Guolin, *et al.*, 2023, Nat. Commun. **14**, 678.
Zheng, Guoxin, *et al.*, 2024, J. Phys. Condens. Matter **36**, 215501.
Zhong, Yigui, Jia-Xin Yin, and Kosuke Nakayama, 2024, J. Phys. Soc. Jpn. **93**, 111001.
Zhong, Yigui, *et al.*, 2023a, Nat. Commun. **14**, 1945.
Zhong, Yigui, *et al.*, 2023b, Nature (London) **617**, 488.
Zhong, Yigui, *et al.*, 2024, Phys. Rev. Res. **6**, 043328.
Zhou, Sen, and Ziqiang Wang, 2022, Nat. Commun. **13**, 7288.
Zhou, Xiaoxiang, Yongkai Li, Xinwei Fan, Jiahao Hao, Ying Xiang, Zhe Liu, Yaomin Dai, Zhiwei Wang, Yugui Yao, and Hai-Hu Wen, 2023, Phys. Rev. B **107**, 165123.
Zhou, Xuebo, Hongxiong Liu, Wei Wu, Kun Jiang, Youguo Shi, Zheng Li, Yu Sui, Jiangping Hu, and Jianlin Luo, 2022, Phys. Rev. B **105**, 205104.
Zhou, Yishui, *et al.*, 2024, Phys. Rev. Res. **6**, 043291.
Zhu, Hanyu, Jun Yi, Ming-Yang Li, Jun Xiao, Lifa Zhang, Chih-Wen Yang, Robert A. Kaindl, Lain-Jong Li, Yuan Wang, and Xiang Zhang, 2018, Science **359**, 579.
Zhu, Hongen, *et al.*, 2023, Chin. Phys. Lett. **40**, 047301.
Zhu, Manli, *et al.*, 2024, Nano Lett. **24**, 7483.